2008

Kinetic study of copper chemistry in chemical mechanical polishing (CMP) by an in-situ real time measurement technique

Changhoon Choi
Iowa State University

Kinetic study of copper chemistry in chemical mechanical polishing (CMP) by an in-situ real time measurement technique

by

Changhoon Choi

A dissertation submitted to the graduate faculty

in partial fulfillment of the requirements for the degree of

DOCTOR OF PHILOSOPHY

Major: Chemical Engineering

Program of Study Committee:
Andrew C. Hillier, Major Professor
Kurt R. Hebert
Brent H. Shanks
Steve W. Martin
Pranav Shrotriya

Iowa State University

Ames, Iowa

2008

UMI Number: 3296792

ProQuest Information and Learning Company
300 North Zeeb Road
P.O. Box 1346
Ann Arbor, MI 48106-1346

Dedicated to my parents, Gun-ee Choi and Jin-ja Chun, and my brother, Chang-won Choi

Table of Contents

List of Figures

List of Tables

Abstract

This work describes a systematic approach to study chemical reactions of copper in contact with various chemical agents and to construct a coherent etching rate model based on the fundamental chemistry. Reactions of copper with chemical agents were investigated by in-situ real time technique, quartz crystal microgravimetry (QCM). Kinetic processes were followed by QCM measurement and analyzed. A coherent etching rate formula was built based on the kinetic analysis of fundamental reactions. The requirement of repeated experiments for studying copper chemistry motivated us to develop a high throughput measurement system. We utilized surface plasmon resonance (SPR) imaging combined with multi flow channel or multi electrode for high throughput design. Fundamental physics of SPR technique and instrumental design will be provided in detail. We expect this study has an impact on relatively advanced area that utilizes copper, such as chemical mechanical polishing (CMP) in semiconductor process.

Chapter 1. Introduction

1.1 General introduction

Copper is one of the most important metals in industry and the third most used following iron and aluminum. In 2005, the annual worldwide consumption of copper was 16.6 million tons with an economic value of 60 billion dollars[1]. Copper has a variety of applications including plumbing, automotive, and electrical wire. Because of the environmental importance and impact on industry, phenomena surrounding copper have been intensively studied and corrosion is one of the most studied topics.

Corrosion is an oxidation process of a metal to form by-products or to dissolve by interacting with its environment. Fundamental aspects of copper corrosion have been studied and reviewed[2-5], including thermodynamic aspects[6, 7], kinetics[8], corrosion mechanisms[9, 10], and surface structure[11]. Environmental concerns and protection of copper products has led investigation of effects of various chemical agents, such as pH[12], cations (e.g., Ca^{2+}, Mg^{2+}, and Na^{+})[13], anions (chloride[14-18], carbonate[19, 20], phosphate[21], monochloramine[22]), and inhibitors (benzotriazole[23-27] and thiols[28-37]). One of the most important applications of copper is the usage as electronic wires and the evolution of technology is opening a new era for copper application. In the early 1990s, IBM developed a method to replace aluminum with copper as the interconnect material in integrated circuit (IC) chip structure[38, 39]. Compared with aluminum, copper has advantages of lower resistivity and higher electromigration resistance[40, 41]. Therefore, replacing aluminum with copper makes it possible to manufacture smaller, faster, and more reliable electronic devices.

Copper interconnect lines are formed by Damascene process, in which copper is electrodeposited to form nano scale interconnect wires, followed by chemical mechanical polishing (CMP) [38, 39]. Damascene process consists of a series of steps to make

interconnects (Figure 1.1). Initially, dielectric materials are deposited on a silicon substrate (A). Pattern is created by photolithography and etching process (B). A conformal seed layer of barrier material such as tantalum or tantalum nitride is deposited on the pattern (C). Copper deposition on the barrier layer is achieved by a conformal seed layer deposition through physical vapor deposition (PVD) followed by electrochemical over-deposition (ECD) to fill up the openings (D). Finally, CMP removes the copper overburden and planarizes the surface for subsequent process (E). In the CMP process, the removal rate is different between copper and barrier or dielectric layer and necessary over-polish leads unwanted side effects such as copper dishing or oxide erosion (F). Multiple step processing is often involved to enhance the performance and reduce the side effects, where each step is adjusted for either material removal rate or planarization.

Figure 1.2 shows a schematic of the CMP process. A wafer carrier forces a wafer, on which an IC chip structure is formed, against a polishing pad that is attached to a platen or a polishing table. The carrier and the platen rotate in the same direction to carry out CMP while slurry is supplied to provide chemical and mechanical components. The mechanism of metal CMP is generally accepted as an alternating process of mechanical abrasion and chemical corrosion – the Kaufman model[42]. In the Kaufman model, a metal oxide film is formed on the surface and mechanical abrasion removes the oxide film exposing a bare metal surface to the polishing slurry. Chemicals in the slurry then attack the bare metal to form a new oxide layer (Figure 1.3). Chemical reactions to oxidize metal in CMP are essentially identical to corrosion in addition to which a variety of chemical ingredients are incorporated to control the process and achieve maximum performance. Preparation of slurry that contains chemical components still depends on trial and error rather than on scientific understanding of fundamental chemistry. This motivating example, CMP and slurry solution has a fast growing market. In 2002, total CMP market size was 1.8 billion dollars and it is expected to be over 5 billion dollars in 2008. The market size for CMP slurry was 408 million dollars in 2002 and

is expected to be over 1 billion dollars in 2008[43]. As a result, this will have a great impact on the industry as well as on research to understand fundamental chemistry and to find out the strategy to systematically control etching rate of copper in CMP.

1.2 Objectives

The main objective of this research is to study copper films in contact with various chemical agents and to propose a coherent kinetic model based on fundamental reaction mechanisms. Chemical reactions will be monitored by an in-situ real time detection technique, quartz crystal microgravimetry (QCM). Experimental results will be analyzed considering fundamental chemical reactions and their kinetics.

The investigation of chemical reactions on copper surfaces with various solutions required a number of measurements in a similar fashion, only changing solution compositions. The requirement of a systematic approach and a number of similar measurements to investigate various chemical reactions at solid-liquid interfaces motivated us to develop a method that rapidly screens interfacial reactions. The development of a high throughput measurement technique would decrease the time required for the experiments. We utilized surface plasmon resonance (SPR) imaging as a surface sensitive measurement system in combination with a complementary setup for high throughput measurement.

1.3 Thesis organization

This dissertation consists of 6 chapters. Chapter 2 provides general background of chemical reactions in copper CMP and CMP rate models. Physical principles of the in-situ QCM technique are also provided in this chapter. In chapter 3, copper corrosion in pH controlled aqueous solutions is observed. Fundamental chemical reactions between copper and hydrogen peroxide, glycine, and benzotriazole are investigated at pH 2 where metallic copper is the major surface. An additive etching rate model is constructed based on the fundamental kinetic mechanisms and updated to account for interactions among the chemical

agents. In chapter 4, the solution pH is changed to 10 where the copper surface is passivated and etching rate model is built on the same principle. In chapter 5, a high throughput detection technique is developed to study benzotriazole film formation using SPR imaging system. Another SPR imaging system is also constructed by slight modification. Experimental design of the system is described and exemplary data is provided. Chapter 6 discusses conclusions and future directions of the research project.

1.4 References

1. Jolly, J.L., *The U.S. Copper-base Scrap Industry and Its By-products*. 2006, Copper Development Association Inc.: New York.
2. Merkel, T.H. and S.O. Pehkonen, *General corrosion of copper in domestic drinking water installations: Scientific background and mechanistic understanding.* Corrosion Engineering Science and Technology, 2006. **41**(1): p. 21-37.
3. Jones, D.A., *Principles and Prevention of Corrosion.* 2 ed. 1996, Upper Saddle River: Prentice-Hall.
4. Kear, G., B.D. Barker, and F.C. Walsh, *Electrochemical corrosion of unalloyed copper in chloride media--a critical review.* Corrosion Science, 2004. **46**(1): p. 109-135.
5. Sequeira, C.A.C., *Inorganic, physicochemical, and microbial aspects of copper corrosion: literature survey.* British Corrosion Journal, 1995. **30**(2): p. 137-153.
6. Ives, D.J.G. and A.E. Rawson, *Copper Corrosion .1. Thermodynamic Aspects.* Journal of the Electrochemical Society, 1962. **109**(6): p. 447-451.
7. Pourbaix, M., *Atlas of Electrochemical Equilibria in Aqueous Solutions*. 1974.
8. Ives, D.J.G. and A.E. Rawson, *Copper Corrosion .2. Kinetic Studies.* Journal of the Electrochemical Society, 1962. **109**(6): p. 452-457.
9. Ives, D.J.G. and A.E. Rawson, *Copper Corrosion .3. Electrochemical Theory of General Corrosion.* Journal of the Electrochemical Society, 1962. **109**(6): p. 458-462.
10. Feng, Y., W.-K. Teo, K.-S. Siow, K.-L. Tan, and A.-K. Hsieh, *Corrosion behaviour of copper in neutral tap water. Part I: Corrosion mechanisms.* Corrosion Science, 1996. **38**(3): p. 369-385.
11. Speckmann, H.-D., M.M. Lohrengel, J.W. Schultze, and H.-H. Strehblow, *Growth and reduction of duplex oxide films on copper.* Berichte der Bunsengesellschaft fuer Physikalische Chemie, 1985. **89**(4): p. 392-402.

12. Metikos-Hukovic, M., R. Babic, and I. Paic, *Copper corrosion at various pH values with and without the inhibitor.* Journal of Applied Electrochemistry, 2000. **30**(5): p. 617-624.
13. Notoya, T., V. Otieno-Alego, and D.P. Schweinsberg, *Corrosion and polarization behaviour of copper in domestic water in the presence of Ca, Mg and Na-salts of phytic acid.* Corrosion Science, 1995. **37**(1): p. 55-65.
14. Broo, A.E., B. Berghult, and T. Hedberg, *Copper corrosion in drinking water distribution systems - the influence of water quality.* Corrosion Science, 1997. **39**(6): p. 1119-1132.
15. Milosev, I. and M. Metikos-Hukovic, *Passive films on 90Cu-10Ni alloy. The mechanism of breakdown in chloride containing solutions.* Journal of the Electrochemical Society, 1991. **138**(1): p. 61-67.
16. Bianchi, G., G. Fiori, P. Longhi, and F. Mazza, *Horse shoe corrosion of copper alloys in flowing sea water: mechanism and possibility of cathodic protection of condenser tubes in power stations.* Corrosion (Houston), 1978. **34**(11): p. 396-406.
17. Faita, G., G. Fiori, and D. Salvadore, *Copper behaviour in acid and alkaline brines - 1. Kinetics of anodic dissolution in 0.5 M NaCl and free-corrosion rates in the presence of oxygen.* Corrosion Science, 1975. **15**(6-7): p. 383-392.
18. Braun, M. and K. Nobe, *Electrodissolution kinetics of copper in acidic chloride solutions.* Journal of the Electrochemical Society, 1979. **126**(10): p. 1666-1671.
19. Zhou, A., D. He, N. Xie, Q. Xie, L. Nie, and S. Yao, *Electrochemical quartz crystal microbalance probing the electro-formed and electro-reduced products on a copper electrode in aqueous solutions containing $NaHCO_3$ and Na_2CO_3.* Electrochimica Acta, 2000. **45**(24): p. 3943-3950.
20. Gonzalez, S., M. Perez, M. Barrera, A.R. Gonzalez Elipe, and R.M. Souto, *Mechanism of copper passivation in aqueous sodium carbonate-bicarbonate solution derived from combined X-ray photoelectron spectroscopic and electrochemical data.* Journal of Physical Chemistry B, 1998. **102**(28): p. 5483-5489.
21. Kilincceker, G., B. Yazici., A.B. Yilmaz., and M. Erbil., *Effect of phosphate ions on electrochemical behaviour of copper in sulphate solutions.* British Corrosion Journal, 2002. **37**(1): p. 23-30.
22. Zhang, X., S.O. Pehkonen, N. Kocherginsky, and G.A. Ellis, *Copper corrosion in mildly alkaline water with the disinfectant monochloramine.* Corrosion Science, 2002. **44**(11): p. 2507-2528.
23. Cano, E., J.L. Polo, A. La Iglesia, and J.M. Bastidas, *A study on the adsorption of*

benzotriazole on copper in hydrochloric acid using the inflection point of the isotherm. Adsorption-Journal of the International Adsorption Society, 2004. **10**(3): p. 219-225.

24. Youda, R., H. Nishihara, and K. Aramaki, *Sers and Impedance Study of the Equilibrium between Complex-Formation and Adsorption of Benzotriazole and 4-Hydroxybenzotriazole on a Copper Electrode in Sulfate-Solutions.* Electrochimica Acta, 1990. **35**(6): p. 1011-1017.
25. Youda, R., H. Nishihara, and K. Aramaki, *A Sers Study on Inhibition Mechanisms of Benzotriazole and Its Derivatives for Copper Corrosion in Sulfate-Solutions.* Corrosion Science, 1988. **28**(1): p. 87-96.
26. Dugdale, I. and J.B. Cotton, *Electrochemical investigation on prevention of staining of copper by benzotriazole.* Corrosion Science, 1963. **3**(2): p. 69-74.
27. Brusic, V., M.A. Frisch, B.N. Eldridge, F.P. Novak, F.B. Kaufman, B.M. Rush, and G.S. Frankel, *Copper Corrosion with and without Inhibitors.* Journal of the Electrochemical Society, 1991. **138**(8): p. 2253-2259.
28. Beccaria, A.M. and C. Bertolotto, *Inhibitory action of 3-trimethoxysilylpropanethiol-1 on copper corrosion in NaCl solutions.* Electrochimica Acta, 1997. **42**(9): p. 1361-1371.
29. Feng, Y.Q., W.K. Teo, K.S. Siow, Z.Q. Gao, K.L. Tan, and A.K. Hsieh, *Corrosion protection of copper by a self-assembled monolayer of alkanethiol.* Journal of the Electrochemical Society, 1997. **144**(1): p. 55-64.
30. Haneda, R., H. Nishihara, and K. Aramaki, *Chemical modification of an alkanethiol self-assembled layer to prevent corrosion of copper.* Journal of the Electrochemical Society, 1997. **144**(4): p. 1215-1221.
31. Jennings, G.K., J.C. Munro, T.H. Yong, and P.E. Laibinis, *Effect of chain length on the protection of copper by n-alkanethiols.* Langmuir, 1998. **14**(21): p. 6130-6139.
32. Jennings, G.K. and P.E. Laibinis, *Self-assembled monolayers of alkanethiols on copper provide corrosion resistance in aqueous environments.* Colloids and Surfaces a-Physicochemical and Engineering Aspects, 1996. **116**(1-2): p. 105-114.
33. Baba, H. and T. Kodama, *Corrosion inhibition and characteristics of the triazinedithiol surface film on copper under potentiostatic anodization.* Corrosion Science, 1999. **41**(10): p. 1987-2000.
34. Laibinis, P.E. and G.M. Whitesides, *Self-Assembled Monolayers of N-Alkanethiolates on Copper Are Barrier Films That Protect the Metal against Oxidation by Air.* Journal of the American Chemical Society, 1992. **114**(23): p. 9022-9028.
35. Marconato, J.C., L.O. Bulhoes, and M.L. Temperini, *A spectrocelectrochemical study*

of the inhibition of the electrode process on copper by 2-mercaptobenzothiazole in ethanolic solutions. Electrochimica Acta, 1998. **43**(7): p. 771-780.

36. Whelan, C.M., M. Kinsella, H.M. Ho, and K. Maex, *Corrosion inhibition by thiol-derived SAMs for enhanced wire bonding on Cu surfaces.* Journal of the Electrochemical Society, 2004. **151**(2): p. B33-B38.
37. Tremont, R. and C.R. Cabrera, *Electrochemical and surface analysis study of copper corrosion protection by 1-propanethiol and propyltrimethoxysilane: A comparison with 3-mercaptopropyltrimethoxysilane.* Journal of Applied Electrochemistry, 2002. **32**(7): p. 783-793.
38. Beyer, K.D., W.L. Guthrie, S.R. Makarewicz, E. Mendel, W.J. Patrick, K.A. Perry, W.A. Pliskin, J. Riseman, P.M. Schaible, and C.L. STandley, *Chem-mech Polishing Method for Producing Coplanar Metal/insulator Films on a Substrate.* U.S. Patent 4,944,836, 1990.
39. Kaanta, C.W., S.G. Bombardier, W.J. Cote, W.R. Hill, G. Kerszykowski, H.S. Landis, D.J. Poindexter, C.W. Pollard, G.H. Ross, J.G. Ryan, S. Wolff, and J.E. Cronin, *Dual Damascene: A ULSI Wiring Technology.* VMIC Conference, 1991: p. 144.
40. Oliver, M.R., *Chemical-Mechanical Planarization of Semiconductor Materials*. 2004.
41. Steigerwald, J.M., S.P. Murarka, and R.J. Gutman, *Chemical Mechanical Planarization of Microelectronic Materials*. 1997.
42. Kaufman, F.B., D.B. Thompson, R.E. Broadie, M.A. Jaso, W.L. Guthrie, D.J. Pearson, and M.B. Small, *Chemical-Mechanical Polishing for Fabricating Patterned W Metal Features as Chip Interconnects.* Journal of the Electrochemical Society, 1991. **138**(11): p. 3460-3465.
43. Tucker, T., *CMP Market and Technology Status - 2002.* Northern California Chapter of the American Vacuum Society (NCCAVS) CMPUG Proceedings, 2002.
44. Andricacos, P.C., C. Uzoh, J.O. Dukovic, J. Horkans, and H. Deligianni, *Damascene copper electroplating for chip interconnections.* Ibm Journal of Research and Development, 1998. **42**(5): p. 567-574.

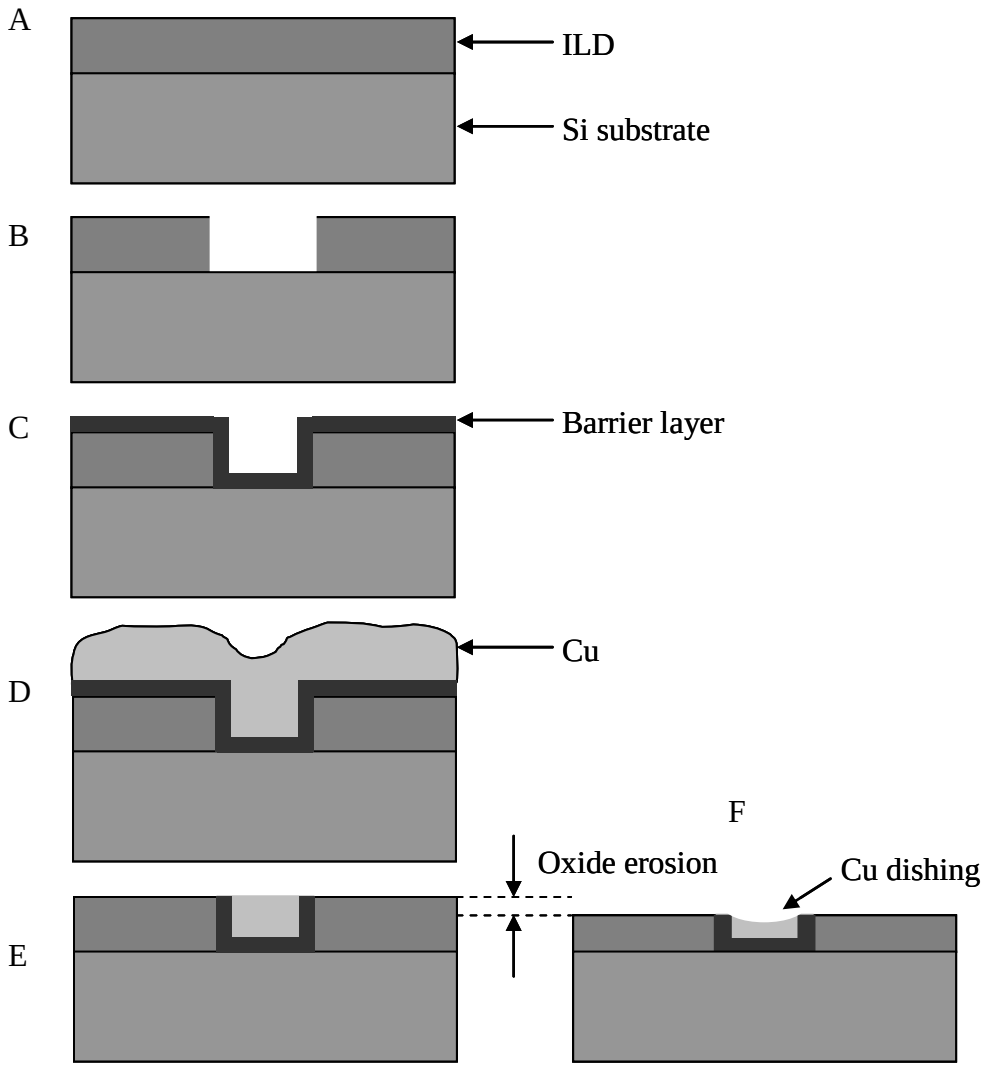

Figure 1.1 Damascene process: (A) inter layer dielectric (ILD) material deposition (B) ILD etching (C) deposition of barrier layer (D) Cu deposition (E) Desired surface by CMP (F) Over-polished surface with surface defects of oxide erosion and Cu dishing (adapted from [44]).

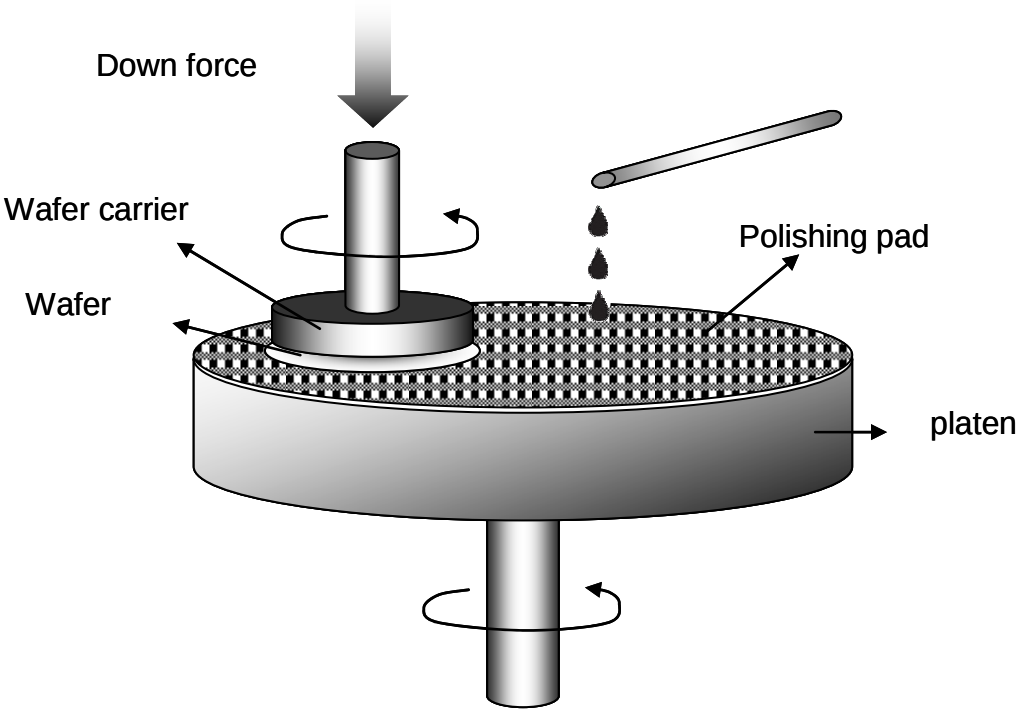

Figure 1.2 A schematic of CMP process. Slurry is supplied to provide chemical and mechanical components while polishing process (adapted from [42]).

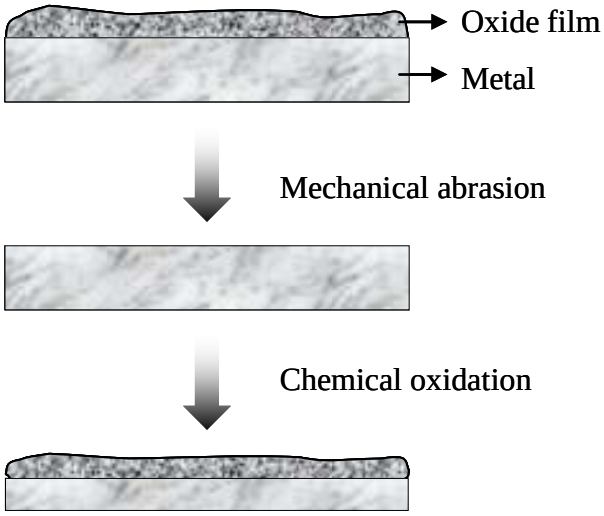

Figure 1.3 Kaufman model [42]for metal CMP process. Metal oxide film is formed on the surface and mechanical abrasion removes the oxide film exposing bare metal surface to polishing slurry. Chemicals in the slurry then attack the bare metal to form a new oxide layer (adapted from [42]).

Chapter 2. Background

This chapter presents a review of copper chemistry in aqueous solutions with various chemical agents and technical principles for quartz crystal microgravimetry (QCM). Chemical reactions of copper in aqueous solutions are essentially corrosion process. In corrosion process, copper is oxidized by dissolved gases and ions to form passivatioin layer of copper oxide or dissolve into solutions. A variety of chemical agents have an effect on the copper corrosion rate and thermodynamic equilibrium. In copper chemical mechanical polishing (Cu-CMP) as a motivating example of this study, it is required to understand the kinetic process of copper corrosion or etching in the presence of various chemical agents in order to prepare more efficient slurry and therefore enhance the performance. Previously, as an effort to understand CMP process without detailed kinetic information about copper corrosion, a few qualitative and quantitative models for CMP performance have been proposed. However, it is still necessary to study more detailed kinetic information of chemical reactions and to propose a quantitatively more precise model. Kinetic study of chemical reactions in solutions requires in-situ real time observation and quartz crystal microgravimetry (QCM) will be utilized as a major tool in this study. QCM is a surface sensitive technique that measures mass change on a metal coated quartz crystal using the principle of piezoelectricity. A resonant frequency that is proportional to the mass change within a limited amount is measured by QCM. The physical principles of QCM and its applications will be presented.

2.1 General copper chemistry in aqueous solutions and copper chemical mechanical polishing (Cu-CMP)

2.1.1 Copper etching with effective chemical agents in aqueous solutions

Chemical reactions of copper in copper chemical mechanical polishing (Cu-CMP) are essentially corrosion process and general information about thermodynamic equilibrium of copper in aqueous solutions and kinetic mechanism of corrosion process is available. Thermodynamic equilibrium state of copper in aqueous solution is explained by Pourbaix diagram (Figure 2.1) [1]. In aqueous solution, copper interacts with the solution to dissolve or to form a passivation layer and in the absence of other chemical effects or electrochemical potentials, solution pH is the primary factor that controls copper corrosion. For example, metallic copper is at equilibrium with cupric ions at low pH and continuous corrosion process occurs. At moderately high pH, the surface is passivated by oxidized copper. Although cuprous oxide and cupric oxide are favorable thermodynamically, cupric hydroxide is also possible. When the solution pH is extremely high (> ~13.5), corrosion occurs again. Kinetic mechanism of copper corrosion in aqueous solution was studied by Ives and Rawson[2, 3]. Ives and Rawson explained copper dissolution mechanism as a series of steps, that is, oxidation by dissolved oxygen in the solution followed by dissolution of the copper oxide by proton and oxygen. They assumed that metallic copper is instantly oxidized on the surface by combining with oxygen to form cuprous oxide.

$$Cu_{(s)} + \frac{1}{2}O_{2(g)} = \frac{1}{2}Cu_2O_{(s)} \tag{2.1}$$

The cuprous oxides interact with more oxygen and protons being removed from the surface.

$$\frac{1}{2}Cu_2O_{(s)} + \frac{1}{4}O_{2(g)} + 2H^{+}_{(aq)} = Cu^{2+}_{(aq)} + H_2O \tag{2.2}$$

In copper chemical mechanical polishing (Cu-CMP), the corrosion process becomes more complicated by the presence of chemical agents. A variety of chemical agents are supplied to provide etching rate control during CMP process. They include, namely, oxidizer, complexing agent, and inhibitor. Each chemical agent has different interaction with copper surface and affect copper etching rate accordingly.

Oxidizing agents or oxidizers are used in metal CMP to mainly control oxidation rate. In Cu-CMP, oxidizers transform the copper surface to a more oxidized state, cuprous oxide and cupric oxide. Copper oxide that formed by an oxidizer may passivate the surface or dissolve into solutions depending on the presence of other ions. For example, the presence of carbonate anions forms a precipitate by combining with copper oxide[4, 5], while copper oxide is dissolved when glycine is present[6, 7]. The fundamental aspect of an oxidizer is simple, but when incorporated with other chemicals, it becomes complicated and requires clarification. The most studied oxidizer is hydrogen peroxide[6-13] and others include iodate ion[14-17], periodic acid, dichromate,[18] ferric nitrate,[15, 19] nitrate ion,[15, 20] manganate, ammonium heptamolybdate,[15] sodium chlorate,[21] and ferrocyanide ion[20].

Complexing agents are used to increase material removal rate in Cu-CMP either by directly etching copper surface or by enhancing solubility of abraded particles. This effect occurs by complexing with partially or fully charged species, therefore having synonyms such as chelating agents or binding agents. The complexation increase copper dissolution rate by preventing reduction of oxidized copper or further oxidation to form stable oxide products[22]. Complexing agent is one of the essential components for Cu-CMP at some conditions but the fundamental aspects of complexation reaction are still unclear. Ammonia[20, 21, 23] or amino acids such as glycine,[7-9, 24-27] cysteine,[9, 27] ethylenediamine,[28] hydroxylamine,[26] and citric acid[29] are commonly used as complexing agents.

Inhibitors are passivating agents that reduce chemical dissolution. Most inhibitors form passivating layers and physically decrease contacting area for dissolution. The most widely known inhibitor for copper corrosion is benzotriazole (BTA). Since the first report by Cotton and Scholes[30] about the BTA inhibition on copper corrosion, the properties of BTA film including structure,[31-41] film formation mechanism[42-44] and stability[42] were extensively studied. Another class of well known inhibitors are self-assembled monolayers

(SAMs) by thiols such as n-alkanethiol[45-57], alkyl-thiosulfate[58], triazinedithiol[59], 3-methoxysilylpropanethiol-1[60], 2-mercaptobenzothiazole[61], propyltrimethoxysilane, and 3-mercaptopropyltrimethoxysilane[62]. The compact structure of SAM layer prohibits copper corrosion. For n-alkanethiols, it is known that longer alkane chain length provides better inhibition effect[53, 54].

Although various chemicals have strong effects on the copper etching rate as stated above, detailed descriptions of the fundamental chemical reactions are not fully developed yet. Cu-CMP as a motivation of this study requires understanding about the chemical reactions at a molecular level in order to prepare successful slurry and hence to achieve maximum performance out of CMP process to meet industrial need. Several CMP models have been proposed as an effort to accomplish this objective.

2.1.2 Copper corrosion rate model

2.1.2.1 Preston model

At the early stage of CMP application in industry, CMP rate models have developed in the absence of kinetic understanding about chemical reactions. Therefore, early CMP models only account for mechanical function as independent variables to explain CMP rate. The Preston model is generally accepted as the first CMP model[63]. In the Preston model, the material removal rate is given by considering only mechanical terms, applied pressure and the relative speed of the surface vs. pad.

$$R_P = K_P \times P \times V \tag{2.3}$$

R_P is the material removal rate, K_P is Preston's coefficient, P is the local pressure on the surface, and V is the relative velocity of the surface against the pad. The Preston model was the first CMP model that predicted material removal rate and since then several attempts have been made to improve the rate prediction[64-69]. However, the Preston model does not

consider chemical effects and hence has its own limitations to apply in Cu-CMP that requires molecular level for complete control and understanding.

2.1.2.2 Kaufman model

A more recent model that considers chemical effects has been developed by Kaufman who described metal CMP as an alternating process of chemical corrosion and mechanical abrasion[70], Figure 1.2. The Kaufman model is accepted as a general qualitative model that describes the metal CMP process. Kaufman speculates that the chemical corrosion is a process to form a soft passivation layer that is removed by mechanical actions. This is because the Kaufman model is based on tungsten CMP where the oxide layer completely passivates the tungsten surface. However, in Cu-CMP, copper corrosion is not simply passivation but it can also cause dissolution, which makes it more complicated than tungsten CMP. Furthermore, the Kaufman model is only a qualitative description, oversimplifying the process and hence suffers some serious limitations[15, 71].

2.1.2.3 Paul model

It was Paul who considered the complex CMP process in more detail with quantitative description of chemical reactions [72]. Paul adopted simple kinetic expressions for chemical reactions and mechanical abrasion processes and then combined them to obtain an overall CMP rate expression. Chemical dissolution was given by the simplest kinetic expression

$$r_D = k_D N_{MC^*} \tag{2.4}$$

where r_D is the dissolution reaction rate, k_D is the rate constant of dissolution reaction, and N_{MC^*} is the number of surface sites that are available for dissolution or mechanical abrasion. Mechanical abrasion was also given by the simple kinetic expression

$$r_M = k_M \left(N_p / A\right) N_{MC^*} \tag{2.5}$$

where r_M is the rate of mechanical abrasion, k_M is the rate constant of mechanical abrasion, N_p is the number of effective abrasive particles, and A is the workpiece area. The overall CMP rate was simply given by the addition of chemical dissolution rate and mechanical abrasion rate.

$$R_{Paul} = \left(r_D + r_M\right)/A \tag{2.6}$$

R_{Paul} is the sum of dissolution and mechanical abrasion processes.

The main idea of the Paul model is that the complicated chemical reactions and mechanical abrasion processes are separable and their kinetic expressions can be combined to yield an expression for overall CMP rate. Paul demonstrates that this idea is valid by applying his model to tungsten CMP as a function of oxidizer concentration[73], polishing pressure and speed[74], and inhibitors[75]. Furthermore, Paul extended this idea to Cu-CMP to explain polish rate as a function of oxidizers by considering each chemical reaction in more detail [76].

In the Paul model for Cu-CMP, the oxidation, etching, and mechanical abrasion are expressed in simple kinetic expressions and combined to obtain an overall polishing rate. They consider three different sites of copper surface, namely, Cu, Cu(I), and Cu(II). Cu and Cu(I) are considered oxidized by an oxidizer such as H_2O_2

$$Cu + H_2O_2 \rightarrow Cu(I) \qquad r_{O1} = k_{C01}[H_2O_2]n_0 \tag{2.7}$$

$$Cu(I) + H_2O_2 \rightarrow Cu(II) \qquad r_{O2} = k_{C12}[H_2O_2]n_1 \tag{2.8}$$

where, k_{C01} and k_{C12} are the rate constants for oxidation of Cu to Cu(I) and Cu(I) to Cu(II), respectively. n_0, n_1, and n_2 represent the number of Cu, Cu(I), and Cu(II) on the surface, respectively. The equations for etching of Cu(I) and Cu(II) are given by

$$Cu(I) \rightarrow Cu + Cu^{+}(aq) \qquad r_{W1} = k_{W1}n_1 \tag{2.9}$$

$$Cu(I) + L \rightarrow Cu + Cu^{+}L(aq) \qquad r_{L1} = k_{L1}[L]n_1 \tag{2.10}$$

$$Cu(II) \rightarrow Cu(I) + Cu^{2+}(aq) \qquad r_{W2} = k_{W2}n_2 \tag{2.11}$$

$$Cu(II) + L \rightarrow Cu(I) + Cu^{2+}L(aq) \qquad r_{L2} = k_{L2}[L]n_2 \tag{2.12}$$

where, L represents a ligand that can be used as an etchant and $[L]$ is its concentration, k_{W1}, k_{W2}, k_{L1}, and k_{L2} are rate constants for etching of Cu(I) and Cu(II) by water ($_W$) and ligand ($_L$). The equations for mechanical abrasion to remove debris Y from the surface into the slurry and to reveal the underlying Cu or Cu(I) layers are given by

$$Cu \rightarrow Cu + Y \qquad r_{M0} = \kappa_{M0} n_0 \tag{2.13}$$

$$Cu(I) \rightarrow Cu + Y \qquad r_{M1} = \kappa_{M1} n_1 \tag{2.14}$$

$$Cu(II) \rightarrow Cu(I) + Y \qquad r_{M2} = \kappa_{M2} n_2 \tag{2.15}$$

where, κ_{M0}, κ_{M1}, and κ_{M2} are mechanical abrasion rate constants that include the effects of pressure and speed by $\kappa_{Mi} = k_{Mi} Pv$. The schematic diagram of these chemical reactions that occur during Cu-CMP is shown in Figure 2.2. The material removal rate per surface area is the sum of each term for the removal processes

$$R = \frac{\tau_0' \kappa_{M0} n_0 + \tau_1' \kappa_{M1} n_1 + \tau_2' \kappa_{M2} n_2 + \tau' (\kappa_{W1} + \kappa_{L1}[L]) n_1 + \tau' (\kappa_{W2} + \kappa_{L2}[L]) n_2}{A_W} \tag{2.16}$$

where, τ' represents the monolayer removal volume, and τ_0', τ_1', and τ_2' are mechanical removal volumes for Cu metal, Cu(I), and Cu(II), respectively. Under the steady state conditions, dn_i/dt, expressed in terms of kinetic rate expressions for oxidation, etching, and mechanical abrasion, become zero.

$$\frac{dn_0}{dt} = -r_{O1} + r_{W1} + r_{L1} + r_{M1} = 0 \tag{2.17}$$

$$\frac{dn_1}{dt} = r_{O1} - r_{O2} - r_{W1} - r_{L1} + r_{W2} + r_{L2} - r_{M1} + r_{M2} = 0 \tag{2.18}$$

$$\frac{dn_2}{dt} = r_{O2} - r_{W2} - r_{L2} - r_{M2} = 0 \tag{2.19}$$

Using the equations (2.16) along with (2.17), (2.18), and (2.19), they obtained a quantitative expression for overall material removal rate. Assuming mechanical variables and complexing agent concentrations to be held constant, the overall material removal rate is given by

$$R = \frac{a_0 + a_1 [H_2O_2] + a_2 [H_2O_2]^2}{a_3 + a_4 [H_2O_2] + [H_2O_2]^2} \tag{2.20}$$

for peroxide oxidizers, where a_i depends on the mechanical rates, chemical rates, and the removal depths (detailed expressions of a_i are given in reference [76]), τ_i, which is given by $\tau_i = \tau_i' / d_{Cu}^2$. They also find the removal rate expressioin for non-peroxide oxidizers

$$R = \frac{\tau_0 k_{M0} k_{M2} Pv + \tau_2 k_{M2} k_{C01}[C]}{k_{M2} Pv + k_{C01}[C]} Pv = \frac{b_1 Pv + b_2[C]}{b_3 Pv + [C]} Pv \qquad (2.21)$$

where $[C]$ is oxidizer concentration replacing $[H_2O_2]$, P is pressure, and v is relative velocity of the wafer against the pad and b_i is given by $b_1 = \tau_0 k_{M0} k_{M2} / k_{C01}$, $b_2 = \tau_2 k_{M2}$, and $b_3 = k_{M2} / k_{C01}$. The simulated results shows good agreement with experimental measurement as a function of various oxidizers, including hydrogen peroxide, $K_3Fe(CN)_6$, KIO_3, and $K_2Cr_2O_7$. By this successful simulation, they demonstrate that their assumptions are also valid for Cu-CMP.

Paul model significantly improves CMP models by incorporating simplified kinetic models and obtaining a quantitative expression for material removal rate. However, Paul model has its own limitations. First, the Paul model fits the material removal rate as a function of oxidizers in the presence of glycine and mechanical abrasion, without knowing the kinetic information about each reaction. Since they don't have fundamental kinetic information, they lump sets of kinetic constants together creating a new set of parameters to fit measured material removal rates. Hence, the Paul model cannot yield kinetic rate constants of the fundamental reaction mechanisms by fitting experimental results. Second, pH, the most important chemical factor in Cu-CMP, is not incorporated as an independent variable for the equation of material removal rate. Third, simplified kinetic mechanisms are used rather than more realistic mechanisms for chemical reactions. As a result, information of fundamental chemical reactions is not obtained by the Paul model. Kinetic study of individual chemical reactions is still needed so that more advanced CMP model can be constructed, which motivated this work.

2.2 Quartz crystal microbalance (QCM)

The quartz crystal microbalance (QCM) is a technique that can detect various events at solid-liquid interfaces. The operating principle of QCM is based on piezoelectricity of quartz crystal discovered by Jacques and Pierre Curie in 1880[77]. A quartz disk is sandwiched between two metal films and the application of alternating potentials to the metal films leads to a shear mode vibration of the quartz crystal, which is sensitive to any changes on the surface. Sauerbrey first revealed that the change of mechanical strain or resonance frequency of quartz crystal has a linear relationship with additional mass on the crystal surface[78]. Although QCM is capable of observing various interface phenomena, i.e. roughness, viscosity, etc., major applications are based on its capability of mass detection with high sensitivity.

2.2.1 Fundamental principles of QCM

2.2.1.1 Piezoelectric effect

The piezoelectric effect was originally discovered by Jacques and Pierre Curie in 1880[77]. Since then, the explanation of piezoelectric effect in molecular level was given by Lord Kelvin in 1946.[79] Figure 2.3A shows a model that represents a unit cell of a quartz crystal that consists of positive and negative ions. Assuming each positive and negative ion has charge of $+q$ and $-q$, respectively, the net charge of the unit cell is zero. In addition, the three pairs of dipoles are balanced making the net dipole moments zero. Let's suppose a mechanical stress is applied to this unit cell causing deformation as shown in Figure 2.3B. The deformation shifts the charge balance to left and right hand side for positive and negative charges, respectively. The ions shift along the corner of circle to maintain the distance of oppositely charged dipoles. The result of this charge balance shift is the generation of non-zero dipole moments in the horizontal direction. When a reverse of this pressure is applied, the shifts of net charge and dipole moments are reversed with the same magnitude. More detailed mathematical description of piezoelectricity can be found in literature.[80] The

converse-piezoelectric effect is achieved by applying electric voltage to the unit cell, producing mechanical strain.

2.2.1.2 Quartz crystal and mass detection by Sauerbrey's relationship

Various crystal and ceramics have piezoelectricity and quartz crystal is mainly used for QCM application. Chemical formula of quartz crystal is silicon dioxide, SiO_2. Quartz crystal has two stable forms depending on temperature and alpha quartz that is stable below 573 °C is of interest as a resonator. Figure 2.4 shows an alpha quartz crystal[81]. Quartz crystal must be cut to have a specific orientation with respect to z-axis in order to be used in a QCM device. Various cuts are available but AT-cut quartz crystal, which has angle of 35 ° 15 ′ relative to z-axis, is mainly used because of its low temperature-coefficient at room temperature[82, 83]. In other words, AT-cut quartz crystal has minimal frequency variation by temperature changes, especially between 0 and 50 °C, which makes temperature-coefficient close to zero.

Quartz crystal is cut to have disk shape and electrodes are vapor-deposited on both sides to apply electric potential (Figure 2.5A). Applying potential to quartz crystal through the metal electrodes produces mechanical strain. The deformation is elastic and parallel to the surface of quartz crystal. Opposite potential creates mechanical strain with opposite direction. Therefore, applying alternate potential causes the quartz crystal to vibrate in thickness shear mode (Figure 2.5B) and creates a transverse acoustic wave (Figure 2.5C). Transverse acoustic wave proceeds across the thickness of quartz crystal ($t_{q,0}$), reflecting back into the crystal at the surfaces. When the wavelength of acoustic wave is equal to 2 t_q, standing wave condition is satisfied and resonant frequency (f_0) is given by

$$\lambda_0 = \frac{v_{tr}}{f_0} = 2t_{q,0} \tag{2.22}$$

where v_{tr} represents transverse velocity of sound in AT-cut quartz [84]. Crystal surfaces act as antinodes of acoustic wave. When the crystal surface is uniformly covered by an additional layer of foreign material, the acoustic wave travels through the additional layer in addition to quartz crystal. This fractional change of thickness results in change of resonant frequency (Δf).

$$\lambda_1 = \frac{v_{tr}}{f_1} = 2t_{q,1} = 2\left(t_{q,0} + \Delta t\right) \tag{2.23}$$

$t_{q,1}$ is combined thickness of quartz crystal and additional layer (Δt) and f_1 is new resonant frequency by additional layer. The difference between the new resonant frequency, f_1, and the original frequency, f_0, is given by

$$\Delta f = f_1 - f_0 = \frac{-v_{tr}\Delta t}{2t_{q,0}\left(t_{q,0} + \Delta t\right)} \tag{2.24}$$

Hence, the ratio of Δf against original frequency, f_0, is

$$\frac{\Delta f}{f_0} = -\frac{2\Delta t \cdot f_1}{v_{tr}} \tag{2.25}$$

On the other hand, the thickness change (Δt) is expressed by mass change (Δm)

$$\Delta t = \frac{\Delta m}{A \cdot \rho_q} \tag{2.26}$$

where A is piezoelectrically active surface area and ρ_q is quartz density (ρ_q = 2.648 g cm^{-3}). The transverse velocity of sound in quartz, v_{tr}, is expressed by

$$v_{tr} = \sqrt{\mu_q / \rho_q} \tag{2.27}$$

where μ_q is shear modulus of quartz (μ_q = 2.947 × 10^{11} g cm^{-1} s^{-2}). Rearrangement of equation (2.25) with (2.26) and (2.27) gives a new expression for Δf.

$$\Delta f\left(1 + \frac{2 \cdot f_0 \cdot \Delta m}{A \cdot \sqrt{\mu_q \cdot \rho_q}}\right) = \frac{-2 \cdot f_0^2 \cdot \Delta m}{A \cdot \sqrt{\mu_q \cdot \rho_q}} \tag{2.28}$$

When the mass of additional layer (Δm) is extremely small, the right term inside parenthesis of equation (2.28) becomes negligible compared to 1 to make

$$\Delta f \approx \frac{-2 \cdot f_0^2 \cdot \Delta m}{A \cdot \sqrt{\mu_q \cdot \rho_q}} \tag{2.29}$$

Equation (2.29) is well known Sauerbrey equation[78]. The right hand side of equation (2.29) is constant except for Δm

$$\Delta f = -C_f \cdot \Delta m \tag{2.30}$$

where C_f is the integral sensitivity constant and corresponds to $2 f_0^2 / \left(A \mu_q^{1/2} \rho_q^{1/2} \right)$. For 10 MHz AT-cut quartz crystal, C_f is equal to 2.26×10^2 Hz cm^2 μg^{-1}. It is considered that QCM measurement is accurate when mass loading is less than 2 % of quartz crystal weight[84].

Sauerbrey's relationship to measure mass loading on quartz crystal requires several assumptions. First assumption is so-called no-slip condition, which states that displacement and shear stress of quartz crystal and additional layer are continuous across the interface. Second assumption is that the density and the transverse acoustic wave velocity in additional layer are alike with those of quartz crystal. In addition, it is required that additional layer is uniformly deposited across the resonator surface. Ideally, frequency change according to mass loading needs to be identical regardless of radial distance from the center of quartz crystal resonator. In other words, local (differential) sensitivity constant ($c_f = df / dm$) is required to be same with integral sensitivity constant, C_f. However, local sensitivity is greater at the radial center of resonator than at the edge[85]. Therefore uniform deposition of additional layer will validate the use of Sauerbrey's equation to measure average thickness.

2.2.2 QCM applications in liquid for kinetic process observation

QCM is one of the most effective tools to investigate kinetic processes in liquid. Early development of QCM is to detect mass change at gas and vacuum environment but it was also required to use in liquid environment[86]. However it was not applicable until

Kanazawa and Gordon revealed that the shift of resonant frequency by liquid loading is discernible from mass change on the resonator surface[87, 88]. Kanazawa and Gordon obtained a quantitative description of velocity distribution in the fluid and presented a simple expression for the frequency shift in contact with a liquid fluid based on a simple shear wave model. The frequency shift depends on fluid viscosity and density according Kanazawa and Gordon equation. However, the sensitivity of quartz resonator on mass loading is unaffected by liquid contact. In addition, the fast response time of quartz resonators allows QCM to monitor many surface reactions real time in liquid solutions although it is slower than in contact with air [89]. Therefore, QCM is an ideal technique to investigate interfacial reactions in liquid for kinetic study.

2.3 References

1. Pourbaix, M., *Atlas of Electrochemical Equilibria in Aqueous Solutions*. 1974.
2. Ives, D.J.G. and A.E. Rawson, *Copper Corrosion .2. Kinetic Studies.* Journal of the Electrochemical Society, 1962. **109**(6): p. 452-457.
3. Ives, D.J.G. and A.E. Rawson, *Copper Corrosion .3. Electrochemical Theory of General Corrosion.* Journal of the Electrochemical Society, 1962. **109**(6): p. 458-462.
4. Zhou, A., D. He, N. Xie, Q. Xie, L. Nie, and S. Yao, *Electrochemical quartz crystal microbalance probing the electro-formed and electro-reduced products on a copper electrode in aqueous solutions containing $NaHCO_3$ and Na_2CO_3.* Electrochimica Acta, 2000. **45**(24): p. 3943-3950.
5. Gonzalez, S., M. Perez, M. Barrera, A.R. Gonzalez Elipe, and R.M. Souto, *Mechanism of copper passivation in aqueous sodium carbonate-bicarbonate solution derived from combined X-ray photoelectron spectroscopic and electrochemical data.* Journal of Physical Chemistry B, 1998. **102**(28): p. 5483-5489.
6. Aksu, S., L. Wang, and F.M. Doyle, *Effect of hydrogen peroxide on oxidation of copper in CMP slurries containing glycine.* Journal of the Electrochemical Society, 2003. **150**(11): p. G718-G723.
7. Lu, J., J.E. Garland, C.M. Pettit, S.V. Babu, and D. Roy, *Relative roles of H2O2 and glycine in CMP of copper studied with impedance spectroscopy.* Journal of the Electrochemical Society, 2004. **151**(10): p. G717-G722.

8. Seal, S., S.C. Kuiry, and B. Heinmen, *Effect of glycine and hydrogen peroxide on chemical-mechanical planarization of copper.* Thin Solid Films, 2003. **423**(2): p. 243-251.
9. Hariharaputhiran, M., J. Zhang, S. Ramarajan, J.J. Keleher, Y.Z. Li, and S.V. Babu, *Hydroxyl radical formation in H2O2-amino acid mixtures and chemical mechanical polishing of copper.* Journal of the Electrochemical Society, 2000. **147**(10): p. 3820-3826.
10. Zeidler, D., Z. Stavreva, M. Plotner, and K. Drescher, *Characterization of Cu chemical mechanical polishing by electrochemical investigations.* Microelectronic Engineering, 1997. **33**(1-4): p. 259-265.
11. Wang, M.T., M.S. Tsai, C. Liu, W.T. Tseng, T.C. Chang, L.J. Chen, and M.C. Cheng, *Effects of corrosion environments on the surface finishing of copper chemical mechanical polishing.* Thin Solid Films, 1997. **308**: p. 518-522.
12. Lu, W.Q., J. Zhang, F. Kaufman, and A.C. Hillier, *A combined triboelectrochemical QCM for studies of the CMP of copper.* Journal of the Electrochemical Society, 2005. **152**(1): p. B17-B22.
13. Ein-Eli, Y., E. Abelev, and D. Starosvetsky, *Electrochemical behavior of copper in conductive peroxide solutions.* Journal of the Electrochemical Society, 2004. **151**(4): p. G236-G240.
14. Hsu, J.-W., S.-Y. Chiu, M.-S. Tsai, B.-T. Dai, M.-S. Feng, and H.-C. Shih, *Electrochemical behavior of copper chemical mechanical polishing in KlO_3 slurry.* Journal of Vacuum Science and Technology B: Microelectronics and Nanometer Structures, 2002. **20**(2): p. 608-612.
15. Kneer, E.A., C. Raghunath, V. Mathew, S. Raghavan, and J.S. Jeon, *Electrochemical measurements during the chemical mechanical polishing of tungsten thin films.* Journal of the Electrochemical Society, 1997. **144**(9): p. 3041-3049.
16. Anik, M., *Reduction characteristics of iodate ion on copper: Application to copper chemical mechanical polishing.* Journal of Applied Electrochemistry, 2004. **34**(9): p. 963-969.
17. Anik, M., *Selection of an oxidant for copper chemical mechanical polishing: Copper-iodate system.* Journal of Applied Electrochemistry, 2005. **35**(1): p. 1-7.
18. Lee, B.-C., D.J. Duquette, and R.J. Gutmann. *Synthesis of model alumina slurries for damascene patterning of copper*. in *Chemical - Mechanical Polishing 2001 - Advances and Future Challenges, Apr 18-20 2001*. 2001. San Francisco, CA: Materials Research Society.

19. Fayolle, M. and F. Romagna, *Copper CMP evaluation: planarization issues.* Microelectronic Engineering, 1997. **37-8**(1-4): p. 135-141.
20. Steigerwald, J.M., S.P. Murarka, R.J. Gutmann, and D.J. Duquette, *Chemical Processes in the Chemical-Mechanical Polishing of Copper.* Materials Chemistry and Physics, 1995. **41**(3): p. 217-228.
21. Luo, Q., R.A. Mackay, and S.V. Babu, *Copper dissolution in aqueous ammonia-containing media during chemical mechanical polishing.* Chemistry of Materials, 1997. **9**(10): p. 2101-2106.
22. Oliver, M.R., *Chemical-Mechanical Planarization of Semiconductor Materials*. 2004.
23. Luo, Q., D.R. Campbell, and S.V. Babu, *Chemical-mechanical polishing of copper in alkaline media.* Thin Solid Films, 1997. **311**(1-2): p. 177-182.
24. Aksu, S. and F.M. Doyle, *The role of glycine in the chemical mechanical planarization of copper.* Journal of the Electrochemical Society, 2002. **149**(6): p. G352-G361.
25. Deshpande, S., S.C. Kuiry, M. Klimov, Y. Obeng, and S. Seal, *Chemical mechanical planarization of copper: Role of oxidants and inhibitors.* Journal of the Electrochemical Society, 2004. **151**(11): p. G788-G794.
26. Tamilmani, S., W. Huang, S. Raghavan, and R. Small, *Potential-pH diagrams of interest to chemical mechanical planarization of copper.* Journal of the Electrochemical Society, 2002. **149**(12): p. G638-G642.
27. Gorantla, V.R.K., E. Matijevic, and S.V. Babu, *Amino acids as complexing agents in chemical-mechanical planarization of copper.* Chemistry of Materials, 2005. **17**(8): p. 2076-2080.
28. Aksu, S. and F.M. Doyle, *Electrochemistry of copper in aqueous ethylenediamine solutions.* Journal of the Electrochemical Society, 2002. **149**(7): p. B340-B347.
29. Gorantla, V.R.K., K.A. Assiongbon, S.V. Babu, and D. Roy, *Citric acid as a complexing agent in CMP of copper investigation of surface reactions using impedance spectroscopy.* Journal of the Electrochemical Society, 2005. **152**(5): p. G404-G410.
30. Cotton, J.B. and I.R. Scholes, *Benzotriazole and Related Compounds as Corrosion Inhibitors for Copper.* British Corrosion Journal, 1967. **2**: p. 1-5.
31. Rubim, J., I.G.R. Gutz, O. Sala, and W.J. Orvillethomas, *Surface Enhanced Raman-Spectra of Benzotriazole Adsorbed on a Copper Electrode.* Journal of Molecular Structure, 1983. **100**(JUL): p. 571-583.

32. Youda, R., H. Nishihara, and K. Aramaki, *Sers and Impedance Study of the Equilibrium between Complex-Formation and Adsorption of Benzotriazole and 4-Hydroxybenzotriazole on a Copper Electrode in Sulfate-Solutions.* Electrochimica Acta, 1990. **35**(6): p. 1011-1017.
33. Youda, R., H. Nishihara, and K. Aramaki, *A Sers Study on Inhibition Mechanisms of Benzotriazole and Its Derivatives for Copper Corrosion in Sulfate-Solutions.* Corrosion Science, 1988. **28**(1): p. 87-96.
34. Toernkvist, C., D. Thierry, J. Bergman, B. Liedberg, and C. Leygraf, *Methyl substitution in benzotriazole and its influence on surface structure and corrosion inhibition.* Journal of the Electrochemical Society, 1989. **136**(1): p. 58-64.
35. Nilsson, J.O., C. Tornkvist, and B. Liedberg, *Photoelectron and Infrared Reflection Absorption-Spectroscopy of Benzotriazole Adsorbed on Copper and Cuprous-Oxide Surfaces.* Applied Surface Science, 1989. **37**(3): p. 306-326.
36. Cohen, S.L., V.A. Brusic, F.B. Kaufman, G.S. Frankel, S. Motakef, and B. Rush, *X-Ray Photoelectron-Spectroscopy and Ellipsometry Studies of the Electrochemically Controlled Adsorption of Benzotriazole on Copper Surfaces.* Journal of Vacuum Science & Technology a-Vacuum Surfaces and Films, 1990. **8**(3): p. 2417-2424.
37. Xue, G., J.F. Ding, P. Lu, and J. Dong, *Sers, Xps, and Electroanalytical Studies of the Chemisorption of Benzotriazole on a Freshly Etched Surface and an Oxidized Surface of Copper.* Journal of Physical Chemistry, 1991. **95**(19): p. 7380-7384.
38. Cho, K., J. Kishimoto, T. Hashizume, and T. Sakurai, *An Observation of Benzotriazole (Bta) Adsorption on Cu(110) by the Ultra-High-Vacuum (Uhv) Scanning Tunneling Microscope (Stm) and Low-Energy-Electron Diffraction (Leed).* Japanese Journal of Applied Physics Part 2-Letters, 1994. **33**(1B): p. L125-L128.
39. Vogt, M.R., W. Polewska, O.M. Magnussen, and R.J. Behm, *In situ STM study of (100) Cu electrodes in sulfuric acid solution in the presence of benzotriazole - Adsorption, Cu corrosion, and Cu deposition.* Journal of the Electrochemical Society, 1997. **144**(5): p. L113-L116.
40. Vogt, M.R., R.J. Nichols, O.M. Magnussen, and R.J. Behm, *Benzotriazole adsorption and inhibition of Cu(100) corrosion in HCl: A combined in situ STM and in situ FTIR spectroscopy study.* Journal of Physical Chemistry B, 1998. **102**(30): p. 5859-5865.
41. Metikos-Hukovic, M., R. Babic, and A. Marinovic, *Spectrochemical characterization of benzotriazole on copper.* Journal of the Electrochemical Society, 1998. **145**(12): p. 4045-4051.

42. Brusic, V., M.A. Frisch, B.N. Eldridge, F.P. Novak, F.B. Kaufman, B.M. Rush, and G.S. Frankel, *Copper Corrosion with and without Inhibitors.* Journal of the Electrochemical Society, 1991. **138**(8): p. 2253-2259.
43. Chen, J.H., Z.C. Lin, S. Chen, L.H. Nie, and S.Z. Yao, *An XPS and BAW sensor study of the structure and real-time growth behaviour of a complex surface film on copper in sodium chloride solutions (pH=9), containing a low concentration of benzotriazole.* Electrochimica Acta, 1998. **43**(3-4): p. 265-274.
44. Babic, R., M. Metikos-Hukovic, and M. Loncar, *Impedance and photoelectrochemical study of surface layers on Cu and Cu-10Ni in acetate solution containing benzotriazole.* Electrochimica Acta, 1999. **44**(14): p. 2413-2421.
45. Laibinis, P.E., G.M. Whitesides, D.L. Allara, Y.T. Tao, A.N. Parikh, and R.G. Nuzzo, *Comparison of the Structures and Wetting Properties of Self-Assembled Monolayers of Normal-Alkanethiols on the Coinage Metal-Surfaces, Cu, Ag, Au.* Journal of the American Chemical Society, 1991. **113**(19): p. 7152-7167.
46. Laibinis, P.E., C.D. Bain, and G.M. Whitesides, *Attenuation of Photoelectrons in Monolayers of Normal-Alkanethiols Adsorbed on Copper, Silver, and Gold.* Journal of Physical Chemistry, 1991. **95**(18): p. 7017-7021.
47. Laibinis, P.E., R.G. Nuzzo, and G.M. Whitesides, *Structure of Monolayers Formed by Coadsorption of 2 Normal-Alkanethiols of Different Chain Lengths on Gold and Its Relation to Wetting.* Journal of Physical Chemistry, 1992. **96**(12): p. 5097-5105.
48. Ishibashi, M., M. Itoh, H. Nishihara, and K. Aramaki, *Permeability of alkanethiol self-assembled monolayers adsorbed on copper electrodes to molecular oxygen dissolved in 0.5 m Na2SO4 solution.* Electrochimica Acta, 1996. **41**(2): p. 241-248.
49. Haneda, R., H. Nishihara, and K. Aramaki, *Chemical modification of an alkanethiol self-assembled layer to prevent corrosion of copper.* Journal of the Electrochemical Society, 1997. **144**(4): p. 1215-1221.
50. Jennings, G.K., J.C. Munro, and P.E. Laibinis, *Effects of film crystallinity on the protective properties of self-assembled monolayers of alkanethiols on copper.* Advanced Materials, 1999. **11**(12): p. 1000-1003.
51. Jennings, G.K., J.C. Munro, T.H. Yong, and P.E. Laibinis, *Effect of chain length on the protection of copper by n-alkanethiols.* Langmuir, 1998. **14**(21): p. 6130-6139.
52. Feng, Y., W.-K. Teo, K.-S. Siow, Z. Gao, K.-L. Tan, and A.-K. Hsieh, *Corrosion protection of copper by a self-assembled monolayer of alkanethiol.* Journal of the Electrochemical Society, 1997. **144**(1): p. 55-64.

53. Jennings, G.K. and P.E. Laibinis, *Self-assembled monolayers of alkanethiols on copper provide corrosion resistance in aqueous environments.* Colloids and Surfaces a-Physicochemical and Engineering Aspects, 1996. **116**(1-2): p. 105-114.
54. Laibinis, P.E. and G.M. Whitesides, *Self-Assembled Monolayers of N-Alkanethiolates on Copper Are Barrier Films That Protect the Metal against Oxidation by Air.* Journal of the American Chemical Society, 1992. **114**(23): p. 9022-9028.
55. Scherer, J., M.R. Vogt, O.M. Magnussen, and R.J. Behm, *Corrosion of alkanethiol-covered Cu(100) surfaces in hydrochloric acid solution studied by in-situ scanning tunneling microscopy.* Langmuir, 1997. **13**(26): p. 7045-7051.
56. Whelan, C.M., M. Kinsella, H.M. Ho, and K. Maex, *Corrosion inhibition by thiol-derived SAMs for enhanced wire bonding on Cu surfaces.* Journal of the Electrochemical Society, 2004. **151**(2): p. B33-B38.
57. Zamborini, F.P., J.K. Campbell, and R.M. Crooks, *Spectroscopic, voltammetric and electrochemical scanning tunneling microscopic study of underpotentially deposited Cu corrosion and passivation with self-assembled organomercaptan monolayers.* Langmuir, 1998. **14**(3): p. 640-647.
58. Lusk, A.T. and G.K. Jennings, *Characterization of self-assembled monolayers formed from sodium S-alkyl thiosulfates on copper.* Langmuir, 2001. **17**(25): p. 7830-7836.
59. Baba, H. and T. Kodama, *Corrosion inhibition and characteristics of the triazinedithiol surface film on copper under potentiostatic anodization.* Corrosion Science, 1999. **41**(10): p. 1987-2000.
60. Beccaria, A.M. and C. Bertolotto, *Inhibitory action of 3-trimethoxysilylpropanethiol-1 on copper corrosion in NaCl solutions.* Electrochimica Acta, 1997. **42**(9): p. 1361-1371.
61. Marconato, J.C., L.O. Bulhoes, and M.L. Temperini, *A spectrocelectrochemical study of the inhibition of the electrode process on copper by 2-mercaptobenzothiazole in ethanolic solutions.* Electrochimica Acta, 1998. **43**(7): p. 771-780.
62. Tremont, R. and C.R. Cabrera, *Electrochemical and surface analysis study of copper corrosion protection by 1-propanethiol and propyltrimethoxysilane: A comparison with 3-mercaptopropyltrimethoxysilane.* Journal of Applied Electrochemistry, 2002. **32**(7): p. 783-793.
63. Preston, F.W., *The Theory and Design of Plate Glass Polishing Machines.* Journal of the Society of Glass Technology, 1927. **11**: p. 214.

64. Liu, C.W., B.T. Dai, W.T. Tseng, and C.F. Yeh, *Modeling of the wear mechanism during chemical-mechanical polishing.* Journal of the Electrochemical Society, 1996. **143**(2): p. 716-721.
65. Haque, T., S. Balakumar, A.S. Kumar, and M. Rahman, *A Material Removal Rate Model for Copper Abrasive-Free CMP.* Journal of the Electrochemical Society, 2005. **152**(6): p. G417-G422.
66. Tseng, W.T. and Y.L. Wang, *Re-examination of pressure and speed dependences of removal rate during chemical-mechanical polishing processes.* Journal of the Electrochemical Society, 1997. **144**(2): p. L15-L17.
67. Luo, Q., S. Ramarajan, and S.V. Babu, *Modification of the Preston equation for the chemical-mechanical polishing of copper.* Thin Solid Films, 1998. **335**(1-2): p. 160-167.
68. Zhao, B. and F.G. Shi, *Chemical mechanical polishing: Threshold pressure and mechanism.* Electrochemical and Solid State Letters, 1999. **2**(3): p. 145-147.
69. Shi, F.G. and B. Zhao, *Modeling of chemical-mechanical polishing with soft pads.* Applied Physics a-Materials Science & Processing, 1998. **67**(2): p. 249-252.
70. Kaufman, F.B., D.B. Thompson, R.E. Broadie, M.A. Jaso, W.L. Guthrie, D.J. Pearson, and M.B. Small, *Chemical-Mechanical Polishing for Fabricating Patterned W Metal Features as Chip Interconnects.* Journal of the Electrochemical Society, 1991. **138**(11): p. 3460-3465.
71. Kneer, E.A., C. Raghunath, S. Raghavan, and J.S. Jeon, *Electrochemistry of chemical vapor deposited tungsten films with relevance to chemical mechanical polishing.* Journal of the Electrochemical Society, 1996. **143**(12): p. 4095-4100.
72. Paul, E., *A model of chemical mechanical polishing.* Journal of the Electrochemical Society, 2001. **148**(6): p. G355-G358.
73. Paul, E., *Application of a CMP model to tungsten CMP.* Journal of the Electrochemical Society, 2001. **148**(6): p. G359-G363.
74. Paul, E., *A model of chemical mechanical polishing - II. Polishing pressure and speed.* Journal of the Electrochemical Society, 2002. **149**(5): p. G305-G308.
75. Paul, E. and R. Vacassy, *A model of CMP - III. Inhibitors.* Journal of the Electrochemical Society, 2003. **150**(12): p. G739-G743.
76. Paul, E., F. Kaufman, V. Brusic, J. Zhang, F. Sun, and R. Vacassy, *A model of copper CMP.* Journal of the Electrochemical Society, 2005. **152**(4): p. G322-G328.
77. Curie, P. and J. Curie, C.R. Acad. Sci, 1880. **91**: p. 293.

78. Sauerbrey, G., *Use of crystal oscillators for weighing thin films and for microweighing.* Zeitschrift fuer Physik, 1959. **155**(2): p. 206-222.
79. Heising, R.A., *Quartz Crystals for Electrical Circuits*. 1946, Van Nostrand, New York: Electronic Industries Association.
80. Bottom, V.E., *Introduction to Quartz Crystal Unit Design*. 1982: Van Nostrand Reinhold Company.
81. Janshoff, A., H.-J. Galla, and C. Steinem, *Piezoelectric mass-sensing devices as biosensors - An alternative to optical biosensors?* Angewandte Chemie (International Edition in English), 2000. **39**(22): p. 4005-4032.
82. O'Sullivan, C.K. and G.G. Guilbault, *Commercial quartz crystal microbalances - theory and applications.* Biosensors & Bioelectronics, 1999. **14**(8-9): p. 663-670.
83. A. Janshoff, C.S., *Quartz Crystal Microbalance for Bioanalytical Applications.* Sensors Update, 2001. **9**(1): p. 313-354.
84. Buttry, D.A. and M.D. Ward, *Measurement of Interfacial Processes at Electrode Surfaces with the Electrochemical Quartz Crystal Microbalance.* Chemical Reviews, 1992. **92**(6): p. 1355-1379.
85. Hillier, A.C. and M.D. Ward, *Scanning electrochemical mass sensitivity mapping of the quartz crystal microbalance in liquid media.* Analytical Chemistry, 1992. **64**(21): p. 2539.
86. Konash, P.L. and G.J. Bastiaans, *Piezoelectric-Crystals as Detectors in Liquid-Chromatography.* Analytical Chemistry, 1980. **52**(12): p. 1929-1931.
87. Kanazawa, K.K. and J.G. Gordon, *Frequency of a quartz microbalance in contact with liquid.* Anal. Chem., 1985. **57**(8): p. 1770-1771.
88. Kanazawa, K.K. and J.G. Gordon, *The Oscillation Frequency of a Quartz Resonator in Contact with a Liquid.* Analytica Chimica Acta, 1985. **175**(SEP): p. 99-105.
89. Ward, M.D. and D.A. Buttry, *Insitu Interfacial Mass Detection with Piezoelectric Transducers.* Science, 1990. **249**(4972): p. 1000-1007.
90. Salt, D., *Hy-Q handbook of Quartz Crystal Devices*. 1987, Berkshire, England: van Nostrand Reinhold (UK) Co. Ltd.

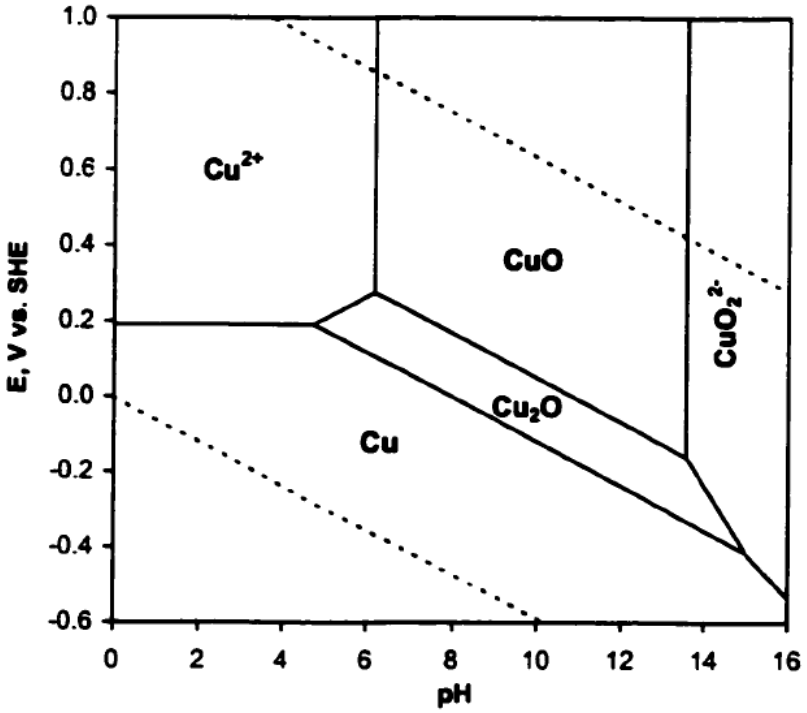

Figure 2.1 Potential-pH equilibrium diagram for Cu-water system at 25 °C[1].

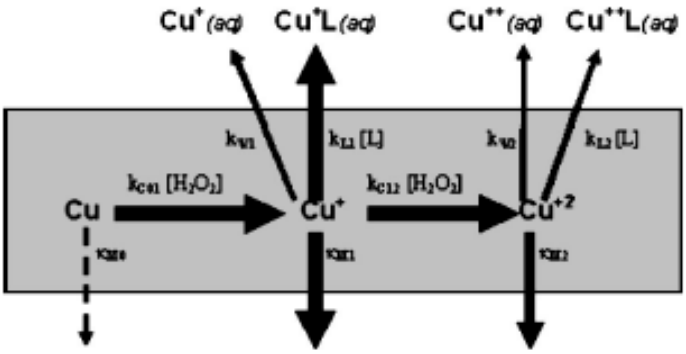

Figure 2.2 Schematic diagram for chemical reactions in Cu-CMP according to Paul model [76]. Various chemical and mechanical reactions are expressed in a simple kinetic rate model.

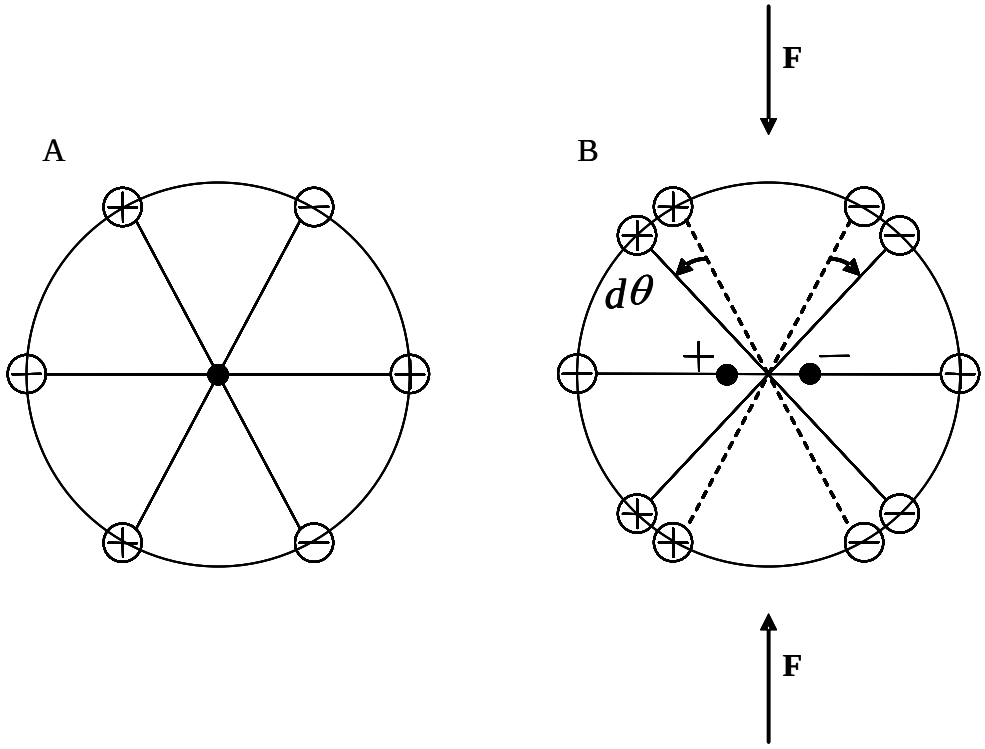

Figure 2.3 A model of a unit cell in quartz crystal (A) and piezoelectric effect by applying mechanical stress (B) (adapted from [90]).

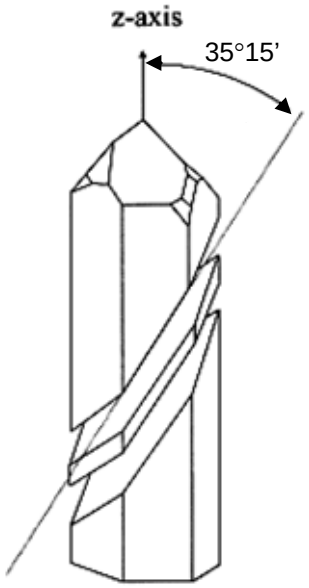

Figure 2.4 Alpha quartz crystals and AT-cut that has angle of 35 ° 15 ′ relative to z-axis[81].

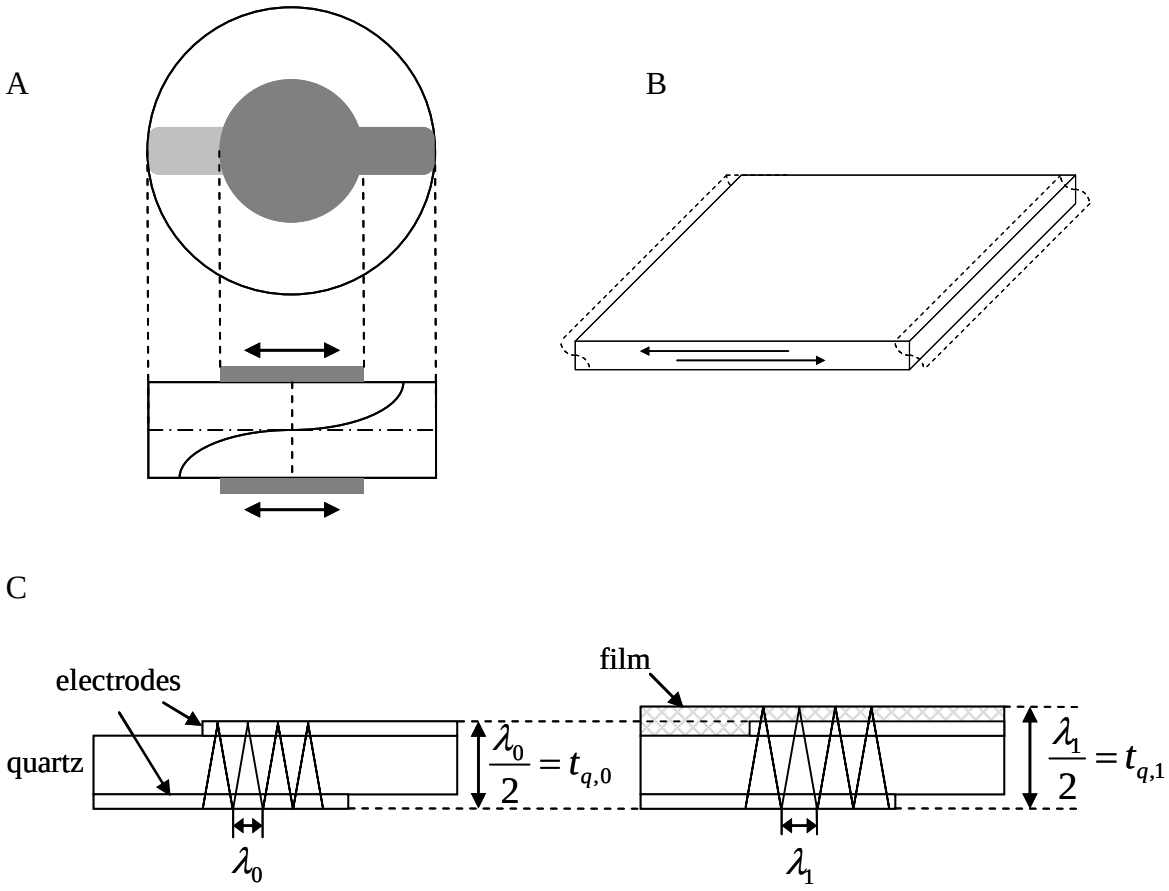

Figure 2.5 Quartz crystal resonator (A), thickness shear mode vibration (B), and surface acoustic wave (C) (adapted from [81] and [84]). Surface acoustic wave is created by applying alternating potentials through metal electrodes on both sides of quartz crystal. When an additional layer is formed, the resonant frequency of acoustic wave is decreased, which is proportional to the increased weight.

Chapter 3. Copper Etching Rate Study in Contact with Glycine, H_2O_2, and Benzotriazole at Low pH

3.1 Abstract

The impact of benzotriazole (BTA), glycine, and H_2O_2 on copper etching in aqueous media at pH 2 was studied. Etching rate of copper in contact with the chemicals was measured by in-situ real time quartz crystal microgravimetry (QCM). Kinetics of chemical reactions between copper and the chemicals were studied by fitting the measurement with an etching rate formula that contained kinetic rate constants. QCM measurement and kinetic analysis broadened understanding of fundamental chemical reactions. In the absence of other chemical agents, copper etching rate was dependent on pH in aqueous solutions. At low pH, metallic copper was a dominant surface site and removed at a constant rate for a pH. Glycine, which was known as a complexing agent, reduced copper etching rate at pH 2 by depriving oxide ions that oxidized metallic copper for dissolution. H_2O_2 increased etching rate significantly by oxidizing metallic copper to more soluble copper oxide. BTA reduced etching rate considerably by Langmuir-type inhibitive adsorption isotherm. Additive etching rate model was developed based on detailed reaction kinetics of the chemical agents with copper. Chemical components interacted with one another as well as copper surface. When put together, H_2O_2 suppressed the inhibition effect of BTA while the presence of glycine had little impact on chemical actions of H_2O_2 and BTA. The additive model was compensated for the secondary impacts that arose among chemical components, which was the major difference with Paul's model. H_2O_2 was a dominating factor compared with the other two components to control copper etching rate at pH 2.

3.2 Introduction

Solid copper has a variety of applications in industry such as electronic wires, coinage, tubing for plumbing, heating, and air-conditioning and hence copper chemistry has been studied for decades due to its importance and economic impact in industry. One of the major research interests was corrosion prevention in order to prolong the lifetime of copper products and to reduce environmental contamination by dissolved copper ions[1, 2]. Recently, Damascene and chemical mechanical polishing (CMP) processes have been introduced to create interconnect lines in integrated circuit (IC) chip making procedure[3-5], which extended copper applications to semiconductor industry. Damascene process electrodeposits copper to form interconnect wires, which produces a necessary overburden. The following CMP step removes the overburden and planarizes the surface for subsequent layers formation. CMP is carried out by combination of mechanical abrasion and chemical corrosion and the performance is determined by material removal rate and surface planarity. It is required to improve the CMP performance for reducing production time and quality enhancement of IC chips. One of the main hurdles to achieve maximum CMP performance is insufficient knowledge about the chemical reactions provided by a variety of chemical components so that it limits component selection and its proper concentration, etc.

Four classes of chemicals are generally known to have considerable impacts on copper etching in aqueous solution, which includes inhibitor, oxidizer, complexing agent, and pH. It is pH that has the most significant impact on copper etching since it determines the surface oxidation state of copper and chemical agents change their forms according to pH. For instance, Cu/Cu^{2+} is at equilibrium at low pH while $Cu/Cu_2O/CuO$ is more stable at higher pH as it appears in Pourbaix diagram (Figure 2.1)[6]. In addition, one of the complexing agents, glycine changes its chemical forms depending on pH[7, 8]. Inhibitor is widely studied for copper corrosion protection. Benzotriazole (BTA) and its derivatives are well known as effective inhibitors[9-13]. They form protective layers on copper surface and decrease dissolution by physically reducing the contact with solution[14]. Triazole ring in

BTA is combined with copper surface to form protective complexes[12] and its orientation depends on surface structure of copper[15]. Inhibitive adsorption follows the Langmuir adsorption isotherm at low concentration, which is converted to polymeric complexes at high concentration[16]. Oxidizing agent provides control of copper oxidation states without changing pH, where different oxidation states of copper have different chemical and mechanical properties. Representative oxidizers include H_2O_2[17, 18], IO_3^-[19], $K_2Cr_2O_7$[20], etc. Complexing agents combine with copper molecules to form soluble species and accelerate etching rate. The presence of glycine[8] or ethylenediamine[21] changes potential-pH equilibrium diagrams from those in aqueous solution.

Qualitative information about the major chemical reactions is available as stated above and several CMP rate models have been developed based on this insufficient information to explain material removal rate or chemical dissolution rate as a function of mechanical abrasion or chemical components. Preston model is generally accepted as the first CMP rate model[22]. However, Preston explained material removal rate as a function of mechanical terms without consideration of chemical effects. More advanced CMP model that incorporates chemical impacts was developed by Kaufman[23]. Kaufman described CMP process as an alternating process of chemical corrosion to form a soft layer that is removed by mechanical abrasion. However, Kaufman model is still limited as a qualitative description and no detailed chemical information is acquired. It is quite recent that semi quantitative model was developed considering major chemical reactions in kinetic expressions. Paul adopted simplified kinetic expressions for major chemical reactions and mechanical abrasion and then combined to produce an expression for overall material removal rate[24]. Paul explained the rate of tungsten CMP as a function of oxidizer, inhibitor, and mechanical contribution[25-27]. Copper CMP (Cu-CMP) rate was also explained by Paul model as a function of oxidizer concentration and mechanical terms[28].

The main idea of Paul model is that the various chemical and mechanical reactions are separable and additive combination of the individual rate expressions could give a quantitative CMP rate model. Paul demonstrated that simple combination of various kinetic expressions could explain dissolution rate or material removal rate as a function of chemical composition or mechanical components. Paul model significantly improves CMP model by drifting the modeling from qualitative to quantitative stage. However, Paul did not study individual reactions for kinetic information and hence their model is still lack of fundamental understanding, missing some important factors, such as pH, and oversimplifying some chemical reactions.

In this study, we will investigate elementary chemical reactions first and clarify their quantitative kinetic expressions. Once the fundamental chemistries are elucidated, an additive etching rate model that incorporates complete kinetic expressions will be developed. The additive model is tested for more complex systems that contain multiple chemical agents and modified for deviations from predicted values. Copper etching rate is measured by *in-situ* quartz crystal microgravimetry (QCM) to investigate chemical reactions of glycine, hydrogen peroxide, and BTA with copper.

3.3 Experimental

Materials and Reagents: Chemical agents were used as received. Hydrogen peroxide were received from Fisher scientific (Pittsburgh, PA). Benzotriazole (BTA) and glycine were received from Alfa Aesar (Ward Hill, MA). 18 MΩ Deionized water (Nanopure, Barnstead, Dubuque, IA) was used to prepare all aqueous solutions. pH was adjusted by using sodium hydroxide (Mallinckrodt Bolder inc., Hazelwood, MO) or sulfuric acid (Fisher Scientific). Prepared solutions were deaerated by N_2 for 30 min before use.

Sample preparation: Samples were prepared by depositing copper on gold coated quartz crystal. Gold coated AT-cut 10 MHz quartz crystal was received from Elchema corp.

(Potsdam, New York). The quartz crystal disk had 14 mm diameter and 0.166 mm thickness. Gold was coated at center on both sides of the quartz crystal with 5 mm diameter and connected to steel contact. 99.9 % pure copper wire was received from Goodfellow (Devon, PA) and deposited on gold by 100 nm vacuum evaporator (DV-502A, Denton Vacuum, Moorestown, NJ) for QCM measurement.

Quartz crystal microgravimetry (QCM): Copper etching rate was measured in real time by quartz crystal microgravimetry (QCM) with a flow cell system (Figure 3.1). Fast response (1-5 ms) and high sensitivity (< 1 ng) were the main reason to select QCM as a real time measurement tool. Steel contact that was linked to gold film on each side of quartz crystal was connected to frequency measurement system (EQCN-700, Elchema, Potsdam, NY). Prepared solutions were injected through a tube by a syringe pump (Genie Kent, Kent Scientific Corp., Torrington, CT) at a constant flow rate (1 ml / hr). The flow rate of solution was adjusted to minimize the frequency fluctuation while keeping the solutions to flow continuously. Copper deposited side was faced with introducing solutions and the other side was exposed to the air. The flow cell system and quartz crystal were placed inside a Faraday cage (Elchema, Potsdam, NY) to minimize noise.

Electrochemistry: Electrochemical measurement was carried out by chi 760B workstation (CH instruments inc., Austin, TX). Pt disk electrode that has 1/16 inch diameter was used for cyclic voltammetry in gas controlled aqueous solutions. Hg_2SO_4 and Pt/Ir electrodes were used as reference and counter electrodes, respectively. For open circuit potential measurement in pH controlled solutions, copper wire with 0.25 mm diameter was used.

3.4 Results and discussion

Prior to the investigation about chemical reactions, it is required to clarify how copper responds to pH in aqueous solutions in the absence of chemical agents. Thermodynamic data

is available for copper in aqueous solutions [6]. According to the Pourbaix diagram (Figure 2.1), copper has different equilibrium states and outermost surface, depending on solution pH. The pH regions are divided for corrosion or passivation in this thermodynamic diagram. However, the thermodynamic diagram does not provide kinetic information about corrosion rate or passivation. In-situ QCM is employed to study the kinetics. In QCM measurement, observed frequency change is directly related with mass change by Sauerbrey's equation (2.9) and hence corrosion rate or passivation layer formation can be measured. Figure 3.2A shows an example of real time measurement for etching at pH 2 and for passivation at pH 9. The frequency increase at pH 2 represents that material is removed because the mass change is negatively proportional to frequency change and the straight line of frequency increase indicates that the removal rate is constant. When a solution at high pH is introduced following the pH 2 solution, the frequency increase is retarded and finally stopped, indicating passivation. The amount of frequency decrease is proportional to the added weight of hydroxide ions. Please note that the exact chemical composition of passivation layer is not clear and still controversial[1, 6, 29-31]. We will use the term, passivation layer, here for convenience. Dissolution rate is obtained by dividing the slope (df/dt) by sensitivity constant (C_f: 2.26×10^8 Hz cm^2 g^{-1}) and copper density (d_{Cu}: 8.93 g cm^{-3}).

$$\frac{dh}{dt} = \frac{df}{dt}\frac{1}{C_f d_{Cu}} \tag{3.1}$$

Approximate passivation layer thickness is obtained by considering increased weight of hydroxide ions (OH^-), molecular weight ($MW_{Cu(OH)2}$), and density ($d_{Cu(OH)2}$) of copper hydroxide, $Cu(OH)_2$, for convenience.

$$\Delta h_{Cu(OH)_x} \approx \Delta f \frac{MW_{Cu(OH)_2}}{C_f 2MW_{OH} d_{Cu(OH)_2}} \tag{3.2}$$

Figure 3.2B presents the etching rate change and the passivation layer thickness depending on pH. The observed etching rate change and passivation correspond with the region of

corrosion and passivation in the Pourbaix diagram. Figure 3.2B not only agrees with thermodynamic diagram but also provides kinetic information. In order to explain the kinetic aspects, oxidation mechanism of copper must be considered.

At low pH, metallic copper is removed from the surface at a constant rate.

$$Cu \rightarrow Cu^{2+} + 2e^{-} \qquad r_{0,D} = k_{0D} n_0 \tag{3.3}$$

$r_{0,D}$ is reaction rate for dissolution of metallic copper, k_{0D} is kinetic rate constant, and n_0 is surface site density of metallic copper. As pH is increased, the surface is passivated by combination with hydroxide ions.

$$Cu_{(s)} + xOH^{-}_{(aq)} \underset{\longleftarrow}{\longrightarrow} Cu(OH)_{x(s)} + xe^{-} \qquad K_{pv} = \frac{\theta_p}{\theta_0 \left[OH^{-}\right]^x} \tag{3.4}$$

K_{pv} is equilibrium constant for the passivation reaction, θ_0 (n_0/n_T) and θ_p (n_p/n_T) are the relative surface site densities of Cu and $Cu(OH)_x$ against the total surface site density (n_T), respectively, and x is a constant. The relative amount of θ_0 and θ_p depends on each other by the oxidation reaction (3.4) and their summation is unity ($\theta_0 + \theta_p = 1$). Therefore, θ_0 that depends on pH is related with K_{pv} by

$$\theta_0 = \frac{1}{1 + K_{pv}\left[OH^{-}\right]^x} \tag{3.5}$$

The copper dissolution rate that depends on pH can be re-expressed as an etching rate constant (R_0) multiplied by the relative surface site density (θ_0) that is available for etching.

$$R_{pH} = R_0 \theta_0 \qquad (0< \text{pH} <13) \tag{3.6}$$

R_{pH} is dissolution rate that depends on pH in [nm min^{-1}] and R_0 is etching rate constant that is proportional to the kinetic rate constant, k_{0D} ($R_0 = k_{0D} n_T / d_{Cu}$, d_{Cu} represents density of Cu). Solid line in Figure 3.2B represents R_{pH} and fits measured data well with the values of K_{pv} equal to 5.20×10^{10} and x equal to 1.00. The fact that the value of x is equal to one represents

the formation cuprous hydroxide $Cu(OH)_1$. Although cuprous hydroxide is unfavorable thermodynamically, it is a representative of complex structures of passivation film on the surface.

Depending on pH, copper surface is represented by either metallic copper or passivation layers that have different chemical properties. This chapter focuses on the reactions of metallic copper at low pH and pH 2 is selected for study where R_{pH} is 0.35 nm min^{-1} (measured, calculated R_{pH} is 0.41 nm min^{-1}). At low pH, copper requires oxygen to be etched[6] and hence we observed etching rate change according to purging time with oxygen (Figure 3.3). Note that the first data point in Figure 3.3 (etching rate at 0 min of O_2 purging) represents the etching rate after purging with N_2 for 30 min. Contrary to our expectation, etching rate is not increasing with more purging time by O_2. We checked how oxygen concentration was changing according to time after purging with N_2. Figure 3.4A shows cyclic voltammetry (CV) of Pt in 1 mol l^{-1} H_2SO_4 solution with Hg_2SO_4 as a reference electrode (RE) and Pt/Ir as a counter electrode (CE) after purging with N_2 for 30 min (N_2 purged) and O_2 for 10 min (O_2 saturated). After 4.5 hours since N_2 purging, CV curve shifted toward the saturated CV curve, indicating O_2 was diffused into the solution. The peak current density during cathodic scan is due to the reduction of PtO_x that was oxidized during anodic scan and corresponds to the amount of O_2 in solution. The solubility of O_2 in aqueous solution follows Henry's law and at 25°C it is 0.258 mol l^{-1}[32]. Figure 3.4B shows O_2 concentration change in solution according to time after purging with N_2. After about 4 hours, O_2 concentration in solution reaches to about 10 % of saturation or 3×10^{-2} mol l^{-1} or so. Etching rate measurement using QCM normally takes 2 to 6 hours and hence the solution contains more than about 1.5×10^{-2} mol l^{-1} of O_2 concentration. Etching rate measurement in Figure 3.3 shows that this amount of O_2 is enough not to limit copper dissolution. It was checked by open circuit potential (OCP, E_{OC}) measurement of copper in pH controlled solutions. The open circuit potential is mixed potentials determined by anodic (copper

corrosion) or cathodic (oxygen reduction) reaction. Figure 3.5 shows that the change of OCP in solutions after 4 hours of purging either by O_2 or N_2 and OCP is not much different no matter whether the solutions are purged by O_2 or N_2. It demonstrates that copper corrosion is not limited by oxygen reduction or concentration in solution.

Addition of a chemical agent changes the etching rate by interaction with copper surface. Figure 3.6 shows overall etching rate change when glycine is included. Glycine inclusion does not improve but reduces etching rate. Glycine is known as a complexing agent that combines with cupric ions (Cu^{2+}) to form soluble species and changes thermodynamic stability of copper. In aqueous solutions, glycine exists as a cation ($^{+}H_3NCH_2COOH,\ GH_2^+$) at low pH and is reduced to zwitterion ($^{+}H_3NCH_2COO^{-},\ GH^{+-}$) and anion ($H_2NCH_2COO^{-}$, G^-) at higher pH. Their relative amounts at equilibrium depend on pH in aqueous solutions[7].

$$GH^{+-} + H^+ = GH_2^+ \qquad pH = 2.350 + \log\left\{\frac{[GH^{+-}]}{[GH_2^+]}\right\} \tag{3.7}$$

$$G^- + H^+ = GH^{+-} \qquad pH = 9.778 + \log\left\{\frac{[G^-]}{[GH^{+-}]}\right\} \tag{3.8}$$

In order to understand the etching rate reduction by glycine, corrosion process needs to be considered. The mechanism of copper corrosion in aqueous solution was studied by Ives and Rawson[29]. They speculated that copper etching consists of a series of reactions that involve oxygen as an oxidant and proton as an etchant. Copper is first dissociated into cuprous ions and electrons.

$$Cu_{(s)} \rightleftharpoons Cu_{(s)}^+ + e^- \tag{3.9}$$

The electrons ionize oxygen dissolved in solutions to oxide ions.

$$\frac{1}{4}O_{2(g)} + e^{-} \underset{\longleftarrow}{\longrightarrow} \frac{1}{2}O^{2-}_{(aq)} \tag{3.10}$$

The cuprous ions on the surface and oxide ions combine to form cuprous oxide.

$$Cu^{+}_{(s)} + \frac{1}{2}O^{2-}_{(aq)} \underset{\longleftarrow}{\longrightarrow} \frac{1}{2}Cu_2O_{(s)} \tag{3.11}$$

The cuprous oxides interact with more oxygen and protons to be removed from the surface.

$$\frac{1}{2}Cu_2O_{(s)} + \frac{1}{4}O_{2(g)} + 2H^{+}_{(aq)} \underset{\longleftarrow}{\longrightarrow} Cu^{2+}_{(aq)} + H_2O \tag{3.12}$$

Glycine introduction is believed to consume a fraction (n_{g0}) of the oxide ions produced according to (3.10) and hence decrease oxidation rate of metallic copper.

$$GH^{+}_{2\,(aq)} + \frac{1}{2}O^{2-}_{(aq)} \underset{\longleftarrow}{\longrightarrow} GH^{+-}{}_{(aq)} + \frac{1}{2}H_2O \qquad r_{GDP} = k_{GDP,f}\left[GH^{+}_{2}\right] - k_{GDP,b}\left[GH^{+-}\right] \tag{3.13}$$

r_{GDP} is reaction rate for deprotonation of glycine(GDP) and $k_{GDP,f}$ and $k_{GDP,b}$ represent forward and backward rate constants, respectively. The concentrations of cations and zwitterions are co-related by (3.7) and their summation is total concentration of glycine.

$$\left[GH^{+}_{2}\right] + \left[GH^{+-}\right] = \left[G\right] \tag{3.14}$$

Hence, the reaction rate r_{GDP} can be rewritten in terms of glycine concentration rather than cations and zwitterions by using the equation (3.7) and (3.14)

$$r_{GDP} = \frac{\left[G\right]}{1+10^{pH-2.35}}\left(k_{GDP,f} - k_{GDP,b}10^{pH-2.35}\right) \tag{3.15}$$

Cuprous ions on the surface ($Cu^{+}_{(s)}$) that are not oxidized by $O^{2-}_{(aq)}$ are associated with GH^{+-} and stabilized at surface.

$$Cu^{+}_{(s)} + GH^{+-}_{(aq)} \underset{\longleftarrow}{\longrightarrow} Cu^{+} - GH^{+-}_{(s)} \tag{3.16}$$

Therefore, the amount of $Cu^{+}_{(s)}$ part that is stabilized at surface by coupling with GH^{+-} corresponds to the decreased etching rate. The decrease of etching rate by addition of glycine at low pH was also observed by Du et al.[33] They obtained etching rate of copper by measuring corrosion current and observed decrease by the addition of glycine at pH 2.

Etching rate formula is now updated for glycine solution at low pH.

$$\left(\frac{dh}{dt}\right)_{0,G} = R_{pH\,2} + R_{0,G}[G]^{n_{g0}} \tag{3.17}$$

$R_{0,G}$ is etching rate for glycine at pH 2 and directly related with the kinetic rate constants in equation (3.14) by

$$R_{0,G} = \frac{-\left(k_{GDP,f} - k_{GDP,b}10^{pH-2.35}\right)}{1+10^{pH-2.35}}, \tag{3.18}$$

which is the same expression with r_{GDP} in equation (3.15) excluding [G]. Equations (3.17) and (3.18) show that etching rate at low pH is simply updated by adding another etching term for glycine, which is etching rate, $R_{0,G}$, multiplied by glycine concentration with a factor, n_{g0}, which represents the part of $Cu^{+}_{(s)}$ complexed with glycine and stabilized on the surface. Solid line in Figure 3.6 shows the calculation by equation (3.17) in good agreement with the measured data.

Another important chemical agent is an oxidizer since it provides the control of surface oxidation states that have significant impact on etching rate without changing pH. Hydrogen peroxide, H_2O_2, is a strong oxidizer and the most studied one for CMP applications. Figure 3.7 shows that overall etching rate increases linearly against the concentration of hydrogen peroxide. The prevailing reaction of hydrogen peroxide with copper surface at low pH is oxidation of Cu to CuO. Cupric oxides are the form of dissolution and hydrogen peroxide accelerates the oxidation rate and hence corrosion rate.

$$Cu_{(s)} + H_2O_2 \longrightarrow CuO + H_2O_{(aq)} \qquad r_{0,H} = k_{0H} n_0 [H_2O_2] \tag{3.19}$$

$r_{0,H}$ and k_{0H} are reaction rate and kinetic rate constant respectively for metallic copper oxidation by H_2O_2. Note that the oxidation by H_2O_2 is additional to the gaseous oxidation (3.11). Dissolution of CuO is considered to be fast and both oxidation and dissolution steps are irreversible. Etching rate formula with the inclusion of additional oxidation by H_2O_2 is

$$\left(\frac{dh}{dt}\right)_{0,H} = R_{pH2} + R_{0,H}\left[H_2O_2\right] \tag{3.20}$$

$R_{0,H}$ is primary etching rate constant for Cu in H_2O_2 solutions and directly related to the kinetic rate constant k_{0H} by

$$R_{0,H} = k_{0H}\frac{n_T MW_{Cu}}{N_A d_{Cu}} \tag{3.21}$$

where n_T is total surface site density (=10^{15} atoms cm^{-2}), MW_{Cu} is molecular weight of copper, d_{Cu} is copper density. Kinetic rate constant, k_{0H} is obtained by fitting calculation to the measured data. Solid line in Figure 3.7 represents the calculation by equation (3.14). Etching rate formula is again updated by simple addition of a term that accounts for the oxidation reaction by H_2O_2. Etching rate change by H_2O_2 was studied by several authors[34-36]. Although it was agreed that H_2O_2 oxidized copper, quantitative kinetic information was not provided. A certain amount of glycine was often put together to observe etching rate change according to H_2O_2 concentration without knowing kinetic information about the interaction between glycine and copper surface. They measured dissolution rate according to H_2O_2 concentration at pH 4 where more than 80 % of copper surface was passivated. Hence, it was possible that copper etching rate was limited by glycine complexation when glycine concentration was not high enough. At pH 2, more than 95 % of copper surface is metallic copper and hence glycine is not necessary for copper corrosion, which makes the etching rate increase continuously.

The third chemical component is benzotriazole (BTA) that is known as an inhibitor. BTA forms a film by chemical bonding with copper surface[12, 37, 38]. This passivation film reduces active area for copper corrosion and hence decreases dissolution rate. Figure 3.8

is an example of real time measurements with the introduction of BTA. Solution at pH 2 without BTA is injected first to initiate etching on copper that was initially passivated at high pH (1). Soon, etching reaches a constant rate indicating that oxide layer on surface is removed (2). Then, BTA-containing solution is introduced and etching rate starts decreasing (3), which shows that BTA is forming a film on metallic copper. The reduced etching rate is due mainly to the reduced metallic copper site density (n_0) and to a little amount of BTA weight. Once the film is formed, frequency change is straight and further film formation is not observed (4), indicating that BTA film formation on metallic copper is Langmuir type adsorption.

$$Cu_{(s)} + n_{b0}BTA \underset{\longleftarrow}{\longrightarrow} Cu-BTA_{n_{b0}(s)} \qquad r_{0,B} = k_{0Bf} n_0 [BTA]^{n_{b0}} - k_{0Bb} n_{0B} \qquad (3.22)$$

n_{b0} is a stoichiometric coefficient for BTA adsorption, $r_{0,B}$ is a reaction rate of BTA adsorption on Cu^0, $n_{0,B}$ is surface density of BTA-covered Cu^0, and k_{0Bf} and k_{0Bb} are rate constants for forward and backward reaction of BTA adsorption, respectively. Overall, the etching rate change is mainly by BTA adsorption that reduces n_0 and by a little weight added by adsorbed BTA. Using trial-and-error method, real time surface coverage of BTA on Cu^0 (θ_{0B}) can be reduced from the real time measurement. Theoretical change of $\theta_{0,B}$ can be obtained by considering BTA adsorption isotherm (3.22), where the reaction rate $r_{0,B}$ is equal the rate of BTA-covered surface formation (dn_{0B}/dt).

$$\theta_{0B,t} = \frac{k_{0Bf}[BTA]^{n_{b0}}}{k_{0Bf}[BTA]^{n_{b0}} + k_{0Bb}} \left\{1 - e^{-\left(k_{0Bf}[BTA]^{n_{b0}} + k_{0Bb}\right)t}\right\} \qquad (3.23)$$

Surface coverage ($\theta_{0B,t}$) is a function of rate constants k_{0Bf} and k_{0Bb}, BTA concentration [*BTA*], stoichiometric constant n_{b0}, and time *t*. At steady state, *t* goes to infinity and the last term in the curly brackets on the right hand side of equation (3.23) becomes unity, which removes dependence on *t*. Figure 3.9 shows dynamics (A) and isotherm (B) for BTA adsorption and

measured surface coverage is compared with theoretical expression by equation (3.23). Theoretical calculation fits the measured data very well for both dynamics and isotherm curves. There are two surface sites in the presence of BTA. One is Cu^0 (θ_0) that is available for both etching and BTA adsorption. The other site is BTA-covered Cu^0 (θ_{0B}) that is inactive for etching or further adsorption. Hence, in BTA-containing solution, etching rate change is determined by BTA surface coverage. Overall etching rate change formula is then R_{pH2} multiplied by active surface site (θ_0) and θ_0 is regulated by BTA adsorption.

$$\left(\frac{dh}{dt}\right)_{0,B} = R_{pH2}\theta_0 \tag{3.24}$$

Since the summation of θ_0 and θ_{0B} is close to unity,

$$\theta_0 \approx \frac{k_{0Bb}}{k_{0Bf}[BTA]^{n_{b0}} + k_{0Bb}} \tag{3.25}$$

Overall etching rate at steady state takes a reverse form of adsorption isotherm (Figure 3.9B).

The objective of this study is to develop a quantitative kinetic model for copper dissolution in aqueous solutions. Copper dissolution is a complicated process and complete picture of kinetic mechanism has been lacking, especially when chemical agents are incorporated. One of the complications is due to the existence of multiple copper surface sites and pH control in this study segregated metallic copper from the others, minimizing the number of involved reactions. Kinetic study of glycine, H_2O_2, and BTA with copper at pH 2 elucidated the reaction mechanism, which is a basis for CMP model development. The quantitative description of kinetic processes will also make the CMP model quantitative and the control of CMP process along with slurry preparation will become much more advanced by using this quantitative dissolution rate model. The construction of dissolution rate model follows the idea of Paul's model, that is, to combine the individual etching rate formula additively.

$$\left(\frac{dh}{dt}\right)_0 = \left(R_{pH2} + R_{0,G}[G]^{n_{g0}} + R_{0,H}[H_2O_2]\right)\theta_0 \tag{3.26}$$

θ_0 is given by (3.25). This additive model (3.26) simply combines the previous formulas (3.17), (3.20), and (3.24) without duplication. When the equation (3.26) is used for individual chemical reactions, it successfully predicts as the individual formulas do. The additive formula should predict etching rate for multi-component system without significant deviations if the concept of additive model works.

In order to examine if the additive formula (3.26) works for more complicated systems, two or more components are put together and etching rates are measured. One concentration is chosen for glycine and H_2O_2 and put into each other's solution so that the etching rate is observed for one in the presence of the other. Figure 3.10 shows the measurement for glycine and H_2O_2 bi-component system and prediction by equation (3.26) (dashed line). Etching rate dependence on H_2O_2 is not much different from that with single H_2O_2. Etching rate increases linearly with H_2O_2 concentration increase. Compared with H_2O_2, etching rate dependence on glycine is small. In presence of H_2O_2, it is believed that gaseous oxidation by oxygen (3.11) is negligibly small compared with the oxidation by H_2O_2. Prediction by the additive model shows slight deviations for both systems. These deviations are compensated by incorporating secondary etching rate constants that account for the possible interactions between H_2O_2 and glycine. For instance, the primary etching rate constants $R_{0,G}$ and $R_{0,H}$ are updated to include secondary rate constants $R_{0,GH}$ and $R_{0,HG}$, where the former accounts for impact by H_2O_2 to glycine and the latter by glycine to H_2O_2. Secondary rate constants are multiplied by each component concentration and added to $R_{0,G}$ and $R_{0,H}$.

$$R_{0,G} \longrightarrow R_{0,G} + R_{0,GH}\left[H_2O_2\right] + R_{0,GB}\left[BTA\right] \tag{3.27-1}$$

$$R_{0,H} \longrightarrow R_{0,H} + R_{0,HG}\left[G\right] + R_{0,HB}\left[BTA\right] \tag{3.27-2}$$

$R_{0,GB}$ and $R_{0,HB}$ are secondary constants for BTA with glycine and H_2O_2, respectively. The inclusion of secondary constants represents the change of etching rate dependence on a

chemical component by the presence of another. For instance, chemical state of a component that affects etching rate can be transformed to another, which would cause the etching rate dependence on the chemical agent to change. Detailed information about secondary interactions would require further study and at this moment and they are incorporated by secondary rate constants. Adsorption isotherm term remains unmodified since the modification on that term does not improve the fitting much but makes the etching rate formula complicated. Solid lines in Figure 3.10 represent the fitting with secondary rate constants. Fitting is slightly improved by the incorporation of secondary constants, which indicates weak interaction between glycine and H_2O_2.

Figure 3.11 shows the bi-component measurements and fitting for glycine and BTA. The presence of both BTA and glycine suppresses etching rate significantly. In addition, including secondary rate constants improves the fitting by calculation but the difference is small. The little improvement of fitting by calculation with secondary constants indicates that the presence of BTA or glycine does not affect chemical reaction of the other component considerably. In the same way, H_2O_2 and BTA are put together and etching rate is observed (Figure 3.12). BTA and H_2O_2 bi-component system has a noticeable change. Etching rate is not decreased by BTA, as indicated by the additive model (dashed line) and relatively large gap exists between measured data and the additive model. Etching rate dependence on H_2O_2 is nearly unchanged regardless of BTA or glycine presence. On the other hand, inhibitive effect of BTA nearly disappears in presence of H_2O_2, which indicates H_2O_2 oxidizes not only copper but also BTA so that BTA loses its adsorption capability. The large gap between measured data and prediction by additive model comes from this secondary interaction. Incorporation of secondary etching rate constants updates prediction and fits the measurement.

Three components of glycine, BTA, and H_2O_2 are put together and etching rate is measured (Figure 3.13). Etching rate dependence on glycine is now increasing along with

glycine concentration in the presence of BTA and H_2O_2. Inhibitive etching rate reduction by BTA is not observable again. Compared with glycine and BTA, H_2O_2 has the most significant impact on etching rate. Fitting by calculation using equation (3.26) and (3.27) shows noticeable gap with the measured data. It is hard to prove what tertiary reactions are but it is apparent that the etching rate formula (3.26) and secondary etching rate constants (3.27) need to be updated by incorporating tertiary constants.

$$R_{0,GH} \longrightarrow R_{0,GH} + R_{0,GHB}[BTA] \tag{3.28-1}$$

$$R_{0,GB} \longrightarrow R_{0,GB} + R_{0,GBH}[H_2O_2] \tag{3.28-2}$$

$$R_{0,HG} \longrightarrow R_{0,HG} + R_{0,HGB}[BTA] + R_{HGH}[H_2O_2][BTA] \tag{3.28-3}$$

$$R_{0,HB} \longrightarrow R_{0,HB} + R_{0,HBG}[G] + R_{0,HBH}[H_2O_2][G] \tag{3.28-4}$$

Equation (3.28) shows the expansion of secondary rate constants (3.27) by combining tertiary constants. As an example, $R_{0,GHB}$ represents impact of tertiary reaction by the presence of BTA to the secondary rate constant $R_{0,GH}$. It should be noted that $R_{0,HGH}$ and $R_{0,HBH}$ make up for additional impacts of hydrogen peroxide to BTA adsorption. These terms are added instead of changing kinetic constants for BTA adsorption. Figure 3.13B shows that H_2O_2 is a major component that changes etching rate most significantly, compared with the other two components. It implies that oxidation is a key process to control etching rate at low pH.

The final etching rate model for glycine, H_2O_2, and BTA is given by

$$\left(\frac{dh}{dt}\right)_0 = \left(R_{pH2} + R'_{0,G}[G]^{n_{g0}} + R'_{0,H}[H_2O_2]\right)\left(\frac{k_{0Bb}}{k_{0Bf}[BTA]^{n_{b0}} + k_{0Bb}}\right) \tag{3.29}$$

where the extended primary etching rate constants $R'_{0,G}$ and $R'_{0,H}$ are represented by

$$R'_{0,G} = R_{0,G} + R'_{0,GH}[H_2O_2] + R'_{0,GB}[BTA] \tag{3.30-1}$$

$$R'_{0,H} = R_{0,H} + R'_{0,HG}[G] + R'_{0,HB}[BTA] \tag{3.30-2}$$

and the extended secondary etching rate constants $R'_{0,GH}$, $R'_{0,GB}$, $R'_{0,HG}$, and $R'_{0,HB}$ are represented by

$$R'_{0,GH} = R_{0,GH} + R_{0,GHB}[BTA] \tag{3.31-1}$$

$$R'_{0,GB} = R_{0,GB} + R_{0,GBH}[H_2O_2] \tag{3.31-2}$$

$$R'_{0,HG} = R_{0,HG} + R_{0,HGB}[BTA] + R_{HGH}[H_2O_2][BTA] \tag{3.31-3}$$

$$R'_{0,HB} = R_{0,HB} + R_{0,HBG}[G] + R_{0,HBH}[H_2O_2][G] \tag{3.31-4}$$

The final etching rate model (3.29) is constructed based on the additive model that is directly connected with kinetic mechanisms of chemical reactions of glycine, H_2O_2, and BTA with copper surface. The additive model is insufficient to predict the etching rate of more complicated systems and we tried to compensate for the gap. It presents that the prediction of copper dissolution rate is a complicated task and not only their fundamental chemistries but also the interactions among chemical components must be understood in more detail.

Ideally, all the combinations of chemical compositions need to be measured to prove the etching rate model is accurate, which requires tremendous amount of time to complete. We selected a couple of conditions and measured etching rate to see if the etching rate model is acceptable. Figure 3.14 shows the design of experiment (DOE) for all experimental conditions where ○, △, and × represent single, bi, and tri component conditions. Asterisk (*) represents arbitrarily selected conditions for prediction with the etching rate model. When the concentrations of BTA, glycine, and H_2O_2 are 2×10^{-4} mol l^{-1}, 0.1 mol l^{-1}, and 0.05 mol l^{-1}, respectively, the measured etching rate is 34.5 nm min^{-1} and predicted value is 35.1 nm min^{-1}. When the concentrations of BTA, glycine, and H_2O_2 are 1×10^{-4} mol l^{-1}, 0.04 mol l^{-1}, and 0.05 mol l^{-1}, respectively, the measured etching rate is 20.6 nm min^{-1} and predicted value is 20.2 nm min^{-1}. For both conditions, the prediction by etching rate model

agrees well with experimental measurements. The prediction by etching rate model in (3.29) seems to be acceptable.

Compared with the Paul model, our model deals with more detailed chemical reactions and kinetic mechanisms. The Paul model is based on oversimplified reaction mechanisms without understanding fundamental chemistry of each element. They lump together kinetic constants to create secondary fitting constants that are hardly connected to fundamental chemistries and their reaction mechanisms. The additive model in this study is based on elementary reaction mechanisms and combines their kinetic expressions to form a coherent etching rate model along with compensations. Our model is flexible to include further chemical or even mechanical processes in proper rate expressions. In Cu-CMP, design of slurry is a matter of what and how much of chemical agents are put in. Our model can provide an improved understanding for the connection between the CMP performance and incorporated chemical agents.

3.5 Conclusions

The objective of study in this chapter was to develop a coherent kinetic model for copper dissolution rate in aqueous solutions. The dissolution rate model was expected to be quantitative so that it would be possible to prepare more predictable and more successful slurry for Cu-CMP. Due to the complication of copper corrosion process in aqueous solutions, it was required to study basic kinetics of copper reactions in aqueous solution as a function of pH. Experimental measurement by in-situ QCM showed a good agreement with thermodynamic diagram and provided kinetic information about copper etching or passivation in pH adjusted aqueous solutions. When a complete picture of kinetic model was established, chemical reactions of copper with glycine, hydrogen peroxide, and BTA were investigated at pH 2 where metallic copper is predominant at surface.

At pH 2, glycine introduction decreased copper etching rate. It was speculated that glycine consumed a fraction of oxide ions that corroded metallic copper to copper oxide, which was the form of dissolution. On the other hand, hydrogen peroxide increased etching rate by accelerating oxidation of metallic copper to cupric oxide. BTA introduction reduced etching rate significantly by passivative adsorption on copper surface and the adsorption follows Langmuir adsorption isotherm.

Chemical reactions of glycine, hydrogen peroxide, and BTA were kinetically analyzed and clarified. Control of pH at 2 restricted the copper surface to be metallic copper, which limited the number of involved reactions and hence made it simple to analyze. Additive model of copper dissolution was constructed based on the fundamental kinetics. Elementary reaction rates were speculated to contribute to the dissolution rate additively and hence kinetic rate constants were directly related with the primary etching rate constants in the additive model.

The additive model was testified to see if the model worked for multi-component systems. It was shown that the model agreed with well with glycine-BTA and hydrogen peroxide-glycine system. However, a large gap between the measured data and the model prediction was observed for BTA-hydrogen peroxide system, which indicated a strong secondary interaction between these two chemical agents. BTA lost inhibitive effect in the presence of hydrogen peroxide while etching rate dependence on hydrogen peroxide was not altered much regardless of the presence of BTA. It is believed that hydrogen peroxide oxidize BTA so that BTA loses its inhibitive effect. Secondary interactions of glycine with the other two components were relatively small. The gap between the additive model and measured data was compensated by incorporating secondary etching rate constants. When the three chemical components were put together, hydrogen peroxide was the controlling factor of etching rate and the dependence of dissolution rate on glycine and BTA were relatively small.

The deviations of measured data with second order model were adjusted with incorporating tertiary etching rate constants.

Nomenclature

h : thickness of copper

dh/dt : dissolution rate of copper

df/dt : frequency change rate

C_f : sensitivity constant (=2.26 × 10^8 Hz cm^2 g^{-1})

d_{Cu} : copper density

$r_{0,D}$: reaction rate for dissolution of metallic copper

$r_{0,B}$: reaction rate of BTA adsorption on metallic copper

$r_{0,H}$: reaction rate of copper oxidation by H_2O_2

k_{0D} : kinetic rate constant of dissolution reaction of metallic copper

k_{0H} : reaction rate constant for oxidation reaction by H_2O_2

k_{0Bf} : forward reaction rate constant for BTA adsorption on metallic copper

k_{0Bb} : backward reaction rate constant for BTA adsorption on metallic copper

$k_{GDP,f}$: forward reaction rate constant for glycine deprotonation (GDP)

$k_{GDP,b}$: backward reaction rate constant for glycine deprotonation (GDP)

K_{pv} : equilibrium constant for passivation of metallic copper

θ_p : relative surface site density of passivated copper

θ_0 : relative surface site density of metallic copper

θ_{0B} : relative surface site density of BTA-covered metallic copper

n_0 : surface site density of metallic copper

n_{0B} : surface site density of BTA-covered metallic copper

n_T : total surface site density (=10^{15} atoms cm^{-2})

n_{g0} : fraction constant for glycine complexation with oxide ions

n_{b0} : stoichiometric coefficient for BTA adsorption on metallic copper

$R_{0,G}$: primary etching rate constant for glycine

$R_{0,H}$: primary etching rate constant for glycine

R_{pH} : copper dissolution rate that depends on pH

R_0 : etching rate constant for metallic copper

$R_{0,GH}$: secondary etching rate constant for glycine with H_2O_2

$R_{0,GB}$: secondary etching rate constant for glycine with BTA

$R_{0,HG}$: secondary etching rate constant for $H_2O_2$with glycine

$R_{0,HB}$: secondary etching rate constant for $H_2O_2$with BTA

$R_{0,GHB}$: tertiary etching rate constant for glycine with H_2O_2 and BTA

$R_{0,GBH}$: tertiary etching rate constant for glycine with H_2O_2 and BTA

$R_{0,HGB}$: tertiary etching rate constant for H_2O_2 with glycine and BTA

$R_{0,HGH}$: tertiary etching rate constant for H_2O_2 with glycine and BTA

$R_{0,HBG}$: tertiary etching rate constant for H_2O_2 with BTA and glycine

$R_{0,HBH}$: tertiary etching rate constant for H_2O_2 with glycine and BTA

3.6 References

1. Merkel, T.H. and S.O. Pehkonen, *General corrosion of copper in domestic drinking water installations: Scientific background and mechanistic understanding.* Corrosion Engineering Science and Technology, 2006. **41**(1): p. 21-37.
2. Kear, G., B.D. Barker, and F.C. Walsh, *Electrochemical corrosion of unalloyed copper in chloride media--a critical review.* Corrosion Science, 2004. **46**(1): p. 109-135.
3. Kaanta, C.W., S.G. Bombardier, W.J. Cote, W.R. Hill, G. Kerszykowski, H.S. Landis, D.J. Poindexter, C.W. Pollard, G.H. Ross, J.G. Ryan, S. Wolff, and J.E. Cronin, *Dual Damascene: A ULSI Wiring Technology.* VMIC Conference, 1991: p. 144.
4. Beyer, K.D., W.L. Guthrie, S.R. Makarewicz, E. Mendel, W.J. Patrick, K.A. Perry, W.A. Pliskin, J. Riseman, P.M. Schaible, and C.L. STandley, *Chem-mech Polishing Method for Producing Coplanar Metal/insulator Films on a Substrate*. 1985.
5. Beyer, K.D., W.L. Guthrie, S.R. Makarewicz, E. Mendel, W.J. Patrick, K.A. Perry, W.A. Pliskin, J. Riseman, P.M. Schaible, and C.L. STandley, *Chem-mech Polishing*

Method for Producing Coplanar Metal/insulator Films on a Substrate. U.S. Patent 4,944,836, 1990.

6. Pourbaix, M., *Atlas of Electrochemical Equilibria in Aqueous Solutions*. 1974.
7. Aksu, S. and F.M. Doyle, *Electrochemistry of copper in aqueous glycine solutions.* Journal of the Electrochemical Society, 2001. **148**(1): p. B51-B57.
8. Aksu, S. and F.M. Doyle, *The role of glycine in the chemical mechanical planarization of copper.* Journal of the Electrochemical Society, 2002. **149**(6): p. G352-G361.
9. Cotton, J.B. and I.R. Scholes, *Benzotriazole and Related Compounds as Corrosion Inhibitors for Copper.* British Corrosion Journal, 1967. **2**: p. 1-5.
10. Walker, R., *Benzotriazole as a Corrosion Inhibitor for Immersed Copper.* Corrosion, 1973. **29**(7): p. 290-296.
11. Youda, R., H. Nishihara, and K. Aramaki, *A Sers Study on Inhibition Mechanisms of Benzotriazole and Its Derivatives for Copper Corrosion in Sulfate-Solutions.* Corrosion Science, 1988. **28**(1): p. 87-96.
12. Tornkvist, C., D. Thierry, J. Bergman, B. Liedberg, and C. Leygraf, *Methyl Substitution in Benzotriazole and Its Influence on Surface-Structure and Corrosion Inhibition.* Journal of the Electrochemical Society, 1989. **136**(1): p. 58-64.
13. Brusic, V., M.A. Frisch, B.N. Eldridge, F.P. Novak, F.B. Kaufman, B.M. Rush, and G.S. Frankel, *Copper Corrosion with and without Inhibitors.* Journal of the Electrochemical Society, 1991. **138**(8): p. 2253-2259.
14. Poling, G.W., *Reflection Infra-Red Studies of Films Formed by Benzotriazole on Cu.* Corrosion Science, 1970. **10**(5): p. 359-&.
15. Sugimasa, M., L.J. Wan, J. Inukai, and K. Itaya, *Adlayers of benzotriazole on Cu(110), (100), and (111) in HClO4 solution - In situ scanning tunneling microscopy study.* Journal of the Electrochemical Society, 2002. **149**(10): p. E367-E373.
16. Babic, R., M. Metikos-Hukovic, and M. Loncar, *Impedance and photoelectrochemical study of surface layers on Cu and Cu-10Ni in acetate solution containing benzotriazole.* Electrochimica Acta, 1999. **44**(14): p. 2413-2421.
17. Ein-Eli, Y., E. Abelev, and D. Starosvetsky, *Electrochemical behavior of copper in conductive peroxide solutions.* Journal of the Electrochemical Society, 2004. **151**(4): p. G236-G240.
18. Lu, J., J.E. Garland, C.M. Pettit, S.V. Babu, and D. Roy, *Relative roles of H2O2 and glycine in CMP of copper studied with impedance spectroscopy.* Journal of the Electrochemical Society, 2004. **151**(10): p. G717-G722.

19. Anik, M., *Reduction characteristics of iodate ion on copper: Application to copper chemical mechanical polishing.* Journal of Applied Electrochemistry, 2004. **34**(9): p. 963-969.
20. Lee, B.-C., D.J. Duquette, and R.J. Gutmann. *Synthesis of model alumina slurries for damascene patterning of copper*. in *Chemical - Mechanical Polishing 2001 - Advances and Future Challenges, Apr 18-20 2001*. 2001. San Francisco, CA: Materials Research Society.
21. Aksu, S. and F.M. Doyle, *Electrochemistry of copper in aqueous ethylenediamine solutions.* Journal of the Electrochemical Society, 2002. **149**(7): p. B340-B347.
22. Preston, F.W., *The Theory and Design of Plate Glass Polishing Machines.* Journal of the Society of Glass Technology, 1927. **11**: p. 214.
23. Kaufman, F.B., D.B. Thompson, R.E. Broadie, M.A. Jaso, W.L. Guthrie, D.J. Pearson, and M.B. Small, *Chemical-Mechanical Polishing for Fabricating Patterned W Metal Features as Chip Interconnects.* Journal of the Electrochemical Society, 1991. **138**(11): p. 3460-3465.
24. Paul, E., *A model of chemical mechanical polishing.* Journal of the Electrochemical Society, 2001. **148**(6): p. G355-G358.
25. Paul, E., *Application of a CMP model to tungsten CMP.* Journal of the Electrochemical Society, 2001. **148**(6): p. G359-G363.
26. Paul, E., *A model of chemical mechanical polishing - II. Polishing pressure and speed.* Journal of the Electrochemical Society, 2002. **149**(5): p. G305-G308.
27. Paul, E. and R. Vacassy, *A model of CMP - III. Inhibitors.* Journal of the Electrochemical Society, 2003. **150**(12): p. G739-G743.
28. Paul, E., F. Kaufman, V. Brusic, J. Zhang, F. Sun, and R. Vacassy, *A model of copper CMP.* Journal of the Electrochemical Society, 2005. **152**(4): p. G322-G328.
29. Ives, D.J.G. and A.E. Rawson, *Copper Corrosion .3. Electrochemical Theory of General Corrosion.* Journal of the Electrochemical Society, 1962. **109**(6): p. 458-462.
30. Speckmann, H.-D., M.M. Lohrengel, J.W. Schultze, and H.-H. Strehblow, *Growth and reduction of duplex oxide films on copper.* Berichte der Bunsengesellschaft fuer Physikalische Chemie, 1985. **89**(4): p. 392-402.
31. Shoesmith, D.W., T.E. Rummery, D. Owen, and W. Lee, *Anodic Oxidation of Copper in Alkaline Solutions 1. Nucleation and Growth of Cupric Hydroxide Films.* Journal of the Electrochemical Society, 1976. **123**(6): p. 790-799.
32. Atkins, P.W., *Physical Chemistry*. 6th ed. 1998: Oxford University Press.

33. Du, T., Y. Luo, and V. Desai, *The combinatorial effect of complexing agent and inhibitor on chemical-mechanical planarization of copper.* Microelectronic Engineering, 2004. **71**(1): p. 90-97.
34. Aksu, S., L. Wang, and F.M. Doyle, *Effect of hydrogen peroxide on oxidation of copper in CMP slurries containing glycine.* Journal of the Electrochemical Society, 2003. **150**(11): p. G718-G723.
35. Du, T., D. Tamboli, V. Desai, and S. Seal, *Mechanism of copper removal during CMP in acidic H2O2 slurry.* Journal of the Electrochemical Society, 2004. **151**(4): p. G230-G235.
36. Du, T., A. Vijayakumar, and V. Desai, *Effect of hydrogen peroxide on oxidation of copper in CMP slurries containing glycine and Cu ions.* Electrochimica Acta, 2004. **49**(25): p. 4505-4512.
37. Magnussen, O.M. and R.J. Behm, *Atomic-scale processes in Cu corrosion and corrosion inhibition.* Mrs Bulletin, 1999. **24**(7): p. 16-23.
38. Walsh, J.F., H.S. Dhariwal, A. Gutierrez-Sosa, P. Finetti, C.A. Muryn, N.B. Brookes, R.J. Oldman, and G. Thornton, *Probing molecular orientation in corrosion inhibition via a NEXAFS study of benzotriazole and related molecules on Cu(100).* Surface Science, 1998. **415**(3): p. 423-432.

Table 3.1 Rate constants and coefficients for kinetic rate equations of glycine, H_2O_2, and BTA with Cu^0.

Reactions	Kinetic rate constants		Coefficients
Glycine deprotonation	$k_{GDP,f}$ / min^{-1}	1.06	n_{g0} (0.35)
(3.13)	$k_{GDP,b}$ / min^{-1}	0.75	(Fraction coefficient)
H_2O_2 oxidation (3.19)	$k_{0,H}$ / l mol^{-1} min^{-1}	1.80×10^3	
BTA adsorption (3.22)	k_a / l^{nb} min^{-1} mol^{-nb}	1.46×10^2	n_{b0} (0.68)
	k_d / min^{-1}	0.083	

Table 3.2 Values of etching rate constants in etching rate model.

Primary	R_{pH2} / nm min^{-1}	3.55×10^{-1}
	$R_{0,G}$ / nm $l^{n_{g0}}$ min^{-1} $mol^{-n_{g0}}$	-4.99×10^{-1}
	$R_{0,H}$ / nm l min^{-1} mol^{-1}	2.13×10^{2}
Secondary	$R_{0,GH}$ / nm $l^{(n_{g0}+1)}$ min^{-1} $mol^{-(n_{g0}+1)}$	2.77×10^{1}
	$R_{0,GB}$ / nm $l^{(n_{g0}+1)}$ min^{-1} $mol^{-(n_{g0}+1)}$	-5.25×10^{2}
	$R_{0,HG}$ / nm l^{2} min^{-1} mol^{-2}	2.92×10^{2}
	$R_{0,HB}$ / nm l^{2} min^{-1} mol^{-2}	6.26×10^{6}
Tertiary	$R_{0,GHB}$ / nm $l^{(n_{g0}+2)}$ min^{-1} $mol^{-(n_{g0}+2)}$	7.14×10^{6}
	$R_{0,GBH}$ / nm $l^{(n_{g0}+2)}$ min^{-1} $mol^{-(n_{g0}+2)}$	7.14×10^{6}
	$R_{0,HGB}$ / nm l^{3} min^{-1} mol^{-3}	3.18×10^{7}
	$R_{0,HGH}$ / nm l^{4} min^{-1} mol^{-4}	8.40×10^{7}
	$R_{0,HBG}$ / nm l^{3} min^{-1} mol^{-3}	3.18×10^{7}
	$R_{0,HBH}$ / nm l^{4} min^{-1} mol^{-4}	8.51×10^{7}

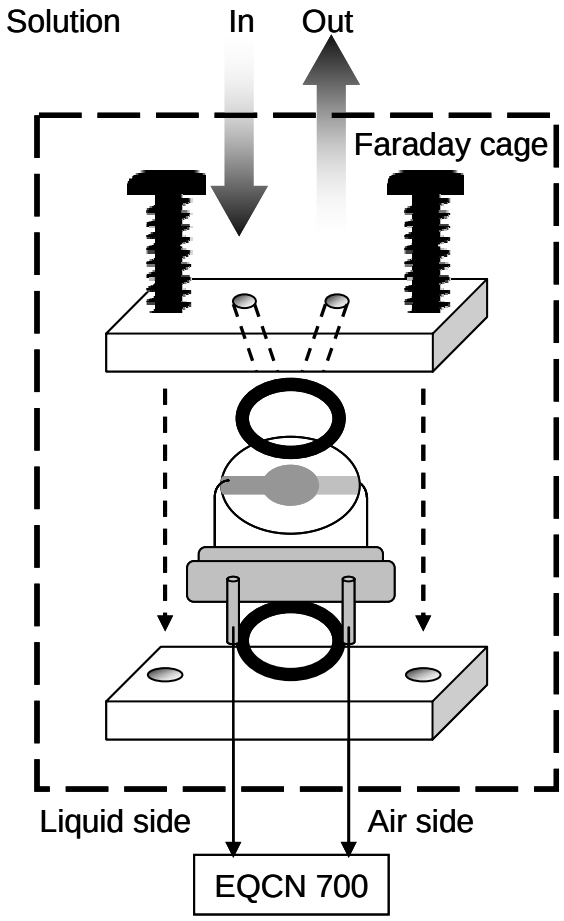

Figure 3.1 Instrumental setup of QCM with flow cell system. Solution flow rate is controlled by syringe pump.

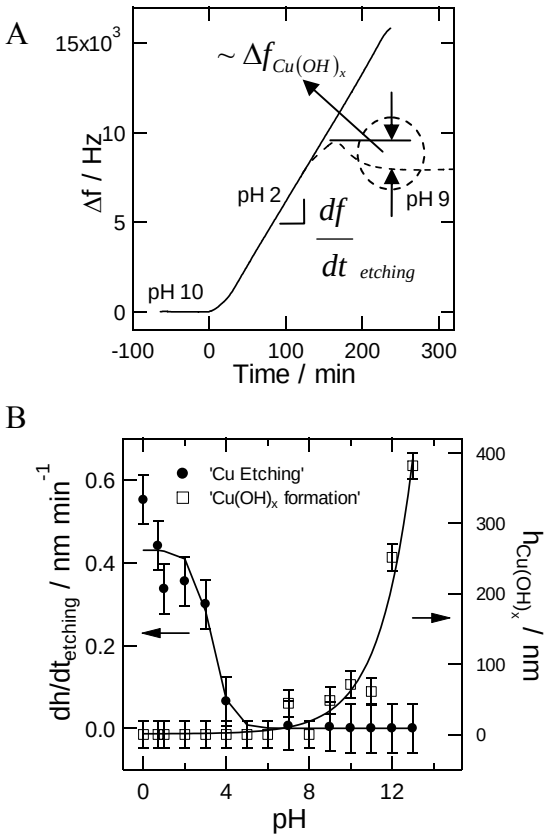

Figure 3.2 Measurement of etching rate and approximate copper oxide thickness. Real time observation of frequency change provides the etching rate by slope (A). Etching rate depends on pH where it is high at low pH and reduced significantly at high pH (B). Solid line for etching rate in (B) represents the dissolution rate model (3.6).

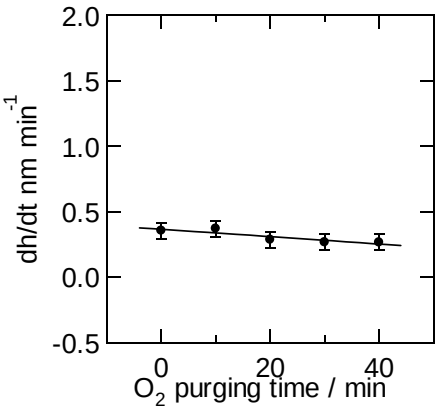

Figure 3.3 Etching rate change at pH 2 according to purging time of oxygen. The first data point with O_2 purging time of zero represents the etching rate after N_2 purging. Etching rate does not increase along with O_2 purging time increase.

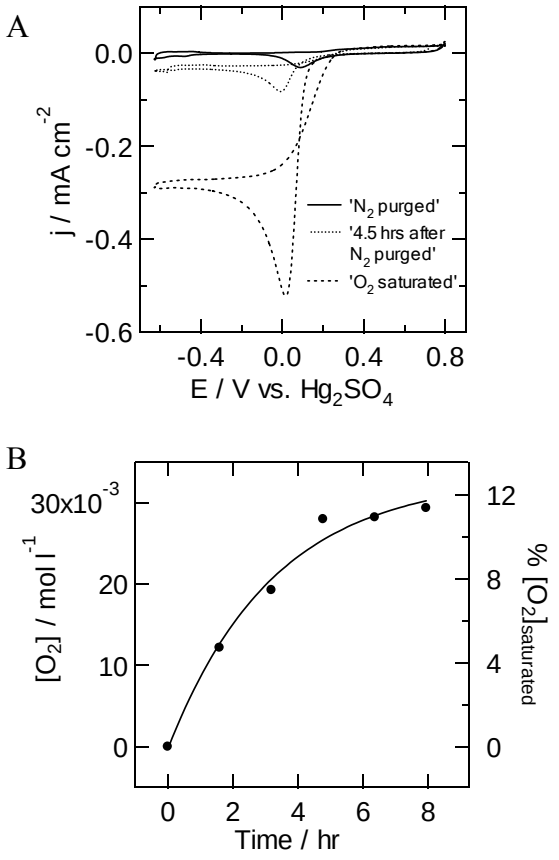

Figure 3.4 Cyclic voltammetric (CV) curve of Pt in 1 mol l^{-1} H_2SO_4 solution with Hg_2SO_4 as a reference electrode and Pt/Ir as a counter electrode after purging with N_2 for 30 min (A) and concentration change of O_2 in solution according to time after purging with N2 (B). CV was run with a scan rate of 5 mV / sec between -0.63 and 0.8 V vs. Hg_2SO_4.

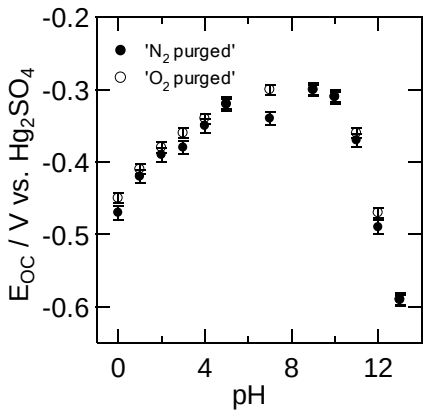

Figure 3.5 Open circuit potential (OCP, E_{OC}) dependence on pH after 4 hours since purging with N_2 for 30 min or O_2 for 10 min. For each pH, purging with N_2 or O_2 does not change OCP.

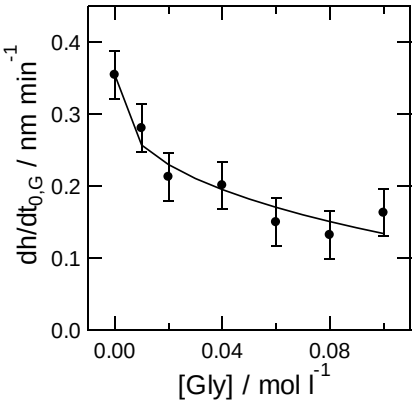

Figure 3.6 Etching rate change according to glycine concentration. Etching rate is decreased by glycine complexation with oxide ions by which metallic copper is oxidized and dissolved. Solid line represents additive model.

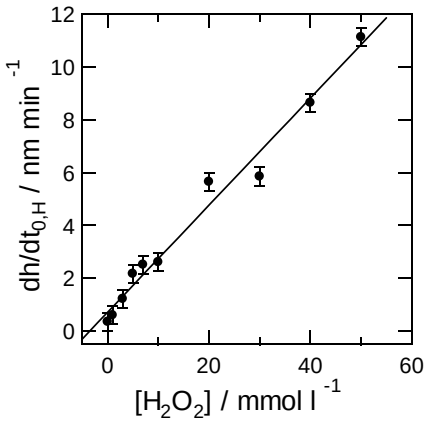

Figure 3.7 Etching rate change according to H_2O_2 concentration. Etching rate increases with H_2O_2 concentration. Etching rate is increased along with increased oxidation rate by H_2O_2.

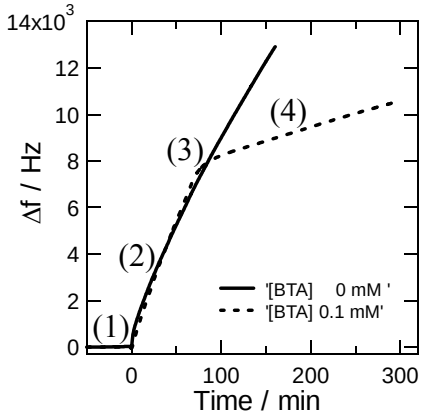

Figure 3.8 Real time measurement of etching rate in presence of BTA. Initially, high pH solution stabilizes surface (1) followed by low pH solution to remove copper oxide (2). BTA solution is injected (3) to passivate surface. Passivated surface reaches a stable state without indication of multilayer adsorption (4).

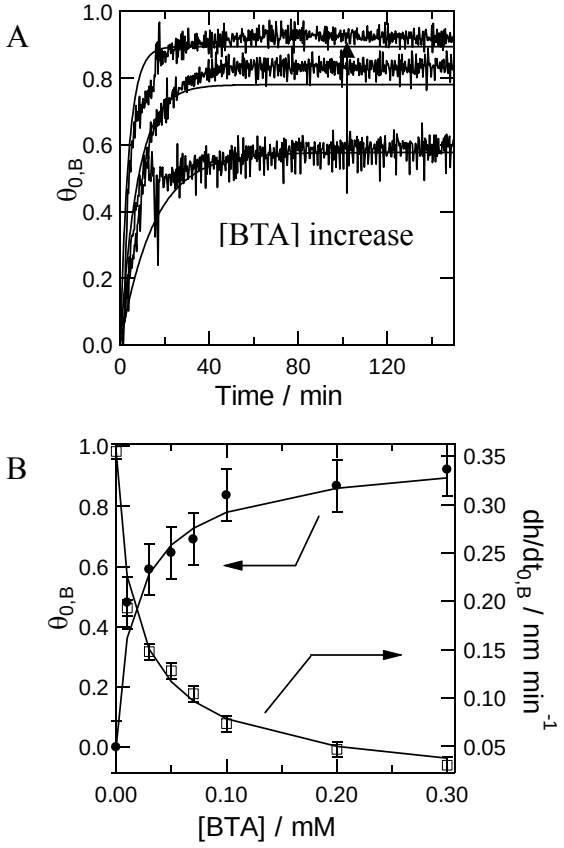

Figure 3.9 BTA adsorption dynamics (A) and isotherm (B) on metallic copper. Langmuir-type adsorption model fits both plots.

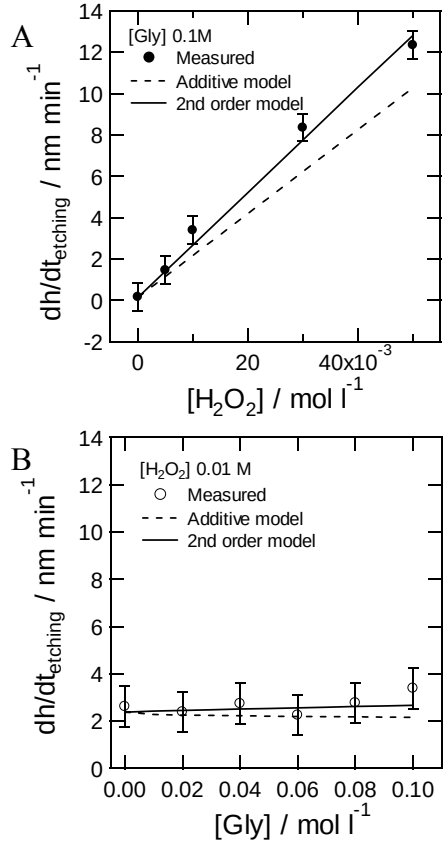

Figure 3.10 Etching rate change according to H_2O_2 (A) and glycine (B) concentration in presence of the other. Dashed lines show additive model and solid lines represent updated model with secondary constants.

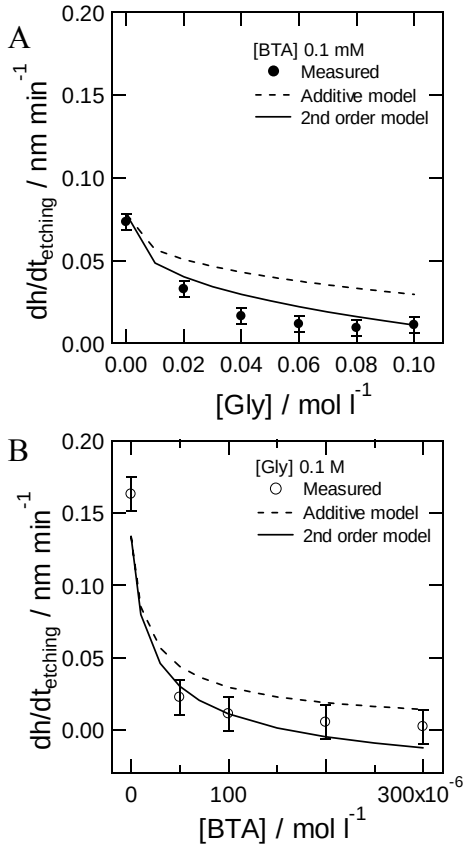

Figure 3.11 Etching rate change according to glycine (A) and BTA (B) concentration in presence of the other. Secondary interaction between glycine and BTA is not significant. Dashed lines show additive model and solid lines represent updated model with secondary constants.

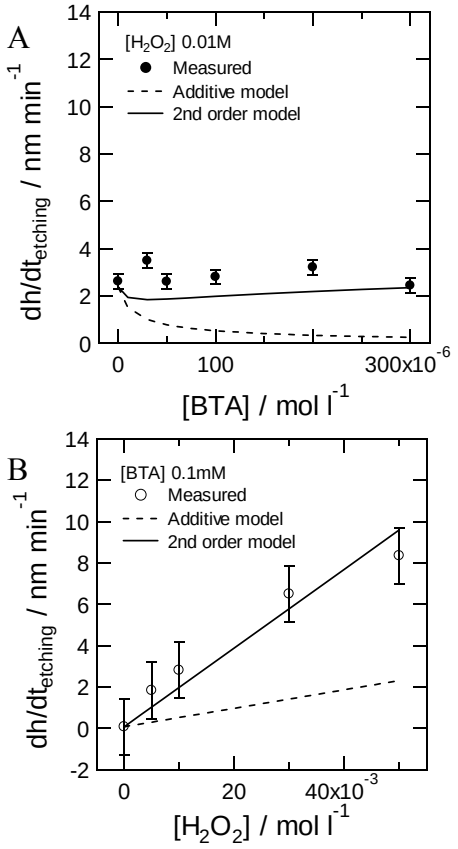

Figure 3.12 Etching rate change according to BTA (A) and H_2O_2 (B) concentration in presence of the other. Secondary interaction between glycine and BTA is noticeable compared to the other secondary interactions. Inhibition of BTA is not observable in presence of H_2O_2. Dashed lines show additive model and solid lines represent updated model with secondary constants.

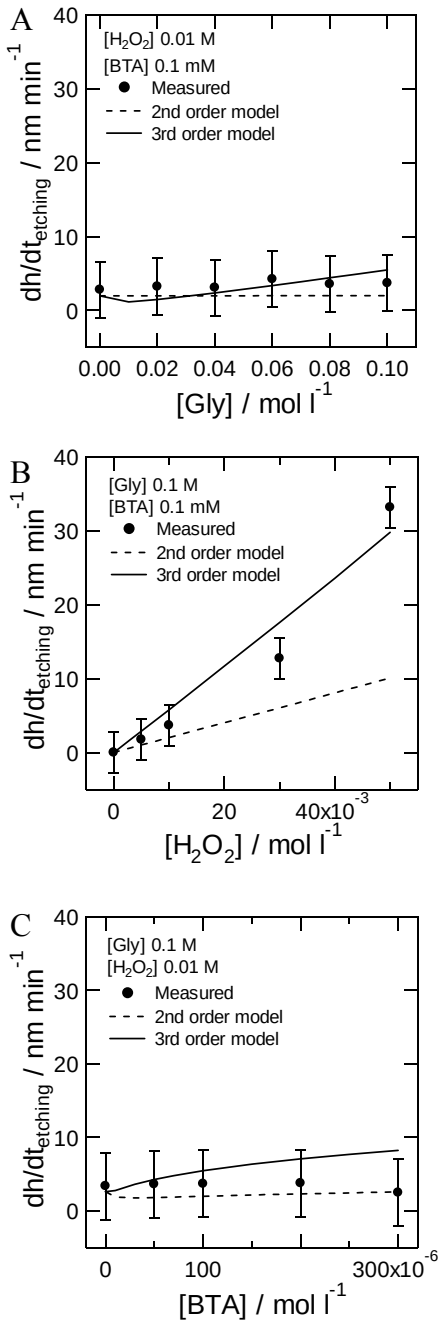

Figure 3.13 Etching rate change according to glycine (A), H_2O_2 (B), and BTA (C) concentration in presence of the other components. H_2O_2 is the most significant factor for controlling chemical etching rate compared with glycine and BTA.

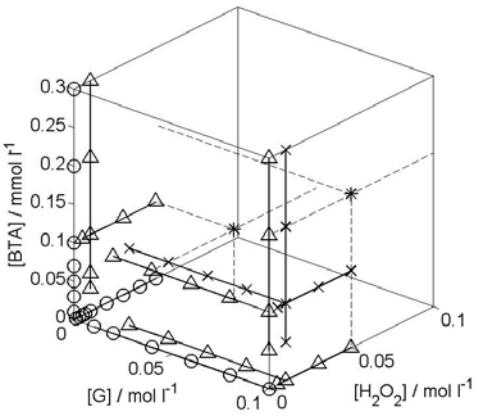

Figure 3.14 Design of experiment (DOE) for single, bi and tri component solutions at pH 2. (○: single component; △:bi component; × : tri component; *: predicted component)

Chapter 4. Chemical Etching Rate Study of Copper in Contact with Glycine, H_2O_2, and Benzotriazole at High pH

4.1 Abstract

The etching rate of copper is studied in aqueous media with benzotriazole (BTA), glycine, and H_2O_2 at high pH where oxidized copper passivates the surface. Real time mass change of copper is detected by in-situ quartz crystal microgravimetry (QCM). Chemical reactions and their kinetics are analyzed by considering interactions between copper surface and the chemicals. Chemical impact on copper etching at high pH is different from that at low pH. Glycine is an indispensable component to trigger copper dissolution at high pH while it decreases corrosion rate at pH 2. At high pH, glycine combines with the passivated layer to form soluble complexes and the dissolution rate is dependent on either complexation or oxidation process, whichever goes slower. BTA decreases etching process by inhibitive adsorption and H_2O_2 increases dissolution rate by accelerating copper oxidation as they do at pH 2 for metallic copper. An additive etching rate model is constructed for copper etching at high pH in a similar way at low pH. Etching rate contribution by each chemical agent is additively combined to form the model. Primary etching rate terms for pH and H_2O_2 are zeros since etching does not occur without glycine. Secondary interactions between the chemicals at high pH are similar to those at low pH. Glycine has little interaction with the other components. On the other hand, BTA inhibition is significantly reduced by the presence of H_2O_2. The additive model is compensated for the deviations caused by interactions among chemical agents. The updated etching rate formula explains major chemical contributions based on fundamental kinetic mechanisms.

4.2 Introduction

In the previous chapter, we studied fundamental kinetic mechanisms of chemical etching reaction of copper at pH 2 with and without chemical agents and constructed a coherent etching rate model based on the kinetic study. Outermost surface of copper in aqueous solutions is divided into metallic copper or oxidized copper that passivate the surface depending on pH. In chapter 3, we segregated metallic copper from the others by controlling pH at 2 and studied its chemical reactions with glycine, BTA, and H_2O_2. Additive model was constructed by combining chemical reaction rates and compensated for secondary interactions among chemical components.

In this chapter, the solution pH is changed to where different copper surface is at equilibrium. The passivated copper surface at high pH has different chemical composition and hence reaction mechanisms with the chemical components are changed from those at pH 2. It is then required to study the chemical reactions and kinetic mechanisms at high pH in order to construct a coherent etching rate formula for this condition. Fundamental kinetic study will be carried out for glycine, H_2O_2, and BTA in a combination of experimental data and kinetic modeling at high pH. Additive model will be developed by combining individual kinetic expression in the same way for low pH dissolution rate model. Secondary interactions among chemical components will be considered and the additive model will be updated for compensation. Copper etching rate is measured by in-situ quartz crystal microgravimetry (QCM).

4.3 Experimental

Materials and Reagents: Chemical agents were used as received. Hydrogen peroxide was received from Fisher scientific (Pittsburgh, PA). Benzotriazole (BTA) and glycine were received from Alfa Aesar (Ward Hill, MA). 18 MΩ Deionized water (Nanopure, Barnstead, Dubuque, IA) was used to prepare all aqueous solutions. pH was adjusted by using sodium

hydroxide (Mallinckrodt Bolder inc., Hazelwood, MO) or sulfuric acid (Fisher Scientific). Prepared solutions were deaerated by N_2 for 30 min before use.

Sample preparation: Samples were prepared by depositing copper on gold coated quartz crystal. Gold coated AT-cut 10 MHz quartz crystal was received from Elchema corp. (Potsdam, New York). The quartz crystal disk had 14 mm diameter and 0.166 mm thickness. Gold was coated at center on both sides of the quartz crystal with 5 mm diameter and connected to steel contact. 99.9 % pure copper wire was received from Goodfellow (Devon, PA) and deposited on gold by 100 nm in vacuum evaporator (DV-502A, Denton Vacuum, Moorestown, NJ) for QCM measurement.

Quartz crystal microgravimetry (QCM): Copper etching rate was measured in real time by quartz crystal microgravimetry (QCM) with a flow cell system (Figure 3.1). Fast response (1-5 ms) and high sensitivity (< 1 ng) were the main reason to select QCM as a real time measurement tool. Steel contact that was linked to gold film on each side of quartz crystal was connected to frequency measurement system (EQCN-700, Elchema, Potsdam, NY). Prepared solutions were injected through a tube by a syringe pump (Genie Kent, Kent Scientific Corp., Torrington, CT) at a constant flow rate (1 ml / hr). The flow rate of solution was adjusted to minimize the frequency fluctuation while keeping the solutions to flow continuously. Copper deposited side was faced with introducing solutions and the other side was exposed to the air. The flow cell system and quartz crystal were placed inside a Faraday cage (Elchema, Potsdam, NY) to minimize noise.

4.4 Results and discussion

Copper corrosion rate depends on pH and the etching rate equation for pH is presented in chapter 3. At moderately high pH, hydroxide ions combine and passivate the copper surface. At a pH below 4, outermost metallic copper is oxidized and removed by dissolved oxygen and proton in the solutions, respectively. When glycine is added into the

solution, it deprives a fraction of oxide ions that oxidize copper and hence reduces the dissolution rate. On the other hand, hydrogen peroxide accelerates copper oxidation and as a result increases dissolution rate. When BTA is added, copper dissolution rate is significantly decreased by inhibitive adsorption that follows Langmuir adsorption isotherm. These reactions occur between the chemical components and metallic copper that is the main outermost surface at low pH. When pH is elevated, outermost surface is covered by passivation layer that has different chemical activity from metallic copper. Therefore, chemical reaction mechanisms are changed with also different reaction rates.

For the investigation of chemical reactions at high pH, 5×10^{-5} mol l^{-1} of NaOH solution that has pH 9.7 is prepared. When this alkaline solution is introduced to the flow cell with QCM (Figure 3.1), the resonant frequency from the quartz crystal is shortly stabilized. In order to observe the reactions with chemical agents, 0.01 mmol l^{-1} BTA, 0.002 mol l^{-1} glycine, and 0.1 mol l^{-1} H_2O_2 solutions at the same pH are prepared and introduced following the empty alkaline solutions. Figure 4.1 shows real time measurement with QCM by introducing these three different chemical components to the quartz crystal. Chemical injection leads mass change of copper that appears as frequency change. Depending on their chemical interactions with copper surface, frequency is increased or decreased. First, H_2O_2 injection decreases frequency or increases weight, which indicates further oxidation by H_2O_2 in addition to the passivation reaction by hydroxide ions. Copper surface in alkaline solution is known to have duplex structure of porous layer on top of compact oxide films[1, 2]. H_2O_2 can penetrate through the porous layer and oxidize the bottom layer further by strong oxidation capability. Second, BTA introduction does not cause noticeable change on copper surface. It could mean either that BTA does not adsorb on copper oxide surface at high pH or that weight addition is too small to be observed. To make it clear, BTA adsorption must be observed while etching, which will be carried out later in this chapter. Third, glycine increases frequency or decreases weight, which indicates that only glycine initiates etching

process for the passivation layer in alkaline solutions. Since BTA and H_2O_2 do not make copper dissolve, glycine is a critical component for copper dissolution at high pH. The frequency increase with the introduction of glycine is straight, that is, the dissolution rate is constant and the slope represents dissolution rate.

Figure 4.2A shows etching rate change depending on glycine concentration. Aksu and Doyle showed that higher concentration of glycine at pH between 9 and 12 accompanied higher etching rate[3] but systematic study has not been made. Figure 4.2A is divided into two regions. At low concentration region, etching rate is enhanced along with concentration increase. On the contrary at high concentration region, etching rate is not increased regardless of concentration change. Etching mechanism in the presence of glycine must be elucidated in order to explain this phenomenon. Overall dissolution process of copper oxide in the presence of glycine can be considered as a combination of aqueous oxidation of metallic copper to form passivation layer by hydroxide ions

$$Cu_{(s)} + OH^-_{(aq)} \underset{\longleftarrow}{\longrightarrow} Cu(OH)_{(s)} + e^- \qquad r_{pv} = k_{pvf} n_0 \left[OH^-\right] - k_{pvb} n_1 \tag{4.1}$$

the complexation of glycine with the passivation layer

$$Cu(OH)_{(s)} + n_g G^-_{(aq)} \underset{\longleftarrow}{\longrightarrow} Cu^+ - G^-_{n_g(s)} + OH^-_{(aq)} \qquad r_G = k_{Gf} n_1 \left[G^-\right]^{n_g} - k_{Gb} n_{1G} \tag{4.2}$$

followed by fast dissolution of the copper-glycine complexes.

$$Cu^+ - G^-_{n_g(s)} \longrightarrow Cu^+ - G^-_{n_g(aq)} \qquad r_D \tag{4.3}$$

r_{pv}, r_G, and r_D is the reaction rate of passivation, glycine complexation, and dissolution respectively, k_{pvf} and k_{pvb} are the forward and backward rate constants of passivation, and k_{Gf} and k_{Gb} are the forward and backward rate constants of the glycine complexation respectively. n_0, n_1, and n_{1G} are surface area density for metallic copper, cuprous hydroxide, and glycine combined cuprous hydroxide respectively.

Low concentration region in Figure 4.2A is controlled by glycine concentration, which indicates that glycine complexation (4.2) is rate determining step (RDS) for this region and dissolution of the complex species (4.3) is fast. Since the dissolution step is fast, complexation and dissolution can be assumed to be one irreversible process, namely, glycine dissolution (GD).

$$Cu(OH)_{(s)} + n_g G^-_{(aq)} \longrightarrow Cu^+ - G^-_{n_g(aq)} + OH^-_{(aq)} \qquad r_{GD} = k_{Gf} n_1 \left[G^-\right]^{n_g} \tag{4.4}$$

At high concentration region, etching rate is not increasing with concentration enhancement. It is because the passivation layer on the surface is removed and oxidation of metallic copper (4.1) delimits overall dissolution rate. Hydroxide ion is the only source to passivate metallic copper, which makes dissolution rate constant at a pH.

An additive etching rate model can be constructed for glycine containing solutions based on the kinetic model in the same way at pH 2. That is, overall etching rate is additive combination of dissolution rate by pH and glycine, where dissolution rate by solution at pH 9.7 ($R_{pH9.7}$) is nearly zero without other chemicals.

$$\frac{dh}{dt} = \left(R_{pH\,9.7} + R_{ox,G}\left[G^-\right]^{n_g}\right)\theta_1 \tag{4.5}$$

θ_1 is relative surface site density of cuprous hydroxide. $R_{ox,G}$ is etching rate constant for glycine and $R_{pH9.7}$ is nearly zero. [G^-] is the concentration of anion and the relative amount is determined by equation (3.8). $R_{ox,G}$ is proportional to the kinetic constant k_{Gf} by

$$R_{ox,G} = k_{Gf}\,\frac{N_A V_{cell}}{n_T A_{Cu}} \tag{4.6}$$

where N_A is Avogadro's number, V_{cell} is the volume of the cell (0.15 ml), n_T is the total surface site density (10^{15} atoms cm^{-2}), and A_{Cu} is the surface area of copper on quartz crystal. Since H_2O_2 does not contribute to the overall etching rate without glycine, additive model can be updated without affecting the overall dissolution rate. Hence the additive model is transformed to

$$\frac{dh}{dt} = \left(R_{pH\,9.7} + R_{ox,G} \left\{ \frac{10^{pH-9.778}}{1+10^{pH-9.778}} [G] \right\}^{n_g} + R_{ox,H} [H_2O_2] \right) \theta_1 \tag{4.7}$$

where $R_{ox,H}$ is etching rate constant for dissolution by H_2O_2 and equal to zero. The relative surface site density needs to be calculated by considering the passivation and glycine dissolution reactions. The passivation reaction increases θ_1 and decreases θ_0 while glycine dissolution decreases θ_1 and increases θ_0. At equilibrium, the change of θ_0 and θ_1 is equal to zero.

$$\frac{d\theta_0}{dt} = \left(-r_{pv} + r_{GD} \right) / n_T = 0 \tag{4.8-1}$$

$$\frac{d\theta_1}{dt} = \left(r_{pv} - r_{GD} \right) / n_T = 0 \tag{4.8-2}$$

Using equation (4.8) along with the fact that summation of θ_1 and θ_0 is unity ($\theta_0 + \theta_1 = 1$), the expressions for θ_0 and θ_1 can be obtained. Solid line in Figure 4.2A represents calculated value by updated etching rate formula (4.7) along with surface density changes (4.8). Trial-and-error method is carried out to find best values of kinetic and etching rate constants, which appear in Table 4.1 and 4.2. Calculation shows how surface densities are changed (Fig ure 4.2B). At low concentration region, copper oxide initially covers most of the surface and glycine dissolution is an RDS. It is overturned as the concentration is increased, where metallic copper occupies majority of the surface and its oxidation becomes an RDS for overall dissolution.

Etching rate change by BTA and H_2O_2 couldn't be measured alone since dissolution does not occur without glycine. Hence, H_2O_2 and BTA are incorporated into glycine solution to observe etching rate change and study kinetics. Figure 4.3A shows etching rate change when H_2O_2 is put together with glycine. Etching rate is observed for glycine with 0.01 mol l^{-1} H_2O_2 (Figure 4.3A) or for H_2O_2 with 0.006 mol l^{-1} glycine (Figure 4.3B). Etching rate is increased significantly by the addition of H_2O_2. The increased etching rate of glycine in the presence of H_2O_2 is due to the increased oxidation rate. H_2O_2 transforms metallic copper to

cupric oxide by equation (3.19). Cupric oxide is also available for glycine complexation and dissolution in the same way of equation (4.4). Etching rate by H_2O_2 concentration enhancement increases slightly with glycine concentration of 0.006 mol l^{-1} where glycine complexation delimits dissolution rate.

In order to explain the dissolution rate when glycine and H_2O_2 are present, the additive model (4.7) is used and updated. The update of additive model is carried out by calculating relative surface site densities and by including secondary etching rate constants. In order to calculate relative surface site densities, oxidized copper surfaces – cuprous hydroxide and cupric oxide – are integrated since both are dissolved by glycine complexation and dissolution. Hence they are lumped to oxidized copper sites (n_{ox}). At high pH, the removal of oxidized copper exposes metallic copper underneath. Therefore, relative surface site densities of metallic copper (θ_0) and copper oxide (θ_{ox}) need to be calculated based on the involved reactions. The passivation by hydroxide ions and oxidation by H_2O_2 increases copper oxide and decreases metallic copper while the dissolution by glycine increases metallic copper and decreases copper oxide.

$$\frac{d\theta_0}{dt} = \left(-r_{pv} + r_{GD} - r_{0,H}\right)/n_T = 0 \tag{4.9-1}$$

$$\frac{d\theta_{ox}}{dt} = \left(r_{pv} - r_{GD} + r_{0,H}\right)/n_T = 0 \tag{4.9-2}$$

Considering that the summation of θ_0 and θ_{ox} is unity ($\theta_0 + \theta_{ox} = 1$), the dependence of relative surface site densities on the concentration of glycine and H_2O_2 is obtained. The secondary etching rate constants are incorporated in the same way at low pH.

$$R_{ox,G} \rightarrow R_{ox,G} + R_{ox,GH}\left[H_2O_2\right] + R_{ox,GB}\left[BTA\right] \tag{4.10-1}$$

$$R_{ox,H} \rightarrow R_{ox,H} + R_{ox,HG}\left[Gly\right] + R_{ox,HB}\left[BTA\right] \tag{4.10-2}$$

$R_{ox,GH}$, $R_{ox,GB}$, $R_{ox,HG}$, and $R_{ox,HB}$ are secondary etching rate constants that account for the impact of H_2O_2 on glycine, BTA on glycine, glycine on H_2O_2, and BTA on H_2O_2, respectively

(BTA terms are included for glycine-BTA system). The secondary etching rate constants account for the change of etching rate dependence on a chemical component by the presence of another. For instance, effective chemical form of a component can be increased or decreased by the presence of another component. More detailed study about the secondary interactions will improve the model. The updated equation with surface site densities and secondary rate constants matches the measured dissolution rate in Figure 4.3A and B.

The measurement of etching rate by introduction of BTA along with glycine appears in Figure 4.4. BTA is an inhibitor that reduces etching rate of copper. We have seen that even slight amounts of BTA have a significant inhibiting impact on metallic copper etching at low pH. Figure 4.4 shows that BTA has a profound impact at high pH too. Etching rate is less than 5% in Figure 4.4A compared with Figure 4.2A by the incorporation of 1×10^{-5} mol l^{-1} BTA. Figure 4.4B also shows dramatic decrease of etching rate by increasing BTA concentration. Etching rate decrease is due to the inhibitive adsorption of BTA onto the copper surface. BTA introduction incorporates two additional reactions of inhibitive adsorption. Adsorption on metallic copper (3.22) and adsorption on copper oxide (cupric oxide is used as a representative of copper oxide that include cuprous hydroxide and cupric oxide).

$$CuO_{(s)} + n_{box} BTA \underset{\longleftarrow}{\longrightarrow} CuO - BTA_{n_{box}} \qquad r_{ox,B} = k_{oxBf} n_{ox} [BTA]^{n_{box}} - k_{oxBb} n_{oxB} \tag{4.11}$$

k_{2Bf} and k_{2Bb} represent forward and backward reaction rate constants for BTA adsorption on copper oxide, respectively. n_{oxB} is the surface density of BTA-adsorbed copper oxide and not available for complexation and etching.

The additive model is updated by calculating surface site densities and incorporating secondary etching rate constants. Secondary etching rate constants for BTA are included in equation (4.10). Relative surface densities are calculated based on the involved chemical reactions, including passivation by hydroxide ions (4.1), dissolution by glycine (4.4), and the

two inhibitive adsorptions, (3.22) and (4.11). There are also four possible surface sites, metallic copper (n_0), copper oxide (n_{ox}), BTA adsorbed metallic copper (n_{0B}) and copper oxide (n_{oxB}) and they depend on the four possible reactions. At equilibrium, their changes are zeros.

$$\frac{d\theta_0}{dt} = \left(-r_{pv} + r_{GD} - r_{0,B}\right)/n_T = 0 \tag{4.12-1}$$

$$\frac{d\theta_{ox}}{dt} = \left(r_{pv} - r_{GD} - r_{ox,B}\right)/n_T = 0 \tag{4.12-2}$$

$$\frac{d\theta_{0B}}{dt} = r_{0,B}/n_T = 0 \tag{4.12-3}$$

$$\frac{d\theta_{oxB}}{dt} = r_{ox,B}/n_T = 0 \tag{4.12-4}$$

The summation of the four sites is equal to unity.

$$1 = \theta_0 + \theta_{ox} + \theta_{0B} + \theta_{oxB} \tag{4.13}$$

Solving equation (4.12) with equation (4.13) provides the change of relative surface site densities according to BTA and glycine concentration. In this case, both the additive and the updated models explain the dissolution rate dependence on glycine and BTA pretty well, which indicates secondary interactions between glycine and BTA are not noticeable.

When glycine, BTA, and H_2O_2 are put together, all of the previous reactions are involved and etching rate dependence on the chemical elements becomes more complicated. Figure 4.5 shows the etching rate dependence on glycine (A), H_2O_2 (B), and BTA (C) when they are put together. Generally, glycine has the biggest impact on etching rate compared with the other two components. The etching rate model is updated by calculating relative surface site density changes and incorporating tertiary etching rate constants. All the previous reactions have to be considered for surface site density calculation, which include passivation by hydroxide ions (4.1), glycine dissolution (4.4), H_2O_2 oxidation (3.19), and BTA adsorption ((3.22) and (4.11)). Four different surface sites are present, including metallic copper (θ_0),

copper oxide (θ_2), BTA-covered metallic copper (θ_{0B}), and BTA-covered copper oxide (θ_{oxB}). Summation of these four relative surface site densities is unity as the equation (4.13) and each density change depends on the chemical reactions.

$$\frac{d\theta_0}{dt} = \left(-r_{pv} + r_{GD} - r_{0,H} - r_{0,B}\right)/n_T = 0 \tag{4.14-1}$$

$$\frac{d\theta_{ox}}{dt} = \left(r_{pv} - r_{GD} + r_{0,H} - r_{ox,B}\right)/n_T = 0 \tag{4.14-2}$$

$$\frac{d\theta_{0B}}{dt} = r_{0,B}/n_T = 0 \tag{4.14-3}$$

$$\frac{d\theta_{oxB}}{dt} = r_{ox,B}/n_T = 0 \tag{4.14-4}$$

Solving three in equations (4.14) with equation (4.13) reveals the dependence of surface site densities on chemical components. When three components are put together, secondary etching rate constants in equation (4.10) are expanded to account for possible tertiary interactions.

$$R_{ox,GH} \rightarrow R_{ox,GH} + R_{ox,GHB}[BTA] \tag{4.15-1}$$

$$R_{ox,GB} \rightarrow R_{ox,GB} + R_{ox,GBH}[H_2O_2] \tag{4.15-2}$$

$$R_{ox,HG} \rightarrow R_{ox,HG} + R_{ox,HGB}[BTA] + R_{ox,HGH}[H_2O_2][BTA] \tag{4.15-3}$$

$$R_{ox,HB} \rightarrow R_{ox,HB} + R_{ox,HBG}[Gly] + R_{ox,HBH}[H_2O_2][Gly] \tag{4.15-4}$$

$R_{ox,GHB}$, $R_{ox,GBH}$, $R_{ox,HGB}$, $R_{ox,HGH}$, $R_{ox,HBG}$, and $R_{ox,HBH}$ are tertiary etching rate constants for the impact of BTA on $R_{ox,GH}$, H_2O_2 on $R_{ox,GB}$, BTA on $R_{ox,HG}$, H_2O_2 and BTA on $R_{ox,HG}$, glycine on $R_{ox,HB}$, and H_2O_2 and glycine on $R_{ox,HB}$, respectively. Solid and dashed lines in Fig ure 4.5 A, B, and C show calculation with and without tertiary constants, respectively. The updated model with tertiary constants matches the experimental measurement nicely and shows large gap with the second order model.

The final etching rate model for glycine, H_2O_2, and BTA at pH 9.7 is given by

$$\frac{dh}{dt} = \left(R_{pH9.7} + R'_{ox,G} \left\{ \frac{10^{pH-9.778}}{1+10^{pH-9.778}} [G] \right\}^{n_g} + R'_{ox,H} [H_2O_2] \right) \theta_{ox} \tag{4.16}$$

where the extended primary etching rate constants $R'_{ox,G}$ and $R'_{ox,H}$ are given by

$$R'_{ox,G} = R_{ox,G} + R'_{ox,GH} [H_2O_2] + R'_{ox,GB} [BTA] \tag{4.17-1}$$

$$R'_{ox,H} = R_{ox,H} + R'_{ox,HG} [Gly] + R'_{ox,HB} [BTA] \tag{4.17-2}$$

and the extended secondary etching rate constants $R'_{ox,GH}$, $R'_{ox,GB}$, $R'_{ox,HG}$, and $R'_{ox,HB}$ are represented by

$$R'_{ox,GH} = R_{ox,GH} + R_{ox,GHB} [BTA] \tag{4.18-1}$$

$$R'_{ox,GB} = R_{ox,GB} + R_{ox,GBH} [H_2O_2] \tag{4.18-2}$$

$$R'_{ox,HG} = R_{ox,HG} + R_{ox,HGB} [BTA] + R_{ox,HGH} [H_2O_2][BTA] \tag{4.18-3}$$

$$R'_{ox,HB} = R_{ox,HB} + R_{ox,HBG} [Gly] + R_{ox,HBH} [H_2O_2][Gly] \tag{4.18-4}$$

The final etching rate model (4.16) is constructed based on the additive model and works well for multi component. The gap between experimental measurements and additive model was compensated by incorporating secondary and tertiary constants. The models can be integrated once the dependence of etching rate constants and relative surface site densities on pH is revealed, which would require complete measurements on all pH.

Figure 4.6 shows a semi-quantitative quad plot that shows etching rate change in a glance when the three components are put together. Ternary diagram at the bottom represents relative contents of three components that appear in Figure 4.5, only after transformed to relative contents. The concentration of each component is rescaled from 0 to 1 by dividing with maximum concentration of each component (BTA 10^{-4} mol l^{-1}, H_2O_2 0.1 mol l^{-1}, and glycine 0.1 mol l^{-1}) and its relative content is enumerated against the others. For example, the concentrations of glycine, H_2O_2, and BTA are 0.02 mol l^{-1}, 0.01 mol l^{-1}, and 10^{-5} mol l^{-1}, their

rescaled values are 0.2, 0.1, and 0.1 by dividing with the maximum concentrations. Then, the relative contents are 0.5, 0.25, and 0.25. Figure 4.6 shows experimental parameter space and measured values. The bigger the bar is, the higher is the etching rate, where the biggest change depends on glycine.

In order to examine if the etching rate model predicts reasonable values for randomly chosen conditions, we selected a couple of conditions and measured etching rate. Figure 4.7 shows the design of experiment (DOE) for all experimental conditions where ○, △, and × represent single, bi, and tri component conditions. Asterisk (*) represents arbitrarily selected conditions for prediction with the etching rate model. When the concentrations of BTA, glycine, and H_2O_2 are 1×10^{-5} mol l^{-1}, 0.04 mol l^{-1}, and 0.05 mol l^{-1}, respectively, the measured etching rate is 12.2 nm min^{-1} and predicted value is 29.4 nm min^{-1}. When the concentrations of BTA, glycine, and H_2O_2 are 1×10^{-4} mol l^{-1}, 0.06 mol l^{-1}, and 0.05 mol l^{-1}, respectively, the measured etching rate is 18.8 nm min^{-1} and predicted value is 21.5 nm min^{-1}. The prediction is not as accurate as at pH 2. The increased error is probably due to the presence of complex surface sites. At high pH, copper surface consists of more than single compositions that add complexity and increase the possibility of errors. Theoretical calculation of etching rate requires calculation of surface site density for different copper surface and a small error may exaggerate overall etching rate prediction error.

Quantitative results for copper etching in the presence of glycine and H_2O_2 and for BTA adsorption are compared with literature. Table 4.3 presents etching rate change measured by Aksu et al.[4] and Du et al.[5] Aksu et al. measured copper etching rate according to H_2O_2 concentration in presence of 0.01 mol l^{-1} glycine by weight loss experiment at pH 4 and 9. Weight loss experiment is to measure weight difference of samples after a specific time in solutions. Table 4.3 is shown in Figure 4.8. The range of H_2O_2 concentration measured by Aksu et al. is from 0 to 5 wt % that corresponds to 1.47 mol l^{-1}. They observed the etching rate increased up to 0.2 wt % that corresponds to 0.06 mol l^{-1} but

do not further study this region to obtain kinetic information. Overall, etching rate measured by Aksu et al. is bigger. One of the reasons is that they put higher concentration of glycine along with H_2O_2. Above pH 4, the role of glycine is critical without which copper surface is mainly passivated. The etching rate changes at pH 4 and pH 4 show a similar trend where pH 4 presents slightly higher etching rate. According to our observation, about 84 % of copper surface is passivated at pH 4 and hence it seems natural to show similar trend in etching rate change at pH 4 with that at pH 9. Du et al. observed etching rate change in the absence of glycine at pH 4 and obtained similar trend with what Aksu et al. observed. Etching rate showed the highest at 1 vol % of H_2O_2 (0.315 mol l^{-1}) concentration followed by significant decrease with further concentration increase. Aksu et al. and Du et al. observed increased etching rate at low concentration of H_2O_2 but did not study that region for kinetic information. Our etching rate measurement corresponds to the low concentration region below 0.1 mol l^{-1} H_2O_2 and provides kinetic information about chemical reactions not only for H_2O_2 oxidation but also for glycine complexation.

Quantitative information about BTA adsorption on copper is observed by Bastidas[6] and Lewis[7]. They carried out weight loss experiment and calculated BTA coverage by the ratio of etching rate with and without BTA (Table 4.4). Figure 4.9 shows the comparison of BTA coverage (θ) as a function of BTA concentration from table 4.4. Bastidas adjusted solution pH using HCl and observed that BTA coverage is higher at higher pH at the same BTA concentration. Both Bastidas and Lewis assumed BTA adsorption as a monolayer formation and explained using Frumkin isothersm. Frumkin isotherm is an extension of Langmuir model to account for the interaction between adsorbed molecules. They fit the experimental data by least square method and obtain kinetic and thermodynamic information. Table 4.5 presents binding constant (k) and adsorption energy (ΔG°_{ads}) at 298 K obtained by Bastidas and Lewis. They show similar adsorption energy around -21 kJ mol^{-1} but binding constant is somewhat different. The binding constant we measured for BTA adsorption on

metallic copper is 1759, which is between the values obtained by Bastidas and Lewis. They obtained the isotherm in BTA concentration from 1×10^{-5} mol l^{-1} to 0.1 mol l^{-1}. However, considering the solubility of BTA in aqueous solution is less than 5×10^{-3} mol l^{-1}, it does not make sense to draw isotherm beyond the solubility limit.

4.5 Conclusions

In this chapter, chemical reactions of glycine, benzotriazole (BTA), and hydrogen peroxide with copper at pH 9.7 were studied and a coherent etching rate model was constructed in the same principle with that at pH 2. The chemical property of copper surface in aqueous solutions depended on pH. At high pH, hydroxide ions from the solution passivated the surface to have different chemical property from the metallic copper at low pH. The passivated copper surface started to dissolve by the addition of glycine into solution. Glycine was combined with copper oxide to form soluble species. On the other hand, BTA and H_2O_2 did not initiate etching and hence glycine was an indispensable chemical to start chemical etching at high pH. However, impact of BTA inhibition and H_2O_2 oxidation were also apparent they were put together with glycine. Etching rate was significantly reduced or increased by inhibition or faster oxidation, respectively. Impacts of secondary interactions between components were similar to those at low pH. BTA inhibition was significantly diminished by the presence of H_2O_2 as it was at low pH.

Additive etching rate formula was built based on elemental chemical reaction mechanisms and tested for multi component systems. The gap between measured data for multi component systems and the additive model was compensated by incorporating secondary and tertiary etching constants. The final model was constructed in the same way with that at pH 2. Once the dependence of etching rate constants on pH is clarified, the two models could be integrated. This study has significance in that overall etching rate model is obtained based on fundamental reaction mechanisms of major chemical components for

copper etching. The model additively combines kinetic expression of each chemical reaction. Therefore further inclusion of chemical and even mechanical components can be incorporated without significant modification of the model once the reaction mechanisms are elucidated.

Nomenclature

dh/dt : dissolution rate

N_A : Avogadro's number

V_{cell} : volume of the flow cell

A_{Cu} : surface area of piezoelectrically active copper surface

r_{pv} : reaction rate of passivation

r_G : reaction rate of glycine complexation

r_D : reaction rate of dissolution for glycine complexed with passivated copper surface

r_{GD} : reaction rate of dissolution by glycine complexation

$r_{0,B}$: reaction rate of BTA adsorption on metallic copper

$r_{0,H}$: reaction rate of copper oxidation by H_2O_2

$r_{ox,B}$: reaction rate of BTA adsorption on oxidized copper

k_{pvf} : kinetic rate constant for forward reaction of passivation

k_{pvb} : kinetic rate constant for backward reaction of passivation

k_{Gf} : kinetic rate constant for forward reaction of glycine complexation with passivated copper surface

k_{Gb} : kinetic rate constant for backward reaction of glycine complexation with passivated copper surface

k_{oxBf} : kinetic rate constant for forward reaction of BTA adsorption on oxidized copper

k_{oxBb} : kinetic rate constant for backward reaction of BTA adsorption on oxidized copper

n_0 : surface site density of metallic copper

n_1 : surface site density of passivated copper

n_{1G} : surface site density of glycine complexed passivated copper

n_T : total surface site density (=10^{15} atoms cm^{-2})

n_{ox} : surface site density of oxidized copper

n_{oxB} : surface site density of BTA-covered oxidized copper

n_g : stoichiometric constant for dissolution by glycine complexation

n_{box} : stoichiometric constant for BTA adsorption on oxidized copper

θ_1 : relative surface site density of cuprous hydroxide

θ_{ox} : relative surface site density of oxidized copper

θ_0 : relative surface site density of metallic copper

θ_{0B} : relative surface site density of BTA-covered metallic copper

θ_{oxB} : relative surface site density of BTA-covered oxidized copper

$R_{pH\,9.7}$: dissolution rate of copper at pH 9.7

$R_{ox,G}$: etching rate constant for glycine

$R_{ox,H}$: etching rate constant for H_2O_2

$R_{ox,GH}$: secondary etching rate constant for glycine with H_2O_2

$R_{ox,GB}$: secondary etching rate constant for glycine with BTA

$R_{ox,HG}$: secondary etching rate constant for $H_2O_2$with glycine

$R_{ox,HB}$: secondary etching rate constant for $H_2O_2$with BTA

$R_{ox,GHB}$: tertiary etching rate constant for glycine with H_2O_2 and BTA

$R_{ox,GBH}$: tertiary etching rate constant for glycine with H_2O_2 and BTA

$R_{ox,HGB}$: tertiary etching rate constant for H_2O_2 with glycine and BTA

$R_{ox,HGH}$: tertiary etching rate constant for H_2O_2 with glycine and BTA

$R_{ox,HBG}$: tertiary etching rate constant for H_2O_2 with BTA and glycine

$R_{ox,HBH}$: tertiary etching rate constant for H_2O_2 with glycine and BTA

4.6 References

1. Ives, D.J.G. and A.E. Rawson, *Copper Corrosion .3. Electrochemical Theory of General Corrosion.* Journal of the Electrochemical Society, 1962. **109**(6): p. 458-462.
2. Speckmann, H.-D., M.M. Lohrengel, J.W. Schultze, and H.-H. Strehblow, *Growth and reduction of duplex oxide films on copper.* Berichte der Bunsengesellschaft fuer Physikalische Chemie, 1985. **89**(4): p. 392-402.
3. Aksu, S. and F.M. Doyle, *Electrochemistry of copper in aqueous glycine solutions.* Journal of the Electrochemical Society, 2001. **148**(1): p. B51-B57.
4. Aksu, S., L. Wang, and F.M. Doyle, *Effect of hydrogen peroxide on oxidation of copper in CMP slurries containing glycine.* Journal of the Electrochemical Society, 2003. **150**(11): p. G718-G723.
5. Du, T., D. Tamboli, V. Desai, and S. Seal, *Mechanism of copper removal during CMP in acidic H2O2 slurry.* Journal of the Electrochemical Society, 2004. **151**(4): p. G230-G235.
6. Bastidas, D.M., *Adsorption of benzotriazole on copper surfaces in a hydrochloric acid solution.* Surface and Interface Analysis, 2006. **38**(7): p. 1146-1152.
7. Lewis, G., *Adsorption isotherm for the copper-benzotriazole system.* British Corrosion Journal, 1981. **16**(3): p. 169-171.

Table 4.1 Kinetic rate constants, coefficients, and the change of surface sites according to the involved reactions.

Reactions	Kinetic rate constants		Coefficients	Surface site changes
Passivation by hydroxide ions (4.1)	k_{pvf} / l mol^{-1} min^{-1}	0.0192		$\theta_0 \rightarrow \theta_{ox}$
	k_{pvb} / min^{-1}	3.7×10^{-13}		$\theta_{ox} \rightarrow \theta_0$
Glycine dissolution (4.4)	k_{2Gf} / cm^2 l^{ng-1} min^{-1} atoms^{-1} mol^{ng-1}	1.0×10^{10}	n_g (6.71)	$\theta_{ox} \rightarrow \theta_0$
	k_{2Gb} / min-^{1}	-		
H_2O_2 oxidation (3.19)	k_{0H} / l mol^{-1} min^{-1}	1.80×10^{3}		$\theta_0 \rightarrow \theta_{ox}$
BTA Inhibition (4.11)	k_{oxBf} / l$^{n_{b2}}$ min^{-1}mol$^{-n_{b2}}$	1.07×10^{6}	n_{b2} (1.33)	$\theta_{ox} \rightarrow \theta_{oxB}$
	k_{oxBb} / min^{-1}	3.82×10^{-7}		$\theta_{oxB} \rightarrow \theta_{ox}$

Table 4.2 Primary, secondary, and tertiary etching rate constants for etching rate formula.

Primary	$R_{pH9.7}$ / nm min^{-1}	0
	$R_{ox,G}$ / nm l^{n_g} min^{-1} mol^{-n_g}	4.60×10^{15}
	$R_{ox,H}$ / nm l min^{-1} mol^{-1}	0
Secondary	$R_{ox,GH}$ / nm $l^{(n_g+1)}$ min^{-1} $mol^{-(n_g+1)}$	1
	$R_{ox,GB}$ / nm $l^{(n_g+1)}$ min^{-1} $mol^{-(n_g+1)}$	0
	$R_{ox,HG}$ / nm l^2 min^{-1} mol^{-2}	1.96×10^{4}
	$R_{ox,HB}$ / nm l^2 min^{-1} mol^{-2}	-5.20×10^{12}
Tertiary	$R_{ox,GHB}$ / nm $l^{(n_g+2)}$ min^{-1} $mol^{-(n_g+2)}$	1
	$R_{ox,GBH}$ / nm $l^{(n_g+2)}$ min^{-1} $mol^{-(n_g+2)}$	5.00×10^{10}
	$R_{ox,HGB}$ / nm l^3 min^{-1} mol^{-3}	4.93×10^{14}
	$R_{ox,HGH}$ / nm l^4 min^{-1} mol^{-4}	1
	$R_{ox,HBG}$ / nm l^3 min^{-1} mol^{-3}	4.93×10^{14}
	$R_{ox,HBH}$ / nm l^4 min^{-1} mol^{-4}	1.32×10^{15}

Table 4.3 Etching rate (dh/dt) measured at pH 2 and 10 with or without glycine and comparison with Aksu et al.[4] and Du et al.[5]

Choi				Aksu et al.				Du et al.	
pH 2		pH 10		pH 4		pH 9		pH4	
[Gly]		[Gly]		[Gly]		[Gly]		[Gly]	
0 mol l^{-1}		0.006 mol l^{-1}		0.01 mol l^{-1}		0.01 mol l^{-1}		0 mol l^{-1}	
$[H_2O_2]$ / mol l^{-1}	dh/dt / nm min^{-1}	$[H_2O_2]$ / mol l^{-1}	dh/dt / nm min^{-1}	$[H_2O_2]$ / mol l^{-1}	dh/dt / nm min^{-1}	$[H_2O_2]$ / mol l^{-1}	dh/dt / nm min^{-1}	$[H_2O_2]$ / mol l^{-1}	dh/dt / nm min^{-1}
0.000	0.355	0.000	0.422	0	0	0	0	0.000	0
0.001	0.598	0.000	0.510	0.03	57	0.04	44	0.315	9
0.003	1.221	0.001	0.625	0.06	70	0.07	40	0.944	4
0.005	2.171	0.001	0.844	0.12	51	0.1	34	1.573	3
0.007	2.511	0.003	1.080	0.18	41	0.19	23	2.202	2
0.01	2.614	0.005	1.039	0.24	26	0.22	15	3.146	2
0.02	5.651	0.007	1.122	0.37	13	0.29	10		
0.03	5.856	0.01	1.012	0.74	7	0.37	8		
0.04	8.649			1.1	4	0.74	4		
0.05	11.125			1.47	2	1.1	3		
						1.47	2		

Table 4.4 Coverage of BTA on copper surface at pH 2 and 10 without or with glycine, respectively and comparison with Bastidas[6] and Lewis[7].

Choi				Bastidas			Lewis	
pH 2		pH 10		[HCl] / mol l^{-1}	0.001	0.01	NH_4Cl 0.2 mol l^{-1}	
		[Gly] 0.006 mol l-1						
[BTA] / mol l^{-1}	θ	[BTA] / mol l^{-1}	θ	[BTA] / mol l^{-1}	θ	θ	[BTA] / mol l^{-1}	θ
0.00000	0.000	0.000000	0.000	0.00001	0.01	0.01	0	
0.00001	0.480	0.000001	0.110	0.00005	0.03	0.02	0.001	0.608
0.00003	0.590	0.000003	0.213	0.0001	0.06	0.03	0.002	0.65
0.00005	0.646	0.000005	0.739	0.0005	0.72	0.15	0.003	0.825
0.00007	0.690	0.000007	0.977	0.001	0.91	0.35	0.004	0.946
0.0001	0.837	0.00001	0.981	0.002	0.97	0.78	0.005	0.963
0.0002	0.868	0.00003	0.990	0.003	0.98	0.86	0.006	0.975
0.0003	0.922	0.00005	0.995	0.004	0.985	0.89	0.007	0.984
		0.00007	0.994	0.005	0.985	0.93	0.01	0.998
		0.0001	0.995	0.01	0.99	0.96	0.02	0.998
				0.05	0.99	0.98	0.03	0.998
				0.1	0.99	0.99		

Table 4.5 Binding constant and adsorption energy at 298 K obtained by Bastidas[6] and Lewis[7].

	[HCl] / mol l^{-1}	k	$\Delta G°_{ads}$ / kJ mol^{-1}
Bastidas	0.001	422	-25
	0.005	122	-22
	0.01	272	-24
	0.05	501	-25
	0.1	60	-20
	0.5	201	-23
Lewis		6188	-21.63
Choi		1759	

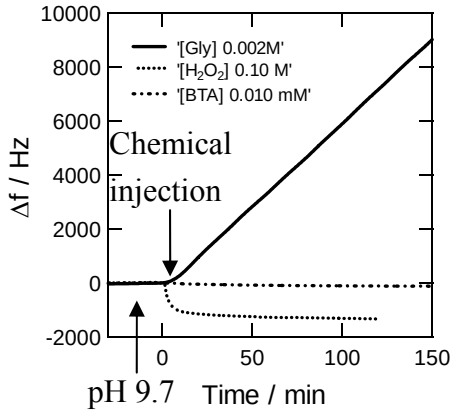

Figure 4.1 Measurement of QCM frequency change for copper in contact with slurry chemicals at high pH. High pH solution passivates copper surface and the injection of slurry chemicals make changes. While BTA injection does not make a big change, H_2O_2 adds more weight by further oxidation and glycine starts to dissolve the surface by combining with copper oxide to form a soluble complex. Glycine is therefore a critical factor for chemical dissolution at high pH.

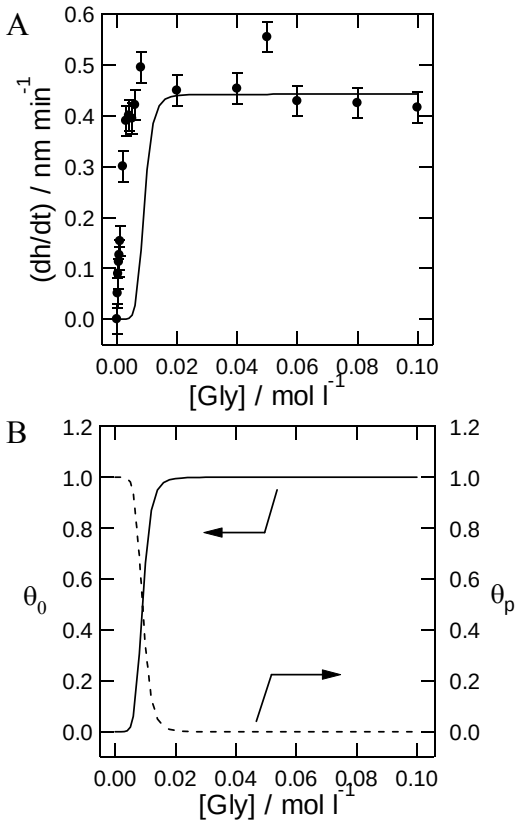

Figure 4.2 Etching rate dependence on glycine concentration at high pH (A) and corresponding relative surface site density changes (B). Etching rate is increased along with glycine concentration at low concentration region while it is constant at high concentration region. This indicates that glycine combination with copper oxide and oxidation of metallic copper are rate determining steps (RDS) at low and high concentration region, respectively. Relative surface site densities calculation demonstrates the RDS by showing that major surface is copper oxide at low concentration region that is overturned by metallic copper at high concentration.

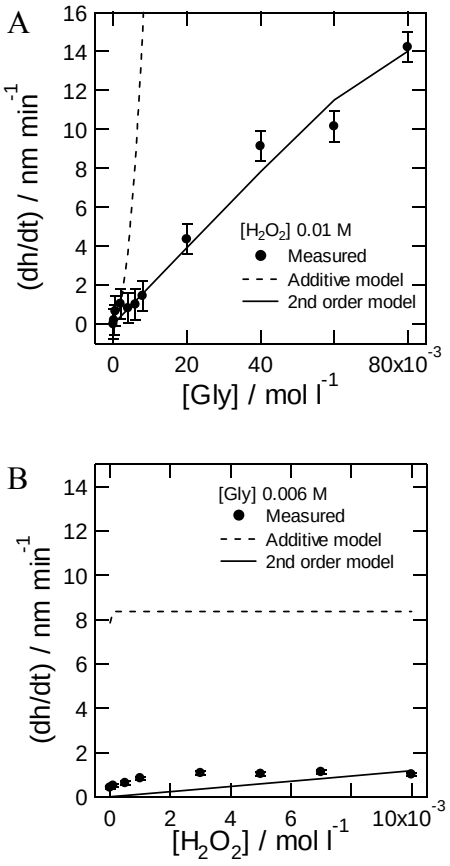

Figure 4.3 Etching rate dependence on glycine (A) and H_2O_2 (B) in presence of the other. In presence of H_2O_2, etching rate according to glycine concentration is greatly enhanced due to increased oxidation rate by H_2O_2. Dashed lines show additive model and solid lines represent updated model with secondary constants.

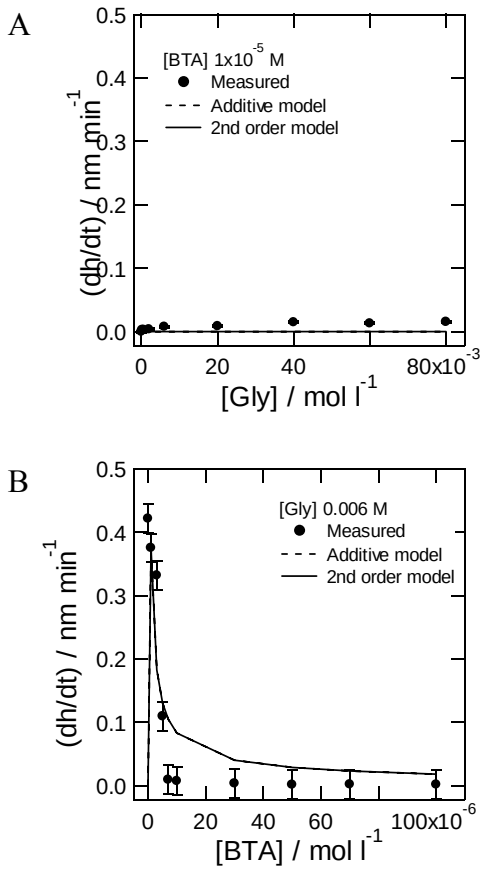

Figure 4.4 Etching rate dependence on glycine (A) and BTA (B) in presence of the other. Etching rate is much reduced by adding BTA due to its inhibitive adsorption on copper oxide. Dashed lines show additive model and solid lines represent updated model with secondary constants, which appear with no change for glycine-BTA systems.

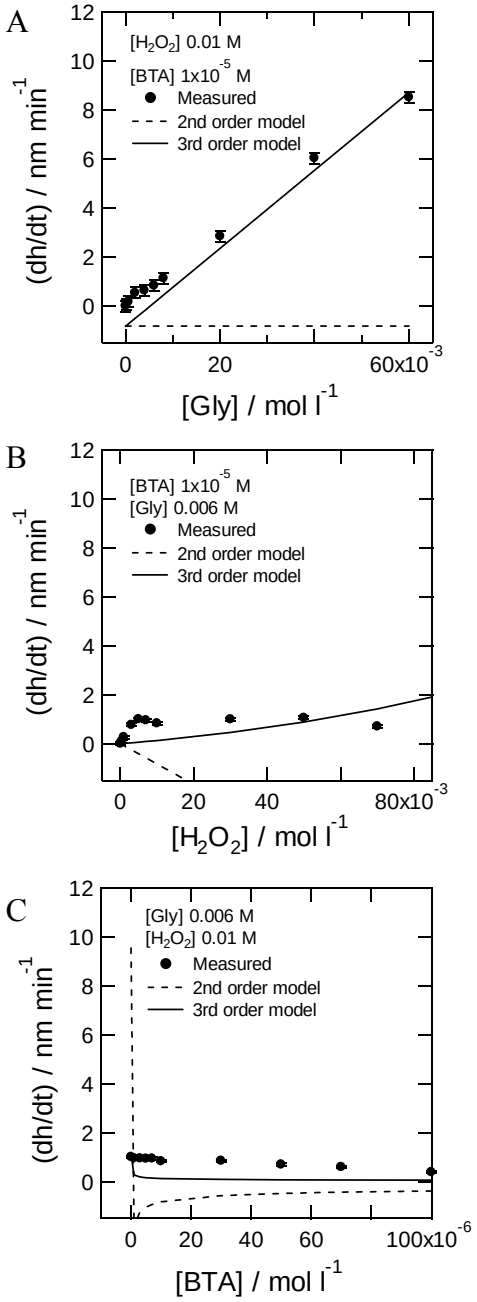

Figure 4.5 Etching rate dependence on glycine (A), H_2O_2 (B), and BTA (C) in presence of the other two components. Glycine has the greatest impact on etching rate compared with the other two. In presence of H_2O_2, BTA inhibition effect is much reduced.

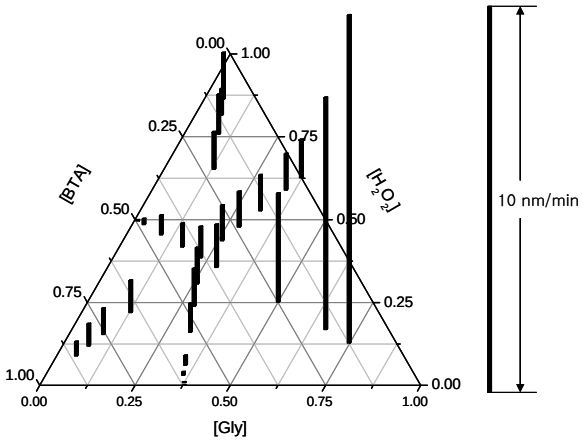

Figure 4.6 Semi-quantitative quad plot that shows etching rate dependence on glycine, H_2O_2, or BTA in presence of the others. Impact of glycine is relatively greater than the others, which means that control of glycine concentration is the most important factor for controlling chemical etching at high pH. The axis represents the relative concentration one component against the others, considering maximum concentration of experiment.

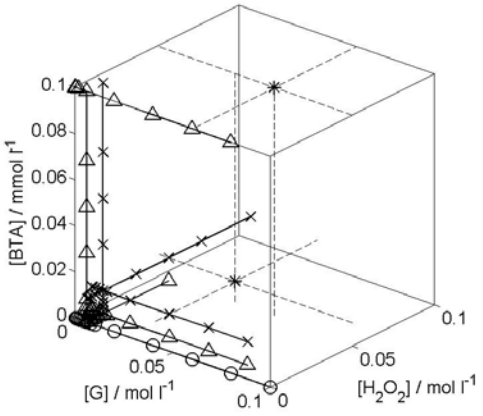

Figure 4.7 Design of experiment (DOE) for single, bi and tri component solutions at pH 10. (○: single component; △:bi component; × : tri component; *: predicted component)

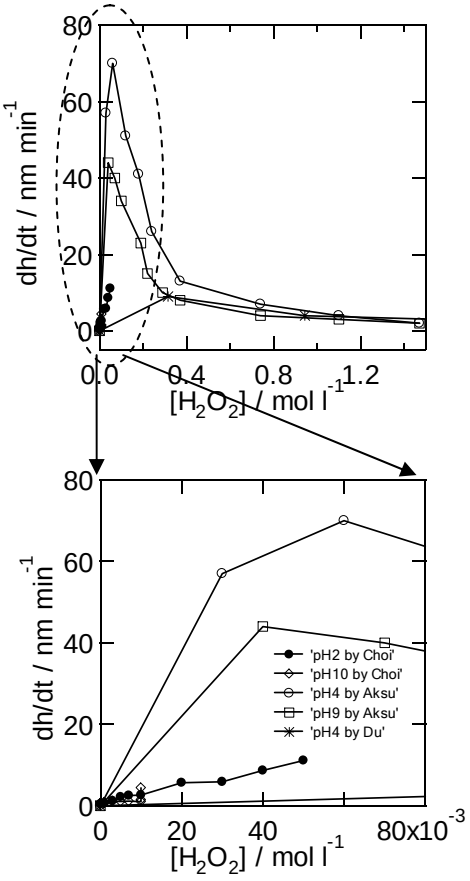

Figure 4.8 Etching rate comparison with literature measured by Aksu et al.[4] and Du et al.[5]

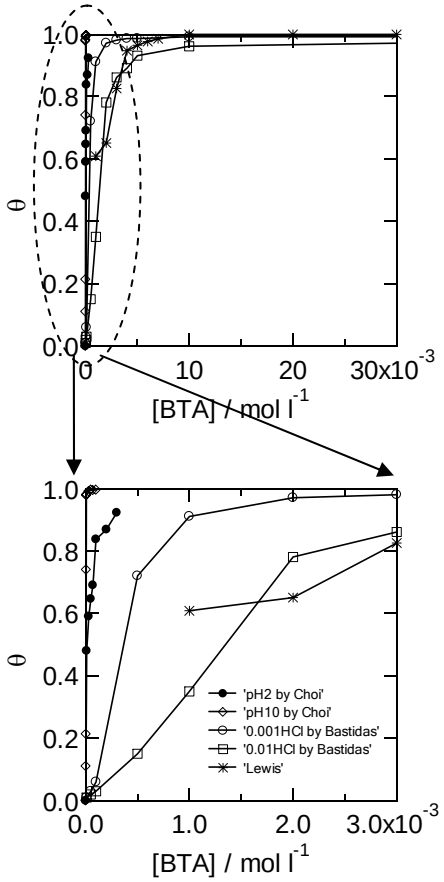

Figure 4.9 Comparison of BTA coverage, θ, with literature obtained by Bastidas[6] and Lews[7].

Chapter 5. Development of High Throughput Surface Plasmon Resonance (SPR) Imaging System

5.1 Abstract

In this chapter, we developed a surface sensitive high throughput characterization technique using surface plasmon resonance (SPR) imaging and applied this technique to study film formation on metal films. We constructed a multi channel SPR imaging (MCSPRI) with a flow cell system to investigate benzotriazole (BTA) film formation on copper surface in aqueous solutions. BTA adsorption was investigated with MCSPRI system but the analysis of measured data presented limitations due to major impact of surface roughness on the observed SPR angle change. However, the concept of high throughput screening with SPR imaging system motivated us to develop multi-electrode SPR imaging (MESPRI) system that was combined with electrochemistry. The combination of SPR and electrochemical techniques was simple but effective and provided significant advantages for simultaneous control and observation of metal-liquid interfaces.

5.2 Introduction

In the previous chapters, we studied copper chemical reactions in aqueous solutions for copper chemical mechanical polishing (Cu-CMP). The complicated chemical reactions required a number of measurements that were essentially a repetition of same experiments with different chemical composition of solutions. Hence, it is useful to systematically study the chemical reactions of copper much faster by utilizing a high throughput detection technique.

Surface plasmon resonance (SPR) is a well-established surface sensitive technique that can observe interfacial phenomena at solid-liquid interfaces. The principle is well understood and its application is wide spread, especially in biosensing area[1-7]. SPR

technique can be utilized in a variety of platforms, i.e. spectroscopy or fixed / spread angle imaging in Kretschmann, Otto, grating coupler, or wave guide configuration[4], which makes SPR instrumentation flexible and applicable in many areas. Using this flexibility, experimental platform of SPR can be extended to have the capability of high throughput screening.

Expanding the capability of SPR technique to have high throughput screening requires adaptation of traditional experimental platforms. For SPR technique, fixed angle SPR imaging (SPRI) with array structure of metal film is typically used for high throughput screening[8-22]. For simultaneous observation of interfacial reactions, a camera monitors collimated light reflected from the prism surface on which the metal array is coated. However, fixed angle SPR imaging observes intensity change at an angle position rather than migrant SPR angle according to interfacial reactions, which may cause unprecedented errors. In addition, array structure is not an efficient design for experiments that involve various solutions with different compositions simultaneously. Hence a different approach is required to make SPR imaging high throughput screening. In this study, we modify SPR imaging system by introducing wedge-shaped light instead of collimated one so that detecting camera can monitor the reflected light in a range of angle and detect SPR angle in-situ real time. A flow cell is fabricated to introduce a number of solutions that have different chemical compositions.

The concept of high throughput system also gives us a motivation to develop another SPR imaging system in combination with electrochemical technique. Advantages of coupling SPR with electrochemistry have been realized for simultaneous control and observation of solid-liquid interfaces[23-25]. Incorporation of SPR with electrochemistry is simple since metal films that are used for generating evanescent wave can be directly used as electrodes. Various electrochemical techniques have been coupled with SPR, which includes scanning electrochemical microscopy (SECM)[18, 26], electrochemical quartz crystal microgravimetry

(EQCM)[27-29], and impedance[30, 31]. We adopt multi-electrode design of metal films for simultaneous control and observation of interfacial changes. Design of multi-electrode is relatively simple and each electrode is easily connected to potentiostat as a working electrode without short circuit.

This chapter presents physical principle and an experimental platform of SPR. Fresnel's relationship that describes the connection of SPR angle changes with physical quantity is derived. In results and discussions, experimental procedure to construct SPR imaging systems using multi-channel flow cell and multi-electrode cell design are presented. The advantages and limitations of SPR imaging systems are discussed.

5.3 Surface plasmon resonance (SPR)

5.3.1 Fundamental physics of SPR and experimental system

Surface plasmon resonance (SPR) utilizes the resonance coupling of two waves in order to characterize the optical change on a metal surface. The resonance coupling occurs when an incident light is introduced onto a metal surface and excites the surface plasmon. It is necessary to understand the description of the surface plasmon waves (SPW) in order to understand its resonance coupling with the incident optical wave in advance.

Collective fluctuations of electrons on a metal boundary are called surface plasma oscillations[32]. These charge fluctuations are accompanied by a mixed transversal and longitudinal electromagnetic field which disappears at $|z| \to \infty$ (Figure 5.1), and has its maximum at the surface, $z = 0$. This polarization wave is described by a complex wave function

$$\vec{A} = \vec{A}_0 e^{i\left(\vec{k}\cdot\vec{r}-\omega t\right)} = \vec{A}_0 e^{i(k_x x \pm k_z z - \omega t)} \tag{5.1}$$

with + for $z > 0$ and – for $z < 0$, where $\vec{A}$ stands for either electric field $\vec{E}$ or magnetic field $\vec{H}$, $\vec{A}_0$ is a constant vector associated with the maximum amplitude of oscillation, $\vec{k}$ is a wave vector ($\vec{k} = k_x\hat{i} + k_y\hat{j} + k_z\hat{k}$, $\hat{i}$, $\hat{j}$, and $\hat{k}$ are unit vectors for *x*, *y*, and *z* direction),

$\vec{r}$ is a position vector ($\vec{r} = x\hat{i} + y\hat{j} + z\hat{k}$), ω is an angular frequency, and t is time. This surface plasmon wave (SPW) is TM (transversal magnetic)-polarized wave, whose magnetic field is perpendicular to the direction of propagation of the SPW and parallel to the plane of interface (y-axis). Hence the wave vector that is perpendicular to the magnetic field does not have y-component (Figure 5.1).

We consider a film of thickness, d, and a frequency-dependent dielectric function $\varepsilon_m(\omega)$ covered on both sides by different media with dielectric constants ε_p and ε_d (Figure 5.2). Starting from the Maxwell's equations[33], which appears next section in this chapter, we can obtain the dispersion relation that connects the angular frequency, ω, with the wave vector, k_{sp}, for the surface plasmon wave

$$k_{sp} = \frac{\omega}{c}\sqrt{\frac{\varepsilon_m \varepsilon_i}{\varepsilon_m + \varepsilon_i}} \tag{5.2}$$

where c stands for the light speed in vacuum and ε_i can be either ε_d or ε_p.

If an incident light is introduced from a dielectric medium of ε_p (> 1) and totally reflected at the metal film surface, an evanescent wave is created and penetrates into the film and the projection of its wave vector on the surface becomes

$$k_x = \frac{\omega}{c}\sqrt{\varepsilon_p}\sin\theta_0 \tag{5.3}$$

where, θ_0 is the angle of the incident light against the surface normal.

The resonance condition of two electromagnetic waves is satisfied when their momentums match each other and the momentum is given by the wave vectors multiplied by the reduced Planck's constant:

$$\vec{P} = \hbar\vec{k} = \frac{h}{2\pi}\vec{k} \tag{5.4}$$

where $\hbar$ is the reduced Planck's constant and h is the Planck's constant ($= 6.626\times10^{-34} J\cdot\sec$). Therefore, we can achieve the resonance condition by equalizing the wave vector of SPW and that of evanescent wave. However, the surface plasmon at the

interface between the metal and the dielectric medium with ε_p – the upper interface in Figure 5.2– cannot be excited since its momentum (line 4 in Figure 5.3) is always larger than that of evanescent wave (line 2 in Figure 5.3). As a result, the resonance coupling occurs at the interface between the metal and the dielectric medium with ε_d – the lower interface in Figure 5.2 – and their resonance condition becomes

$$\frac{\omega}{c}\sqrt{\frac{\varepsilon_m \varepsilon_d}{\varepsilon_m + \varepsilon_d}} = \frac{\omega}{c}\sqrt{\varepsilon_p}\sin\theta_0, \tag{5.5}$$

which is the intersection of line 2 and 3 in Figure 5.3. Direct illumination of the incident light onto an infinite metal cannot excite surface plasmon because the momentum of incident light (line 1 in Figure 5.3) is always smaller than that of surface plasmon at the interface (line 3 in Figure 5.3). Please note that only x-component of the wave vectors exists at the interface. As a result, surface plasmon resonance (SPR) occurs at the interface between the metal and the dielectric medium with ε_d by illuminating an incident light to the thin metal film through a high refractive index medium with ε_p.

Experimentally, SPR can be achieved in various configurations, including Kretschmann configuration[34, 35], Otto configuration[36], grating coupler[3], or optical waveguide[3]. In Kretschmann configuration (Figure 5.4), which is one of the most frequently used configurations, a prism with high refractive index is used to enhance the momentum of incident optical wave and the optical wave is totally reflected at the interface between the prism and the metal layer. In fact, Kretschmann configuration has the exactly same structure in Figure 5.2. When the resonance condition is met, part of the incoming light energy is transferred to the metal phase and it appears as a loss of reflected light intensity. The reflected light intensity or reflectivity is measured as a function of the incident light angle and as the optical property of the interface is changed, the position of SPR angle where the reflectivity becomes minimal in angular space shifts accordingly. The reflectivity curve as a function of the incident angle or SPR curve can be calculated. By fitting the

experimentally obtained SPR curve with the calculation, we can investigate the change that occurs at the interface, i.e., film deposition on the metal layer. This theoretical calculation is called Fresnel's calculation[37] and it can describe the light behavior when the light faces an interface with a different dielectric medium.

5.3.2 Fresnel calculation

The change of SPR angles by interfacial phenomena is connected with physical quantity by Fresnel's relationship. This section presents the derivation of Fresnel's relationship. When an incident light faces an interface with a medium of a different refractive index, it is reflected or refracted (transmitted) and the Fresnel equation describes its behavior. The derivation of Fresnel equation is based on Maxwell's equations for non-magnetic materials. In this section, we will derive the Fresnel equation for 2-phase system and expand it to more complicated multi-phase system.

The Maxwell's equations for non-magnetic material are given by[33]

$$\nabla \cdot \vec{E} = 0 \tag{5.6}$$

$$\nabla \cdot \vec{B} = 0 \tag{5.7}$$

$$\nabla \times \vec{E} = -\frac{\partial \vec{B}}{\partial t} \tag{5.8}$$

$$\nabla \times \vec{B} = \mu\varepsilon \frac{\partial \vec{E}}{\partial t} \tag{5.9}$$

where, $\vec{E}$ is the electric field, $\vec{B}$ is the magnetic induction $\left(\vec{B} = \mu\vec{H}\right)$, and μ and ε are the permeability and the dielectric constant of material through which the light passes, respectively. The electric field $\vec{E}$ and the magnetic induction $\vec{B}$ are described by

$$\vec{E}(\vec{r},t) = \vec{E}_0 e^{i(\vec{k}\cdot\vec{r}-\omega t)} \tag{5.10}$$

$$\vec{B}(\vec{r},t) = \vec{B}_0 e^{i(\vec{k}\cdot\vec{r}-\omega t)} \tag{5.11}$$

where, $\vec{E}_0$ and $\vec{B}_0$ are the constant vectors associated with the maximum amplitude of oscillations. These two wave vectors are related by

$$\vec{B} = \frac{\vec{k} \times \vec{E}}{\omega} = \frac{n}{c} \vec{s} \times \vec{E} \tag{5.12}$$

where $\vec{s}$ is the unit vector in the direction of propagation, as can be derived from the Maxwell equations (5.6), (5.7), (5.8), and (5.9).

The basis for the electromagnetic approach is to establish the boundary conditions that impose restrictions on the relationships between fields on either side of the interface. The boundary condition for the electromagnetic wave at the interface is that there is no discontinuity of the tangential components of the electric field and the magnetic induction at the interface. In equation form, the boundary conditions become for the amplitudes of the fields

$$E_{i,y} + E_{r,y} = E_{t,y} \tag{5.13}$$

$$B_{i,x} + B_{r,x} = B_{t,x} \tag{5.14}$$

$$B_{i,y} + B_{r,y} = B_{t,y} \tag{5.15}$$

$$E_{i,x} + E_{r,x} = E_{t,x} \tag{5.16}$$

where *i*, *r*, and *t* stand for the incident, the reflected, and the transmitted light, respectively. The coordinate system is defined in Figure 5.5.

Equations (5.13) and (5.14) are the boundary conditions for the *s*-polarized light, where the electric field $\vec{E}$ is perpendicular to the plane defined by the direction of propagation and surface normal (Figure 5.5 A). Therefore, $\vec{E}_i$, $\vec{E}_r$, and $\vec{E}_t$ have only *y* components and we can write $E_{i,y} = E_i^s$, $E_{r,y} = E_r^s$, $E_{t,y} = E_t^s$ so that the equation (5.13) can be rewritten as

$$E_i^s + E_r^s = E_t^s \tag{5.17}$$

Using the equation (5.12), the equation (5.14) becomes

$$\left(\vec{k}_i \times \vec{E}_i\right)_x + \left(\vec{k}_r \times \vec{E}_r\right)_x = \left(\vec{k}_t \times \vec{E}_t\right)_x$$

or

$$k_{i,z}E_i^s + k_{r,z}E_r^s = k_{t,z}E_t^s \tag{5.18}$$

since $\vec{k}_i$, $\vec{k}_r$, and $\vec{k}_t$ have only *x* and *z* components and the angular frequency ω does not change. Equation (5.18) can be further simplified by the fact $k_{r,z} = -k_{i,z}$ since

$$k_{i,z} = n_0 \frac{\omega}{c}\cos\theta_i \quad \text{and} \quad k_{r,z} = -n_0 \frac{\omega}{c}\cos\theta_r = -n_0 \frac{\omega}{c}\cos\theta_i$$

so that it becomes

$$E_i^s - E_r^s = \frac{k_{t,z}}{k_{i,z}} E_t^s = \frac{n_1 \cos\theta_t}{n_0 \cos\theta_i} E_t^s \tag{5.19}$$

By combining the equations (5.17) and (5.19), we can obtain the transmission coefficient

$$t_S = \frac{E_t^s}{E_i^s} = \frac{2n_0 \cos\theta_i}{n_0 \cos\theta_i + n_1 \cos\theta_t} \tag{5.20}$$

and the reflection coefficient

$$r_s = \frac{E_r^s}{E_i^s} = \frac{n_0 \cos\theta_i - n_1 \cos\theta_t}{n_0 \cos\theta_i + n_1 \cos\theta_t} \tag{5.21}$$

for the *s*-polarized light.

Equations (5.15) and (5.16) are the boundary conditions for the *p*-polarized light, where the electric field $\vec{E}$ is parallel to the plane defined by the direction of propagation and surface normal (Figure 5.5 B). In this case $\vec{B}$ has only y component and we can write

$$B_{i,y} = B_i^p,\ B_{r,y} = B_r^p,\ B_{t,y} = B_t^p$$

From the equation (5.12), these scalar quantities become

$$B_i^p = \frac{n_0}{c} E_i^p,\quad B_r^p = \frac{n_0}{c} E_r^p,\quad B_t^p = \frac{n_1}{c} E_t^p \tag{5.22}$$

Therefore the equation (5.15) becomes

$$E_i^p + E_r^p = \frac{n_1}{n_0} E_t^p \tag{5.23}$$

From the geometry, we can see that the equation (5.16) becomes

$$\cos\theta_i \left(E_i^p - E_r^p\right) = \cos\theta_t E_t^p$$

or

$$E_i^p - E_r^p = \frac{\cos\theta_t}{\cos\theta_i} E_t^p \tag{5.24}$$

From the equations (5.23) and (5.24), we can find the transmission coefficient

$$t_p = \frac{E_t^p}{E_i^p} = \frac{2n_0 \cos\theta_i}{n_1 \cos\theta_i + n_0 \cos\theta_t} \tag{5.25}$$

and the reflection coefficient

$$r_p = \frac{E_r^p}{E_i^p} = \frac{n_1 \cos\theta_i - n_0 \cos\theta_t}{n_1 \cos\theta_i + n_0 \cos\theta_t} \tag{5.26}$$

for the *p*-polarized light.

The equations (5.20), (5.21), (5.25), and (5.26) are the relations for the Fresnel coefficients. When the refractive index has imaginary part $N = n + ik$, the more general Fresnel coefficients are given by

$$t_S = \frac{2N_0 \cos\theta_i}{N_0 \cos\theta_i + N_1 \cos\theta_t} \tag{5.27}$$

$$r_s = \frac{N_0 \cos\theta_i - N_1 \cos\theta_t}{N_0 \cos\theta_i + N_1 \cos\theta_t} \tag{5.28}$$

$$t_p = \frac{2N_0 \cos\theta_i}{N_1 \cos\theta_i + N_0 \cos\theta_t} \tag{5.29}$$

$$r_p = \frac{N_1 \cos\theta_i - N_0 \cos\theta_t}{N_1 \cos\theta_i + N_0 \cos\theta_t} \tag{5.30}$$

If the direction of propagation is reversed, that is, light comes from a medium 1 to hit the interface, then the Fresnel coefficients can readily be shown to be

$$r_{10} = -r_{01} \tag{5.31}$$

$$t_{10} = (1 - r_{01}^2)/t_{01} \tag{5.32}$$

as can be proved by interchanging N_0 and N_1 in equations (5.27), (5.28), (5.29), and (5.30). Equations (5.31) and (5.32) can be applied to both *p*- and *s*- waves.

The situation becomes more complex when a film is present due to the presence of an additional interface. In addition, the Fresnel coefficients can be obtained for multi-phase

system that has more than 1 film. Hansen[37] derived the equations for multi phase system. The 4-phase system is a typical situation where it forms an additional film on the metal layer with two different dielectric media on both sides of the films. The calculation program is given in appendix. This 4-phase Fresnel calculation can predict the relative reflectivity as a function of incident angle or the SPR curve as the system is optically changed.

In combination with the Fresnel calculation, SPR measurement can measure optical changes such as additional film formation on metal or refractive index change of the film. The major application of SPR is to measure additional film formation on the metal film for thickness measurement. For the Fresnel calculation, we are required to have information about the light wavelength, incident angle, refractive index for prism, metal film, additional layer, and dielectric medium such as solution, and thickness of the metal film and the additional layer. We can vary the additional layer thickness and obtain the SPR angle change according to the thickness variation from the Fresnel's calculation (Figure 5.6). Using the Kretschmann configuration, we can experimentally obtain SPR curve and acquire SPR angle change by scanning a light beam with a given angle range or by introducing a light having a range of angle. Comparison of measured SPR angle change with the Fresnel's calculation yields the thickness information.

The advantages of SPR include that it is non-invasive, label-free, in-situ, highly sensitive, and fast measurement. In the SPR experimental system, the resonance coupling and the additional film formation occurs on the opposite side of the metal film surface from where the incident light is introduced through a prism. Therefore the additional film avoids direct contact with the prism, which makes SPR non-invasive. SPR measurement is not required to label the additional film or molecules for characterization since it utilizes resonance coupling of surface plasmon for detection. SPR is in-situ measurement since it does not require taking a sample off from the experimental setup. In most cases, the additional film layer is formed and observed at the same time without the need to take the

sample off for measurement. SPR is a sensitive technique that can measure thickness change in angstrom range. This sensitivity comes from the short penetration depth of the surface plasmon wave (SPW), where the penetration depth is the distance from the interface where the intensity falls to 1/e of the original value at the interface. The penetration depth of the SPW into the metal phase is tens of nanometers and that into the dielectric medium is a few hundreds of nanometers. A few examples are shown in Table 1. This short penetration depth makes the SPR sensitive enough to measure angstrom level of thickness change depending on the sensing devices, i.e., charge coupled device (CCD) camera or photo detector that detect reflectivity and determine resolution. For instance, if a CCD camera can take a picture with 760 × 480 resolution and acquire the reflectivity in 8 ° range, then the resolution of observed reflectivity curve is 0.01 ° (≈ 8 ° / 760). This is corresponding to the resolution power of 0.7 Å thickness change of organic film with refractive index of 1.5 in SPR system that has 50 nm gold film (layer 2) on BK7 prism (layer 1) and water (layer 4) under the light wavelength of 730 nm. At the same time, the short penetration depth into the dielectric medium limits the maximum thickness of additional film that can be measured. Figure 5.7 shows how the SPR curve shape changes along with the thickness increase of organic film on metal surface. In SPR system with 50 nm gold film (layer 2) on BK7 prism (layer 1), water (layer 4), and 632 nm wavelength incident light, organic film with thickness up to 50 nm can be measured. Above the thickness, the SPR curve loses its SPR angle that can be detected. SPR measurement can be made fast enough for real time measurement with appropriate experimental setup and kinetic information can be readily obtained.

5.4 Experimental

Materials and reagents: Chemical agents were used as received. Cyclohexane, toluene, trichloro ethylene, acetone, and isopropyl alcohol were received from Fisher Scientific (Pittsburgh, PA). 3-mercaptopropyl methoxysilane was received from Aldrich (St.

Louis, MO). 99.99 % Gold was received from Ernest F. Fullam, Inc. (Clifton Park, NY). Piranha solution was prepared by mixing 75% H_2SO_4 with 25% H_2O_2. 18 MΩ Deionized water (Nanopure, Barnstead, Dubuque, IA) was used to prepare all aqueous solutions. pH was adjusted by using sodium hydroxide (Mallinckrodt Bolder inc., Hazelwood, MO) or sulfuric acid (Fisher Scientific). Prepared solutions were deaerated by N_2 for 30 min before use.

Sample preparation for multi-channel SPR imaging (MCSPRI) system: Optical prisms were used as samples for multi-channel SPR imaging (MCSPRI) system. SF-10 equilateral prism was received from Edmund optics inc. (Barrington, NJ). The equilateral prism was cleaned by 2 % Neutrad solution (Decon Laboratories, inc., King of Prussia, PA) followed by sonicating in cyclohexane for 10 min. Successively, the prism was immersed in Piranha solution at 50 °C for 30 min. Then, the prism was rinsed with DI water and dried with N_2 gas. The dried prism was then immersed in 5 mM 3-mercaptopropyl methoxysilane in toluene for 6 hours to coat the prism surface with thiol terminated silane monolayer. Then, the prism was rinsed with toluene and dried with N_2 gas. 99.9 % copper wire (Goodfellow, Devon, PA) was deposited on the SF-10 equilateral prism by vacuum evaporator (DV-502A, Denton Vacuum, Moorestown, NJ). The coating of silane layer on the prism surface improved the adhesion of copper films.

Sample preparation for multi-electrode SPR imaging (MESPRI) system: Glass slides were used as samples for multi-electrode SPR imaging (MESPRI) system. 99.99 % gold wire was received from Goodfellow (Devon, PA) and deposited on glass slides that was cleaned and coated with silane monolayers in the same way to prepare samples for MCSPRI system by vacuum evaporation (Bench Top Turbo III, Denton Vacuum, Moorestown, NJ). A mask was used to form multi-electrode design of gold. The gold coated glass slides were attached to a BK-7 hemi cylindrical lens (Edmund Industrial optics, Barrington, NJ) with index matching fluid (Norland Index Matching Liquid, Norland products inc., Cranbury, NJ).

Multi-channel SPR imaging (MCSPRI) measurement: Optical components and home-made flow channel systems were used to construct a multi-channel SPR imaging (MCSPRI) system. Copper coated SF-10 equilateral prism was equipped with home-made Teflon cell and cured PDMS (poly dimethylsiloxane) gasket (Dow corning corporation, Midland, MI) that formed multi-channel system (Figure 5.8). Prepared solutions were injected through tubes by a multi-syringe pump (Genie Kent, Kent Scientific Corp., Torrington, CT) at a constant flow rate (0.05 ml min^{-1}). SPR images were observed while the solutions were introduced through the flow cell system. Incident light from a tungsten halogen lamp (LS-1 tungsten halogen light source, Ocean optics Inc. Dunedin, FL) coupled with a narrow band-pass wavelength filter that has a central wavelength of 730 nm (Newport corp., Irvine, CA) passed through a biconvex lens and a plano-convex lens (Newport Corp.) for focusing on the surface of SF-10 equilateral prism where copper was coated. Polarity of incident light was controlled by a linear polarizer (Newport Corp.) that was placed between the convex lenses. The emerging reflected light was collimated by another plano-convex lens and monitored by a high resolution CCD camera (kampro02, EHD Imaging GmbH, Damme, Germany) using a variable zoom lens (Zoom7000, Navitar, Rochester, NY). Images were captured with frame-grabber card (Pinnacle Systems, Inc., Mountain View, CA) using commercially available software (Studio 8, Pinnacle Systems, Inc.). Images were recorded using both *s*- and *p*- polarized light at the sample rotation where the minimum SPR intensity was observed. The angle spread of incident light was measured by the pictures taken directly above the equilateral prism. Refracted angle of light inside the prism was calculated by Snell's law. Angle was defined by the angle against the surface normal where the copper was coated.

Multi-electrode SPR imaging (MESPRI) measurement and electrochemistry: The same optical lenses in MCSPRI system and a home-made electrochemical cell were used to construct multi-electrode SPR imaging (MESPRI) system. SF-10 equilateral prism was

replaced by BK-7 hemi cylindrical lens and gold coated glass slide, which were equipped with home-made Teflon cell and viton o-ring (Figure 5.13). Each gold band on the glass slide was connected to a multi potentiostat (Chi 1030, Chi instruments, Austin, TX) as a working electrode. Quasi Ag/AgCl reference electrode (QRE) and Pt/Ir grid were used as a reference and counter electrode, respectively.

Atomic force microscope (AFM) imaging system: Copper surface prepared in the same way for etching rate measurement was investigated for roughness change. Surface roughness change was measured by atomic force microscope imaging system (Dimension 3100 and Nanoscope IV controller, Veeco Metrology, LLC, Santa Barbara, CA). Images were acquired in tapping mode with silicon TESP7 AFM tips (Veeco Metrology, LLC, Santa Barbara, CA).

5.5 Results and discussions

Multi-channel SPR imaging (MCSPRI) system was custom-built using optical components i.e. equilateral prism, convex lenses, polarizer, narrow band-pass wavelength filter, light source and home-made flow channel cell that consists of Teflon cell and PDMS gasket (Figure 5.8A). Incident light from a tungsten halogen lamp coupled with a narrow band-pass wavelength filter that has a central wavelength of 730 nm passed through a biconvex lens and a plano-convex lens for focusing on the surface of equilateral prism where copper film (45 nm) was coated. Polarity of incident light was controlled by a linear polarizer that was placed between the convex lenses. The emerging reflected light was collimated by another plano-convex lens and monitored by a high resolution CCD camera using a variable zoom lens. CCD camera captured images using both *s*- and *p*- polarized light at the sample rotation where the minimum intensity of reflectivity (SPR angle) could be observed. The captured images are called SPR images (Figure 5.8B). The SPR images are different from normal pictures in that x-axis of SPR image represents angular space. The incident light is

focused as a line on the surface of equilateral prism and spreads out when reflected. Hence the captured SPR image has angular variation on x-axis and regular space on y-axis.

SPR angle that appears as a minimum intensity of reflected light on the angular space of SPR image is a characteristic of solid-liquid interface and optical properties of SPR components. SPR angle is determined by the wavelength of incident light and optical properties of SPR components such as refractive indices of equilateral prism, metal films, and dielectric medium and the thickness of metal films. When the other optical properties have constant values, the SPR angle shift is connected with the optical or physical changes at the interface of metal films and dielectric medium such as additional film adsorption or metal film change.

The refractive indices of SPR components are determined by light wavelength and under 730 nm incident light wavelength, the refractive indices of SF-10 prism, copper film, and water are 1.715, 0.22+4.43i, and 1.33, respectively. Figure 5.8B shows an SPR image obtained from the MCSPRI system with DI water as dielectric medium that was introduced to the flow channels. In the absence of additional layers on copper films, SPR angle appears at 54.5 (± 0.1) ° against the surface normal. The solutions in flow channels are separated by PDMS gasket so that SPR images can be monitored simultaneously with the introduction of various solutions having different chemical compositions. SPR images can be recorded continuously while the solutions flow and hence SPR angle shift can be detected in real time.

The first measurement was carried out in pH controlled solutions. We prepared aqueous solutions that have different pH of 2, 6, and 10 and simultaneously supplied to the flow channel in MCSPRI system following pH 10 solution at a constant flow rate (0.05 ml min^{-1}). Figure 5.9A shows the change of SPR angle by the introduction of pH solutions. As studied in chapter 3, copper surface is either dissolved or passivated in aqueous solutions depending on pH and the dissolution rate is constant at a pH. At high pH (6 and 10), copper surface is passivated and does not show the shift of SPR angle. On the other hand, copper

surface in the channel where pH 2 solution is introduced shows SPR angle increase. In the QCM measurements, the dissolution rate at pH 2 was about 0.35 nm min^{-1}. To compare the dissolution rate, the SPR angle shift as a function of copper thickness is calculated by Fresnel's calculation. Figure 5.10 presents theoretical calculation of SPR angle change as a function of copper thickness in the given conditions (730 nm wavelength, SF-10 prism, and aqueous solution). In the thickness range of 22 and 45 nm copper films, copper thickness has a relationship with SPR angle shift by

$$t_{Cu} = -9.02 \ln\left(\frac{\Delta\theta_{SPR} + 0.13}{18.99}\right) \qquad (22 \text{ nm} < t_{Cu} < 45 \text{ nm}) \qquad (5.33)$$

where t_{Cu} is copper thickness and $\Delta\theta_{SPR}$ is the SPR angle shift from the SPR angle at 45 nm copper film. Using this relationship, SPR angle shift curve at pH 2 can be redrawn for thickness decrease from 45 nm (Figure 5.9B). Thickness decrease is linear up to losing 25 nm. The slope in Figure 5.9B represents dissolution rate, which is about 2.43 nm min^{-1}. Compared with the results (~ 0.35 nm min^{-1}) that were measured by QCM in chapter 3, the dissolution rate is too high. We speculated that the overestimation of etching rate in SPR measurement was due to roughness increase. It is generally known that chemical etching roughens copper surface and according to Raether, SPR angle appears about 0.7 ° higher per 1 nm root mean square (RMS) [38]. Although experimental conditions are different, this deviation is a significant change considering that the formation of 15 nm additional film that has refractive index of 1.5 causes 1 ° of SPR angle shift in our experimental conditions. We measured roughness change by observing copper surface topography taken by AFM imaging and investigated how the surface roughness of copper was changing during etching at pH 2.

Figure 5.11 shows the measured roughness and some examples of AFM images. Roughness in terms of root mean square (RMS) height increases linearly with etching time, and their relationship is given by

$$\delta = 0.06t + 0.54 \qquad (5.34)$$

where δ is RMS height (nm) and t is etching time (min). The equation (5.34) shows that etching time of 10 min increases the roughness about 0.6 nm from the initial roughness. The SPR angle shift in Figure 5.9A is due to combined effects by thickness decrease and roughness. Using this relationship, after 10 min of etching at pH 2, SPR angle shift by thickness decrease is only about 0.23 ° while the measured SPR angle shift is about 1.5 °. This indicates that the main SPR angle shift is due to the roughness change rather than thickness change. Therefore data analysis without considering roughness impact will lead to errors, overestimating thickness change.

The overestimation is more apparent when BTA adsorption is observed in low pH solution. Figure 5.12 shows the observed SPR angle shfit at pH 2 with BTA concentration variation (A) and measured etching rate from SPR angle shift (B). Solutions with various concentrations of BTA (0, 5×10^{-5}, 7×10^{-5}, 1×10^{-4}, 3×10^{-4}, 5×10^{-4}, 7×10^{-4}, 1×10^{-3} mol l^{-1}) were introduced simultaneously to the MCSPRI system following pH 10 solution at a constant flow rate of 0.05 ml min^{-1}. Using the equation (5.33), copper etching rate in each solution is obtained. When compared with the etching rate measured by QCM, SPR measurement overestimates the etching rate by more than ten times. As mentioned previously, surface roughness increases has a major impact on SPR angle change. Therefore, SPR measurement has a limitation to observe film formation while the metal film is interacting with solutions. There is another reason that SPR is not suitable for copper etching rate measurement. In order to observe SPR angle from SPR curves, metal films must have proper thickness and it is pretty narrow range of thickness. For copper, it is between 22 nm and 100 nm in aqueous solution theoretically but in reality, it becomes narrower from 30 to 70 nm, which is only about 40 nm. It is too narrow range of thickness to observe copper etching.

The concept of high throughput screening technique using SPR imaging system is still very attractive and the problem in MCSPRI system is the choice of metal films. To be

effective, the metal films should remain untouched during interfacial reactions. Using a noble metal would solve this problem and gold is often the choice of metal film for SPR.

SPR technique has a variety of applications and in most cases, metal film is used as a simple platform to create evanescent waves. Therefore, complicated designs of cell system are required for high throughput measurement. In MCSPRI system as an example, the variation of reactions for high throughput is acquired by varying solution compositions, which requires complicated cell design. If the variation of reaction is controlled on metal films, the complicated design of cell system would not be necessary. Coupling SPR with electrochemistry is a good way to achieve it. It is advantageous to combine SPR with electrochemistry not only by achieving high throughput relatively simple but also by obtaining simultaneous control and observation of interfacial reactions. In addition, SPR and electrochemistry are complementary for each other since both techniques provide real time data that can be directly compared. Incorporation of SPR with electrochemistry is simple since metal films that are used for generating evanescent wave in SPR can be directly used as electrodes in electrochemistry. Various electrochemical techniques have been coupled with SPR, which includes scanning electrochemical microscopy (SECM)[18, 26], electrochemical quartz crystal microgravimetry (EQCM)[27-29], and impedance[30, 31].

For high throughput measurements, we adopt multi-electrode design of metal films and modify the MCSPRI system. Design of multi-electrode is simply obtained by depositing metal films using a mask and each electrode is easily connected to a potentiostat as a working electrode without short circuit. For SPR imaging system, SF-10 equilateral prism was replaced by BK-7 hemi cylindrical lens coupled with glass slides where 52 nm gold film was coated. The glass slide and hemi cylindrical lens were equipped with home-made Teflon electrochemical cell. Quasi Ag/AgCl reference electrode (QRE) and Pt/Ir grid were inserted to the cell as a reference and counter electrode, respectively. Each gold band on the glass slide was connected to a multi potentiostat as a working electrode (Figure 5.13).

SPR images from the MESPRI system were obtained in the same way with MCSPRI system. Incident light from a tungsten halogen lamp that was coupled with a wavelength filter passed through optical lenses and a linear polarizer and focused on the glass slide surface where gold film was deposited. The reflected light was collimated by a plano-convex lens and monitored by a high resolution CCD camera using a variable zoom lens. CCD camera captured images using both *s*- and *p*- polarized light at the sample rotation where the minimum intensity of reflectivity could be observed.

Figure 5.14 shows gold coated glass slide (A), SPR image (B), and SPR curve (C). SPR images from the MESPRI system present relative reflectivity from two surfaces, gold and glass. The relative reflectivity from gold surface gives SPR curve and that from glass shows critical angle where total reflection occurs. Critical and SPR angles are determined by optical properties of SPR components. Under the 730 nm light wavelength, refractive indices of BK-7 hemi cylindrical lens, gold, and aqueous solution are 1.512, 0.135+4.33i, and 1.328, respectively. Using Snell's law[33], critical angle is calculated with refractive indices of prism and solution, which appears at 61.4 ° for our system.

$$\theta_{crit} = \sin^{-1}\left(\frac{n_2}{n_1}\right) \tag{5.35}$$

n_1 and n_2 are refractive indices of first (BK-7 lens) and second media (solution) that incident light encounters, respectively. SPR angle is theoretically calculated by Fresnel's equation. When the thickness of gold film is 52 nm and water is used as dielectric medium, SPR angle appears at 67.4 °. Thickness of Au film is an important factor to determine SPR angle and intensity.

We will demonstrate the capability of MESPRI system for electrochemical control of metal electrodes and real time measurement of surface reactions by detecting SPR angle change. Dynamic SPR images observed in real time and corresponding SPR curves are presented during cyclic voltammetry on gold in aqueous solutions. SPR angle change is

compared with electrochemical data. As an application of high throughput measurement, gold films are loaded with different electrochemical potentials and SPR images are obtained.

The capability of MESPRI system to control metal electrodes electrochemically and to observe in real time with SPR imaging was demonstrated by running cyclic voltammetry (CV) on gold film in 0.1 M H_2SO_4 + 0.1 M Na_2SO_4 solution. CV was run on gold film between -0.5 V and 1.2 V vs. QRE with a scan rate of 100 mV sec^{-1}. SPR images (Figure 5.15A) were recorded while running CV and SPR curves (Figure 5.15B) were extracted from dynamic SPR images. SPR angle in each SPR image represents the surface state of gold film under the given potential. In order to quantify SPR angles, SPR curves are extracted from the SPR images. From each curve, SPR angle could be identified and compared with the undisturbed SPR curve to quantify the shift. Figure 5.16A shows the real time SPR angle change that corresponds to CV curve (Figure 5.16B). CV curve shows typical shape for gold electrode in aqueous solution and SPR angle change is due to optical property change on gold surface, which is oxide formation by high electrochemical potential. According to Xia et al.[39], chemical composition of gold oxide in this potential range is mainly AuO and its refractive index is 3.3+1.1i. The Fresnel calculation yields about 0.8 ° of SPR angle shift with 1 nm increase of gold oxide on metallic gold surface as an additional film. SPR angle shift at 1.2 V in Figure 5.16A is about 0.4 ° that corresponds to 0.5 nm thick AuO film.

MESPRI is not only able to measure interfacial change in real time but also to screen multi-electrode in high throughput. Figure 5.17A shows SPR images of two gold bands at different potentials, 0.0 V (①) and 1.2 V (②) and their corresponding SPR curves (③). The extraction of SPR curves from SPR images provide quantitative information about interfacial changes but requires the analysis of measured SPR angle shift using Fresnel calculation. Simple image calculation can provide a quick sense of SPR angle shift. Figure 5.17B① shows subtracted SPR image from Figure 5.17A② to ①. Subtracted SPR image has a maximum and minimum in intensity that shows the difference of SPR angles from two SPR

images. As the contrast and angular space between the intensity peaks is bigger, the two SPR images have bigger difference in SPR angles. Figure 5.17C shows a subtracted SPR image for multi-electrode gold film. An SPR image for gold bands at 0.0 V is subtracted from that where each gold band is charged at different electrochemical potential. Potential increases from -0.2 V at the top to 1.2 V at the bottom electrodes with 0.2 V step increase, where bigger potential difference shows higher contrast. Figure 5.17 shows a great potential of MESPRI system as a high throughput real time screening technique by combining SPR imaging with electrochemistry.

5.6 Conclusions and future work

In this chapter, we developed two high throughput real time detection system using SPR imaging. Multi-channel SPR imaging (MCSPRI) system was developed by coupling SPR imaging system with home-made flow channel cell to study copper chemistry and additional film formation of benzotriazole on copper. The interfacial reactions that removed copper films increased roughness that had a major impact on measured data. The lack of quantitative information about roughness impact on SPR angle shift made it difficult to separate film formation from the measured data.

The concept of high throughput screening with SPR imaging system motivated us to develop multi-electrode SPR imaging (MESPRI) system to combine the SPR system with electrochemistry. The combination of SPR and electrochemical techniques was simple but effective and provided significant advantages for simultaneous control and observation of metal-liquid interfaces. We demonstrated the capability of MESPRI, i.e. electrochemical control and simultaneous detection with SPR imaging and high throughput observation. Despite some limitations, both MCSPRI and MESPRI systems have great potentials to investigate solid liquid interfaces and possible applications.

5.7 References

1. Liedberg, B., C. Nylander, and I. Lundstrom, *Biosensing with surface plasmon resonance - how it all started.* Biosensors & Bioelectronics, 1995. **10**(8): p. i-ix.
2. Mullett, W.M., E.P.C. Lai, and J.M. Yeung, *Surface Plasmon Resonance-Based Immunoassays.* Methods, 2000. **22**(1): p. 77-91.
3. Homola, J., S.S. Yee, and G. Gauglitz, *Surface plasmon resonance sensors: review.* Sensors and Actuators B: Chemical, 1999. **54**(1-2): p. 3-15.
4. Knoll, W., *Interfaces and thin films as seen by bound electromagnetic waves*. 1998. p. 569-638.
5. Homola, J., *Present and future of surface plasmon resonance biosensors.* Analytical and Bioanalytical Chemistry, 2003. **377**(3): p. 528-539.
6. Green, R.J., R.A. Frazier, K.M. Shakesheff, M.C. Davies, C.J. Roberts, and S.J.B. Tendler, *Surface plasmon resonance analysis of dynamic biological interactions with biomaterials.* Biomaterials, 2000. **21**(18): p. 1823-1835.
7. Yeatman, E.M., *Resolution and sensitivity in surface plasmon microscopy and sensing.* Biosensors & Bioelectronics, 1996. **11**(6-7): p. 635-649.
8. Kanoh, N., M. Kyo, K. Inamori, A. Ando, A. Asami, A. Nakao, and H. Osada, *SPR imaging of photo-cross-linked small-molecule arrays on gold.* Analytical Chemistry, 2006. **78**(7): p. 2226-2230.
9. Yuk, J.S., D.-G. Hong, H.-I. Jung, and K.-S. Ha, *Application of spectral SPR imaging for the surface analysis of C-reactive protein binding.* Sensors and Actuators, B: Chemical, 2006. **119**(2): p. 673-675.
10. Wilkop, T., Z. Wang, and Q. Cheng, *Analysis of μ-contact printed protein patterns by SPR imaging with a LED light source.* Langmuir, 2004. **20**(25): p. 11141-11148.
11. Wolf, L.K., D.E. Fullenkamp, and R.M. Georgiadis, *Quantitative angle-resolved SPR imaging of DNA-DNA and DNA-drug kinetics.* Journal of the American Chemical Society, 2005. **127**(49): p. 17453-17459.
12. Yuk, J.S., H.-S. Kim, J.-W. Jung, S.-H. Jung, S.-J. Lee, W.J. Kim, J.-A. Han, Y.-M. Kim, and K.-S. Ha, *Analysis of protein interactions on protein arrays by a novel spectral surface plasmon resonance imaging.* Biosensors and Bioelectronics, 2006. **21**(8): p. 1521-1528.

13. Kanda, V., J.K. Kariuki, D.J. Harrison, and M.T. McDermott, *Label-free reading of microarray-based immunoassays with surface plasmon resonance imaging.* Analytical Chemistry, 2004. **76**(24): p. 7257-7262.
14. Lee, H.J., Y. Li, A.W. Wark, and R.M. Corn, *Enzymatically amplified surface plasmon resonance imaging detection of DNA by exonuclease III digestion of DNA microarrays.* Analytical Chemistry, 2005. **77**(16): p. 5096-5100.
15. Pyo, H.-B., Y.-B. Shin, M.-G. Kim, and H.C. Yoon, *Multichannel surface plasmon resonance imaging and analysis of micropatterned self-assembled monolayers and protein affinity interactions.* Langmuir, 2005. **21**(1): p. 166-171.
16. Wegner, G.J., A.W. Wark, H.J. Lee, E. Codner, T. Saeki, S. Fang, and R.M. Corn, *Real-time surface plasmon resonance imaging measurements for multiplexed determination of protein adsorption/desorption kinetics and surface enzymatic reactions on peptide microarrays.* Analytical Chemistry, 2004. **76**(19): p. 5677-5684.
17. Inamori, K., M. Kyo, Y. Nishiya, Y. Inoue, T. Sonoda, E. Kinoshita, T. Koike, and Y. Katayama, *Detection and quantification of on-chip phosphorylated peptides by surface plasmon resonance imaging techniques using a phosphate capture molecule.* Analytical Chemistry, 2005. **77**(13): p. 3979-3985.
18. Szunerits, S., N. Knorr, R. Calemczuk, and T. Livache, *New approach to writing and simultaneous reading of micropatterns: Combining surface plasmon resonance imaging with scanning electrochemical microscopy (SECM).* Langmuir, 2004. **20**(21): p. 9236-9241.
19. Smith, E.A., M.G. Erickson, A.T. Ulijasz, B. Weisblum, and R.M. Corn, *Surface plasmon resonance imaging of transcription factor proteins: Interactions of bacterial response regulators with DNA arrays on gold films.* Langmuir, 2003. **19**(5): p. 1486-1492.
20. Piliarik, M., H. Vaisocherova, and J. Homola, *Towards parallelized surface plasmon resonance sensor platform for sensitive detection of oligonucleotides.* Sensors and Actuators, B: Chemical, 2007. **121**(1): p. 187-193.
21. Ho, H.P. and W.W. Lam, *Application of differential phase measurement technique to surface plasmon resonance sensors.* Sensors and Actuators, B: Chemical, 2003. **96**(3): p. 554-559.
22. Smith, E.A., M.J. Wanat, Y. Cheng, S.V.P. Barreira, A.G. Frutos, and R.M. Corn, *Formation, spectroscopic characterization, and application of sulfhydryl-terminated alkanethiol monolayers for the chemical attachment of DNA onto gold surfaces.* Langmuir, 2001. **17**(8): p. 2502-2507.

23. Iwasaki, Y., T. Horiuchi, M. Morita, and O. Niwa, *Analysis of electrochemical processes using surface plasmon resonance.* Sensors and Actuators, B: Chemical, 1998. **B50**(2): p. 145-148.
24. Iwasaki, Y., T. Horiuchi, M. Morita, and O. Niwa, *Electrochemical reaction of Fe(CN)3-/4-6 on gold electrodes analyzed by surface plasmon resonance.* Surface Science, 1999. **427-428**: p. 195-198.
25. Baba, A. and W. Knoll, *Electrochemical growth of dendritic conducting polymer networks.* Advanced Materials, 2003. **15**(12): p. 1015-1019.
26. Szunerits, S., Y. Coffinier, S. Janel, and R. Boukherroub, *Stability of the gold/silica thin film interface: Electrochemical and surface plasmon resonance studies.* Langmuir, 2006. **22**(25): p. 10716-10722.
27. Schweiss, R., J.F. Lubben, D. Johannsmann, and W. Knoll, *Electropolymerization of ethylene dioxythiophene (EDOT) in micellar aqueous solutions studied by electrochemical quartz crystal microbalance and surface plasmon resonance.* Electrochimica Acta, 2005. **50**(14): p. 2849-2856.
28. Baba, A., S. Tian, F. Stefani, C. Xia, Z. Wang, R.C. Advincula, D. Johannsmann, and W. Knoll, *Electropolymerization and doping/dedoping properties of polyaniline thin films as studied by electrochemical-surface plasmon spectroscopy and by the quartz crystal microbalance.* Journal of Electroanalytical Chemistry, 2004. **562**(1): p. 95-103.
29. Bailey, L.E., D. Kambhampati, K.K. Kanazawa, W. Knoll, and C.W. Frank, *Using surface plasmon resonance and the quartz crystal microbalance to monitor in situ the interfacial behavior of thin organic films.* Langmuir, 2002. **18**(2): p. 479-489.
30. Terrettaz, S., T. Stora, C. Duschl, and H. Vogel, *Protein binding to supported lipid membranes : Investigation of the cholera toxin-ganglioside interaction by simultaneous impedance spectroscopy and surface plasmon resonance.* Langmuir, 1993. **9**(5): p. 1361-1369.
31. Lingler, S., I. Rubinstein, W. Knoll, and A. Offenhaeusser, *Fusion of small unilamellar lipid vesicles to alkanethiol and thiolipid self-assembled monolayers on gold.* Langmuir, 1997. **13**(26): p. 7085-7091.
32. Ritchie, R.H., *Plasma Losses by Fast Electrons in Thin Films.* Physical Review, 1957. **1**(5): p. 874-881.
33. Klein, M.V. and T.E. Furtak, *Optics*. 2nd ed. 1986: John Wiley & Sons, Inc.
34. Kretschm.E and H. Raether, *Radiative Decay of Non Radiative Surface Plasmons Excited by Light.* Zeitschrift Fur Naturforschung Part a-Astrophysik Physik Und Physikalische Chemie, 1968. **A 23**(12): p. 2135-&.

35. Kretschmann. E, *Die Bestimmung optischer Konstanten von Metallen durch Anregung von Oberflachenplasmaschwingungen.* Z. Phys., 1971. **241**: p. 313-324.
36. Otto, A., *Excitation of Nonradiative Surface Plasma Waves in Silver by Method of Frustrated Total Reflection.* Zeitschrift Fur Physik, 1968. **216**(4): p. 398-&.
37. Hansen, W.N., *Electric Fields Produced by Propagation of Plane Coherent Electromagnetic Radiation in a Stratified Medium.* Journal of the Optical Society of America, 1968. **58**(3): p. 380-390.
38. Raether, H., *Surface-Plasmons on Smooth and Rough Surfaces and on Gratings*. Springer Tracts in Modern Physics. Vol. 111. 1988. 1-133.
39. Xia, S.J. and V.I. Birss, *Multi-technique study of compact and hydrous Au oxide growth in 0.1 M sulfuric acid solutions.* Journal of Electroanalytical Chemistry, 2001. **500**(1): p. 562-573.
40. Raether, H., *Excitation of Plasmons and Interband Transitions by Electrons*. Springer Tracts in Modern Physics. Vol. 88. 1980, Berlin Heidelberg New York: Springer-Verlag.

Table 5.1 Characteristics of surface plasmon waves (SPW) at the metal-water interface[3]

Metal layer	Ag		Au	
Light wavelength (nm)	630	850	630	850
Penetration depth into metal (nm)	24	23	29	25
Penetration depth into water (nm)	219	443	162	400

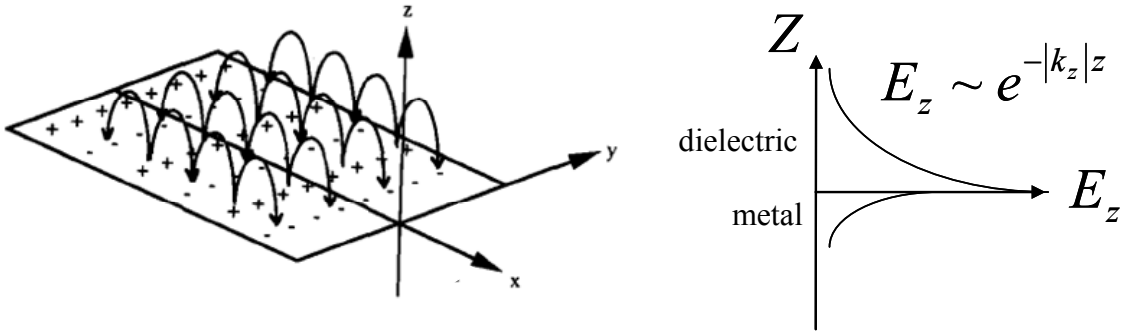

Figure 5.1 Charge and electric field distribution for a surface plasmon propagating in the x direction in the dielectric space above a metallic surface and the exponential dependence of the field Ez [7, 38].

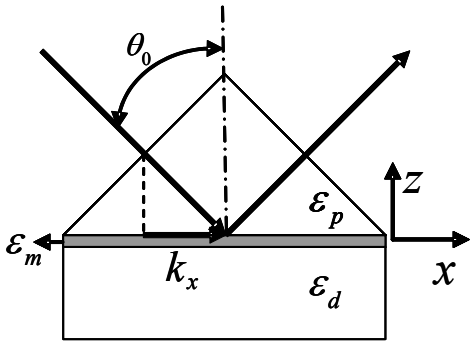

Figure 5.2 A plane parallel plasma film with a dielectric function ε_m covered on both sides with media of different dielectric values ε_p and ε_d.

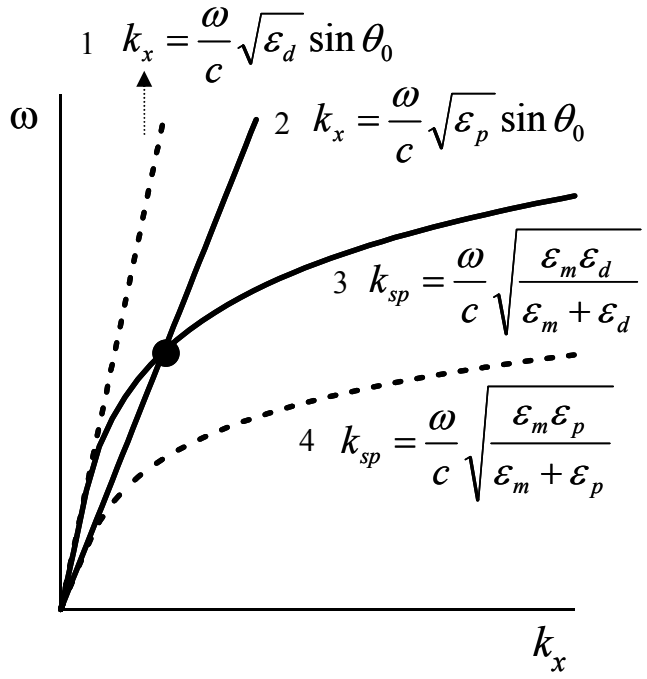

Figure 5.3 Dispersion relations of a plane parallel plasma film with a dielectric function ε_m covered on both sides with media of different dielectric values ε_p and ε_d (adapted from [38, 40]).

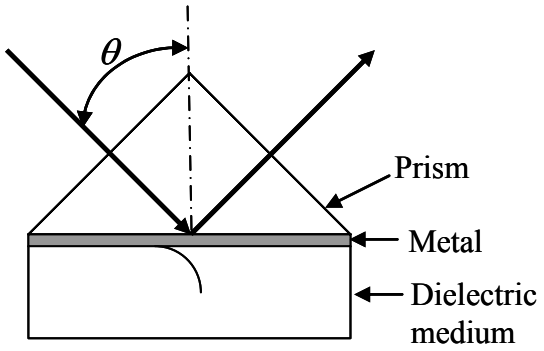

Figure 5.4 SPR system in Kretschmann configuration (adapted from [4, 7, 34]).

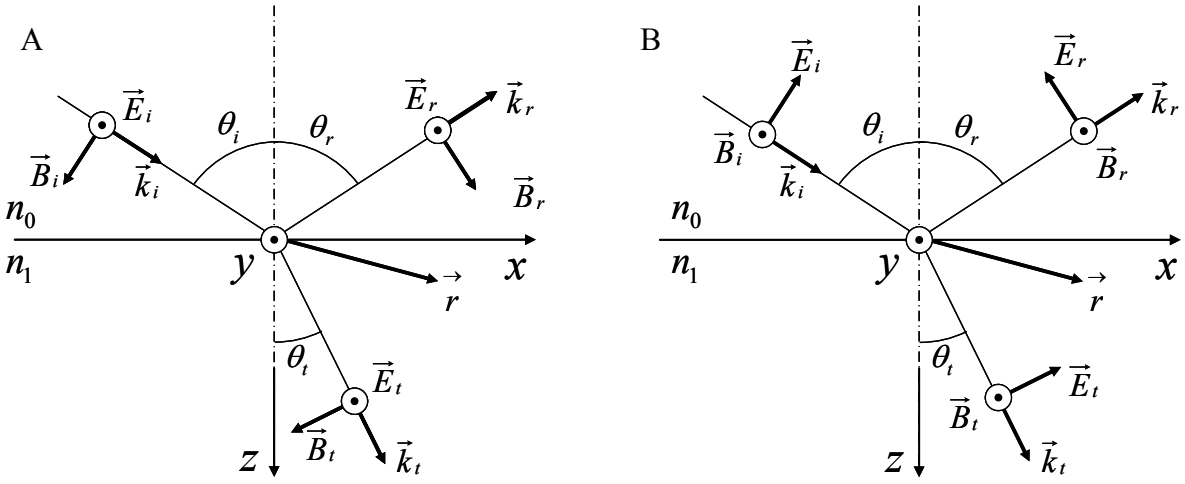

Figure 5.5 Geometry that establishes the conventions for the optics at an interface: (A) s-polarized light; (B) p-polarized light (adapted from [33]).

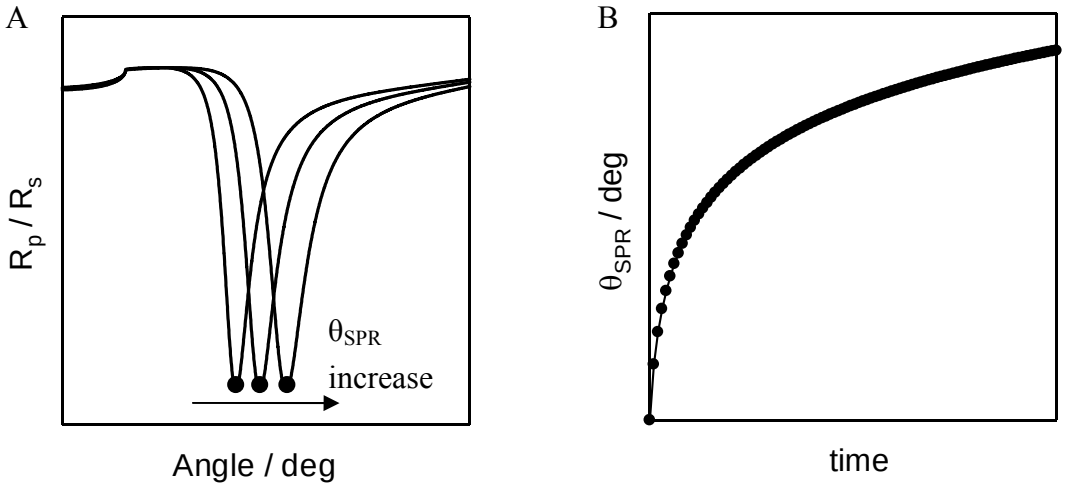

Figure 5.6 SPR curve (A) and SPR angle shift (B) upon film formation on metal.

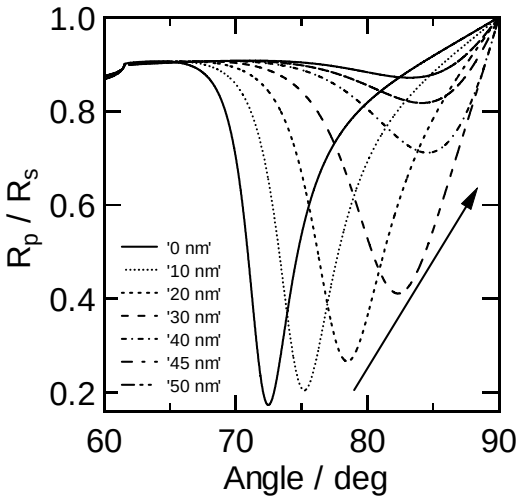

Figure 5.7 SPR curve change as the thickness of an organic film with refractive index of 1.5 is increased. SPR angle is not detectable with more than 50 nm of the film.

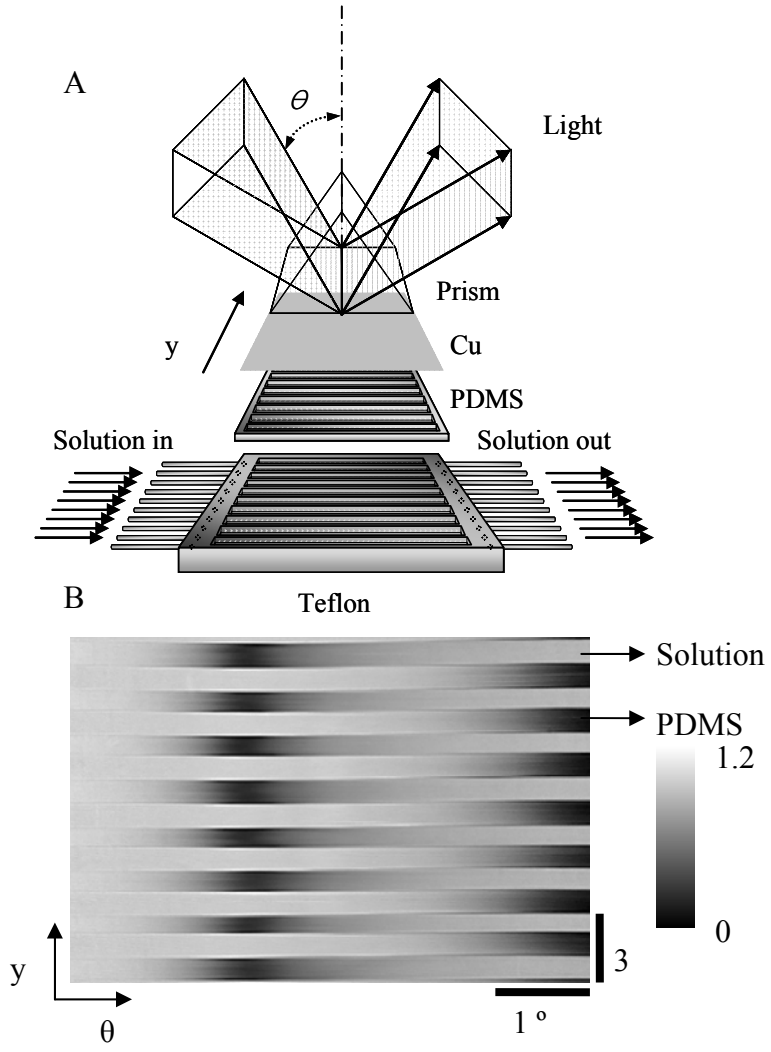

Figure 5.8 Schematic for converging light SPR imaging system (A). SPR image of Cu in contact with aqueous solutions (B).

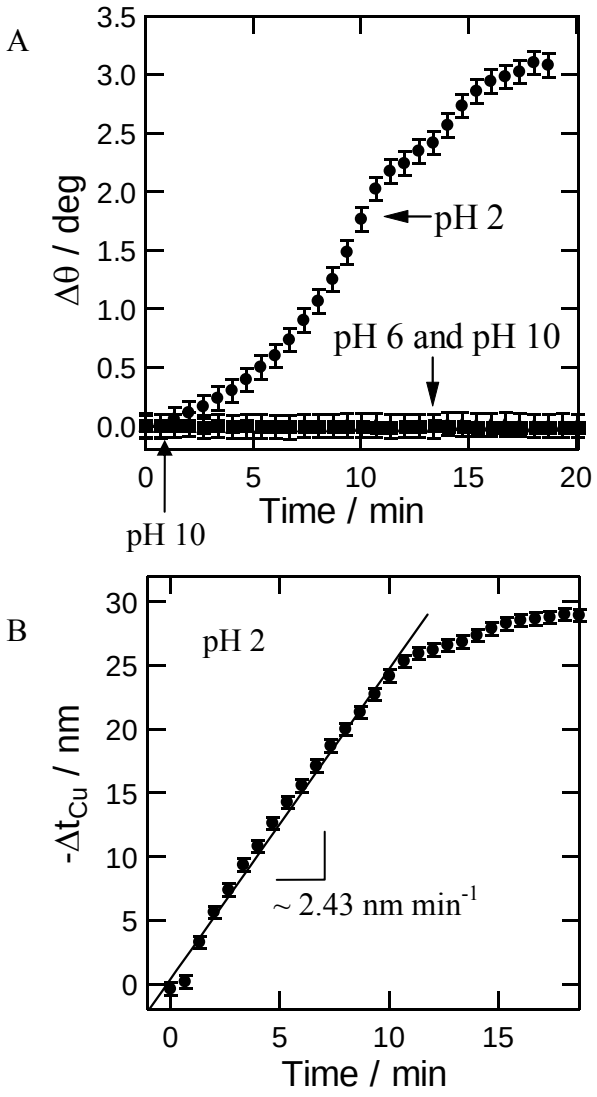

Figure 5.9 Real-time measurement of SPR angles on copper in aqueous solutions at pH 2, 6, and 10 (A). Thickness change of copper at pH 2 can be obtained without consideration of roughness impact (B).

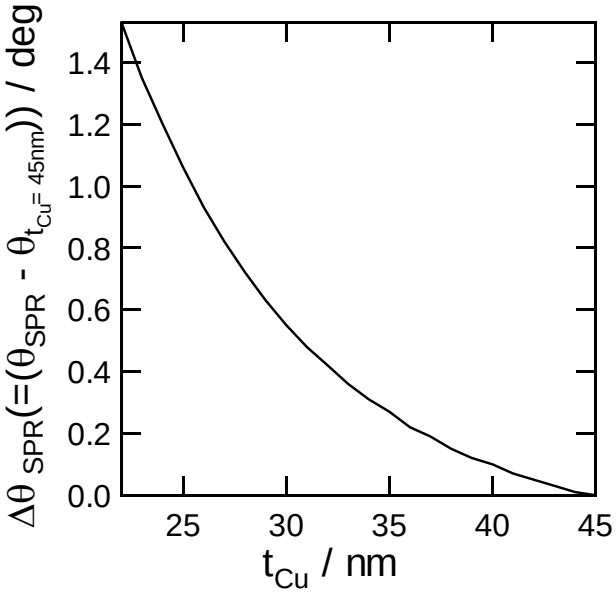

Figure 5.10 SPR angle change as a function of copper thickness in SPR system without additional films. Light with wavelength 730 nm is used along with SF-10 prism and water as dielectric medium.

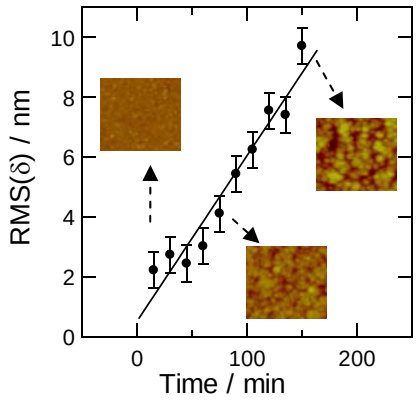

Figure 5.11 Surface roughness change according to etching time. Root mean square (RMS) height linearly increases with etching time.

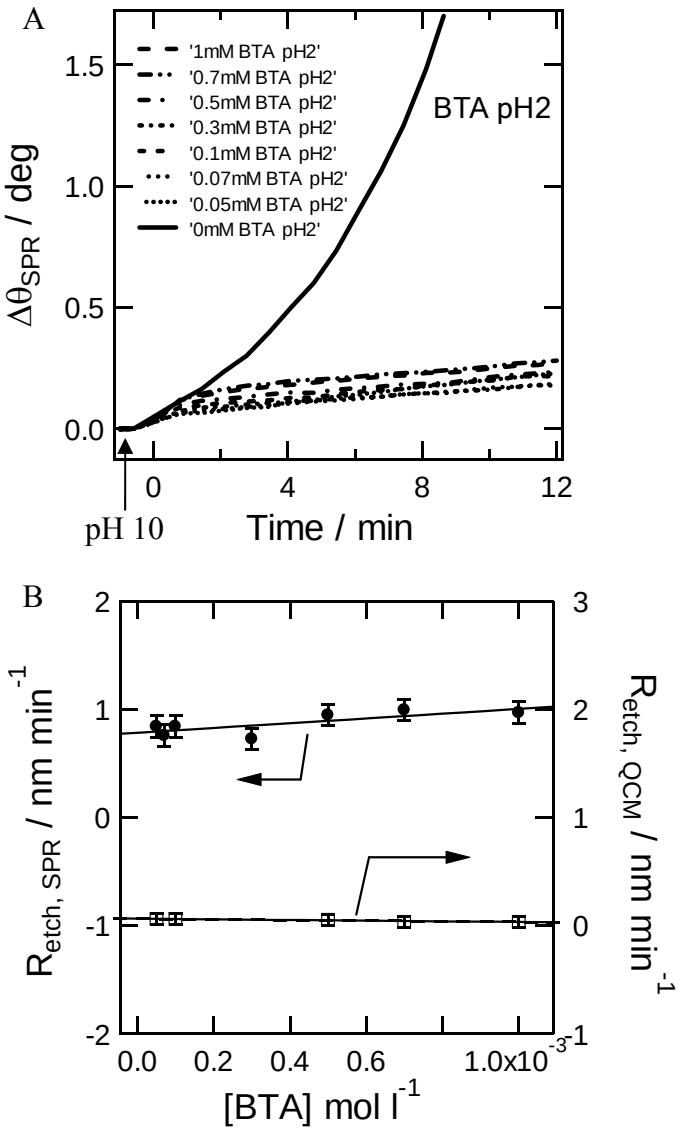

Figure 5.12 SPR angle shift at pH 2 with BTA concentration variation (A) and etching rate comparison with QCM measurement (B).

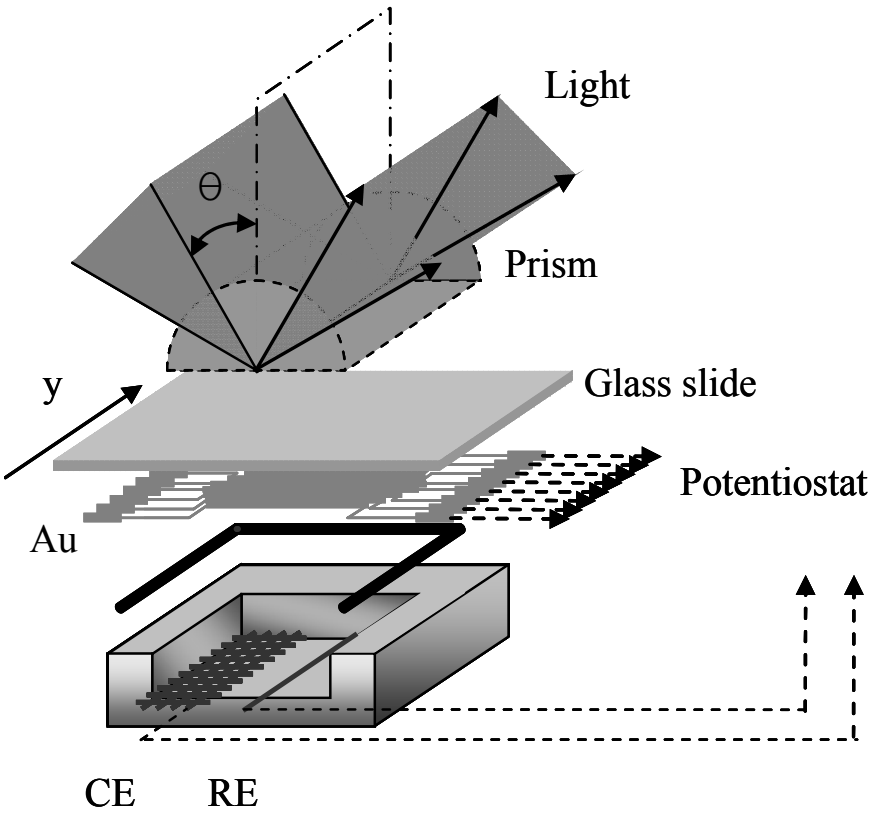

Figure 5.13 Schematic high throughput electrochemical SPR imaging system. Converging light beam is focused on the prism surface. Multi-electrode Au is in contact with an electrolyte, where electrochemistry is applied.

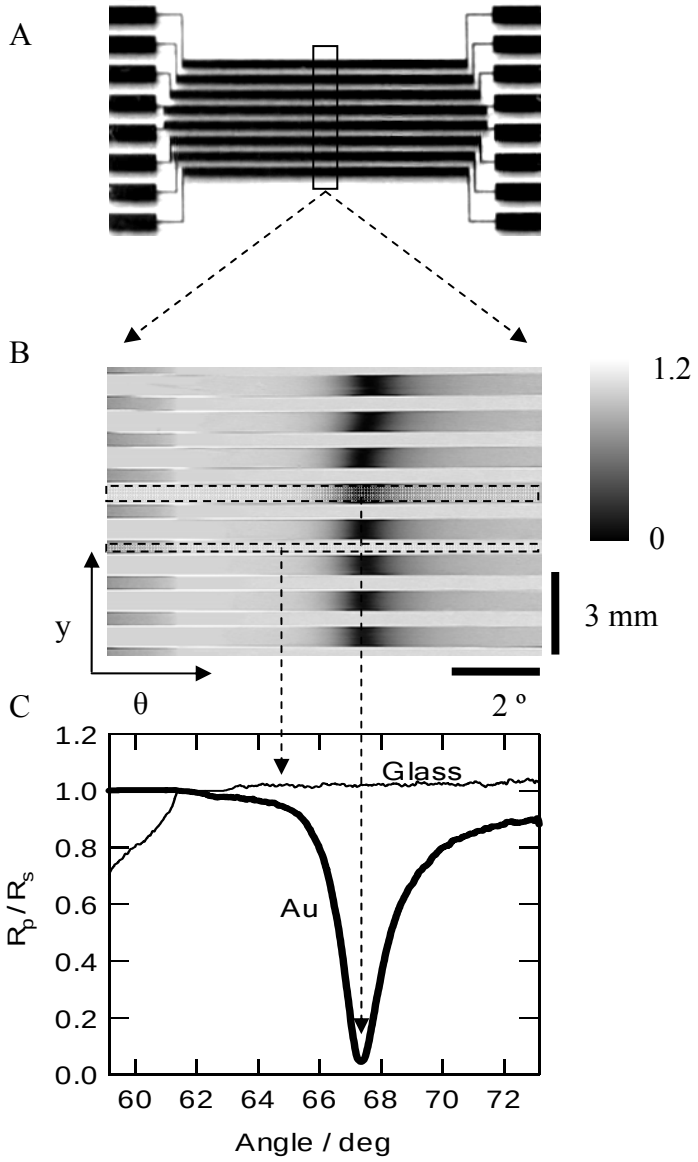

Figure 5.14 Au-coated glass slide (A) SPR image and (B) SPR curve of Au multi-electrode in contact with H_2O and relative reflectivity curve from glass surface (C).

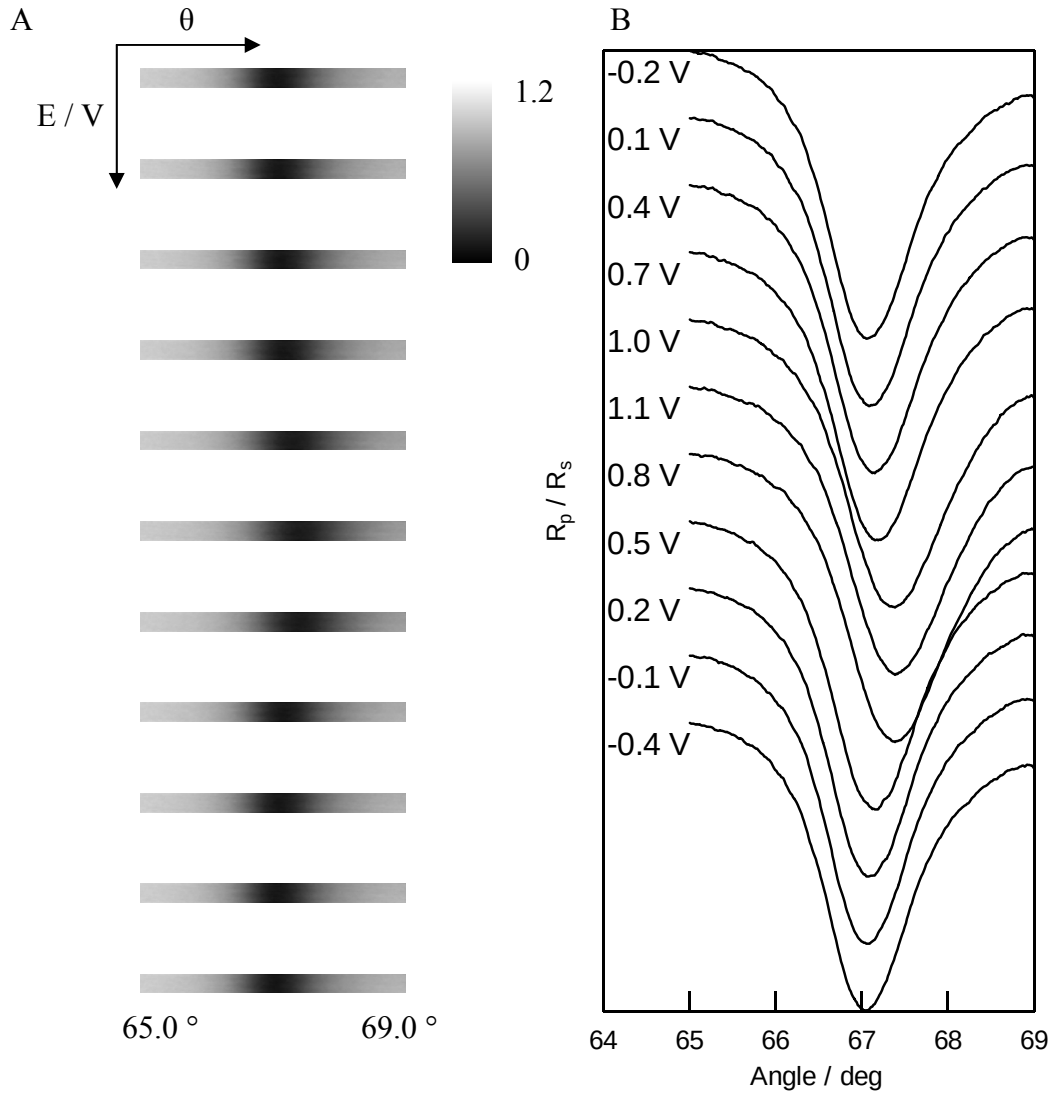

Figure 5.15 Dynamic SPR images (A) and SPR curves (B) during cyclic voltammetry of Au in 0.1 M H_2SO_4 + 0.1 M Na_2SO_4.

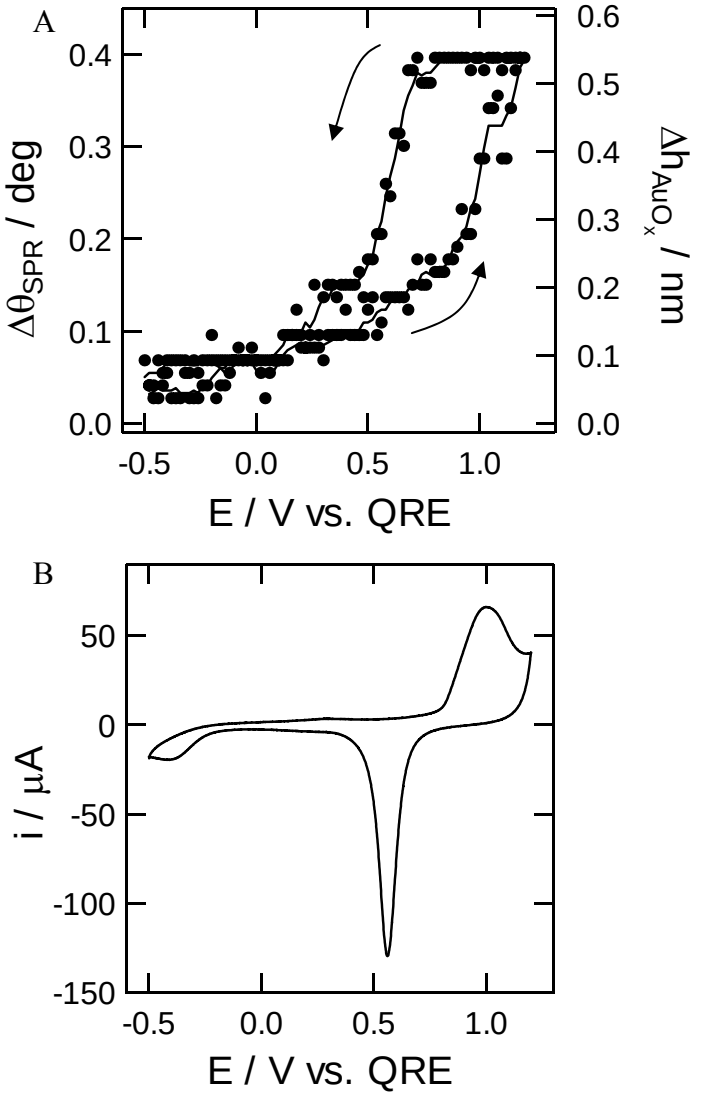

Figure 5.16 Real-time detection of SPR angle (A) with electrochemistry variation (B) in 0.1 M H_2SO_4 + 0.1 M Na_2SO_4.

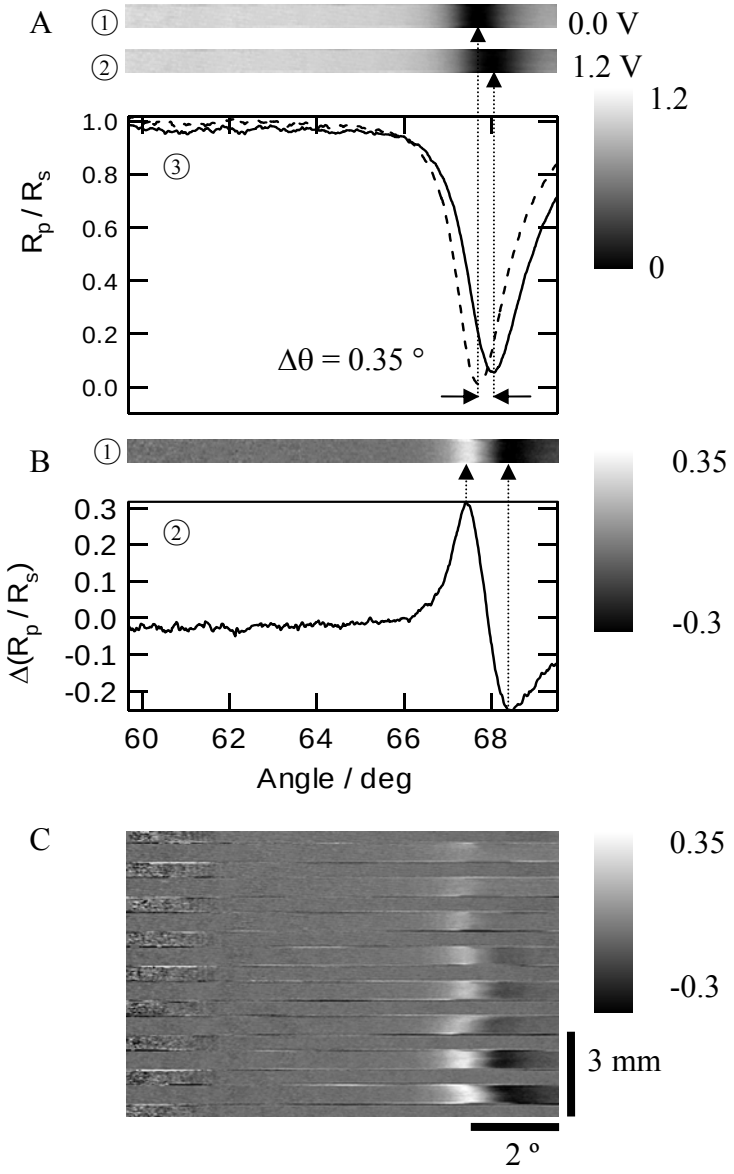

Figure 5.17 (A) SPR image of Au band biased at 0.0 V (①) and at 1.2 V (②) and their extracted SPR curves (③) from the images. (B) Subtracted SPR image from original SPR images at 1.2 V and 0.0 V (①) and its corresponding subtracted SPR curve (②). (C) Subtracted SPR images for multi-electrode in various potentials.

Chapter 6. Conclusions and Future Directions

This work focused on studying fundamental chemical reactions of copper in aqueous solutions in the presence of various chemical components and constructed a coherent dissolution rate model based on the fundamental kinetic mechanisms. The studies were carried out at two different pH, where copper has different outermost surface at equilibrium. We utilized quartz crystal microgravimetry (QCM) as a main tool for investigation and kinetic study was accompanied by modeling. Kinetic models were set up for the reactions between chemical components and copper surface. A coherent etching rate model was constructed by additive combination of the individual kinetic models and compensated for the deviations when multi components were put together. Compared with previous models, the etching rate model was based on more fundamental chemistry. The model was constructed in the same principle with Paul model but much more detailed chemical reaction mechanisms were considered experimentally and theoretically. In situ real time high throughput screening techniques were developed to observe film formations on copper by using surface plasmon resonance (SPR) imaging system coupled with multi-channel flow cell setup. Slight modifications of the multi-channel SPR imaging (MCSPRI) system constructed another high throughput screening system that was combined with electrochemistry (MESPRI). Experimental designs were described and advantages and limitations of MCSPRI and MESPRI systems were discussed. The following conclusions and future directions can be drawn from each part in this dissertation.

Chemical etching rate study of copper at low pH (Chapter 3): This section presents chemical etching rate study of copper at pH 2 and construction of etching rate model. Copper responses in various pH solutions were observed prior to monitoring reactions with chemical agents. Elementary reactions of copper were experimentally observed and kinetically analyzed in aqueous solutions at pH 2 that contained BTA, glycine, or hydrogen

peroxide. Real time investigation with QCM showed that each chemical agent had significant impact on etching rate change of copper. Hydrogen peroxide considerably increased etching rate by oxidizing metallic copper to copper oxide that was soluble at higher rate. On the other hand, etching rate was exponentially decreased by including BTA, which indicated BTA followed Langmuir adsorption isotherm. Multiple layer formation was not observed. Glycine addition at pH 2 decreased etching rate, which was speculated due to the consumption of a fraction of oxide ions that were supposed to oxidize metallic copper to form cuprous oxide followed by dissolution. An additive etching rate formula was constructed based on the elementary reaction kinetics. The additive model was tested by comparing its prediction with experimental measurement in multi component systems. Simple additive formula didn't work for such a case that more than single components were involved, which led the incorporation of secondary and tertiary etching rate constants. Secondary interaction between BTA and hydrogen peroxide was the most obvious, where inhibition of BTA nearly disappeared in the presence of hydrogen peroxide while the oxidation by hydrogen peroxide was preserved regardless of BTA presence. The updated model described experimentally measured data well.

Chemical etching rate study of copper at high pH (Chapter 4): Chemical etching rate study of copper was extended for high pH in this section following chapter 3. In this moderately high pH solution, copper was covered by passivation layer that was formed by hydroxide ions at high pH. Introduction of glycine initiated dissolution while BTA and hydrogen peroxide did not. When put together with glycine, BTA and hydrogen peroxide had impact on etching rate, which was increased and exponentially decreased by hydrogen peroxide and BTA, respectively. It was apparent that glycine combines only with oxidized copper at high pH not with metallic copper at low pH. Addiitive model at pH 9.7 was constructed in the same way at pH 2 and compared with experimental results of multi component systems. Impacts of secondary and tertiary interactions among the chemical

agents were similar to those at low pH. That is, inhibition of BTA was significantly reduced by the presence of hydrogen peroxide while glycine had little interactions with hydrogen peroxide and BTA.

The etching rate model at both pH described experimental data well and elementary chemical reactions were additively combined to form the model. Since the model was built based on additive combination of elementary reactions, further chemical or even mechanical reactions can be incorporated by simple addition of kinetic expressions, which makes the model have great potential and guides future study.

Development of high throughput surface plasmon resonance (SPR) imaging system (Chapter 5): This section presents the development of real time high throughput detection techniques using surface plasmon resonance (SPR) imaging system. SPR imaging systems using incident light with variable angle were coupled with home-made flow channel cell to construct multi-channel SPR imaging (MCSPRI) system. BTA film formation was investigated using MCSPRI but presented limitations due to major impact on the observed SPR angle measurement by roughness. However, another high throughput measurement system coupled with electrochemistry was constructed by modification of the MCSPRI system. It was illustrated to construct SPR imaging system with multi-electrode design for electrochemical application. SPR imaging system that could monitor solid-liquid interfaces from various angles simultaneously without goniometer allowed detecting SPR angle change in real time. Coupling electrochemistry with SPR imaging system was simple but effective because metal films in SPR system could be used directly as electrodes for electrochemistry. Multi-electrode design upgraded the electrochemical SPR imaging system to high throughput monitoring system. This work demonstrated the capability of the multi-electrode SPR imaging (MESPRI) system as an in-situ real time high throughput screening method and advantages of simultaneous control and monitoring of interfacial reactions were presented.

The development of a coherent etching rate model based on fundament chemical reaction mechanisms is a big step toward a complete control of CMP process. This study is limited as investigation of chemical reactions without mechanical action which is another major component in CMP. The future research is directed to investigate this mechanical reaction and combine with the etching rate model presented in this study. The development of high throughput SPR imaging systems for chemical and electrochemical variations provides a great advantage. The proof of concept data is presented in this study and more applications are pursued as future research.

Appendix

4-Phase Fresnel calculation

```
n1=1.515;                % refractive index of the prism
n2=0.1742+3.41i;         % refractive index of the metal film (Cu)
d2=45;                   % thickness of the metal film
n3=1.5;                  % refractive index of the adsorbed layer
d3=10;                   % thickness of the adsorbed layer
n4=1.332;                % refractive index of the dielectric medium (solution)
lambda=632.8;            % the wavelength of incident light [nm]
theini=30;               % the start of the incident angle [deg]
ang=20;                  % the range of angle scan for the incident light
d=0.01;                  % step angle for the angle increase
range=ang/d;             % determines the number of iteration
SPR=double(zeros(range,2));          % blank matrix for the SPR curve as initiative
for j=1:range
thetaangle=theini+d*j;
theta=thetaangle*pi/180;
    e1=n1^2;
    e2=n2^2;
    e3=n3^2;
    e4=n4^2;
    c1=sqrt(n1^2-n1^2*(sin(theta))^2);
    c2=sqrt(n2^2-n1^2*(sin(theta))^2);
```

```
        c3=sqrt(n3^2-n1^2*(sin(theta))^2);
        c4=sqrt(n4^2-n1^2*(sin(theta))^2);
        b2=c2*(2*pi*d2/lambda);
        b3=c3*(2*pi*d3/lambda);
        q1=c1/e1;
        q2=c2/e2;
        q3=c3/e3;
        q4=c4/e4;
        m11=cos(b2)*cos(b3)-q3*sin(b2)*sin(b3)/q2;
        m12=-i*cos(b2)*sin(b3)/q3-i*sin(b2)*cos(b3)/q2;
        m21=-i*q2*sin(b2)*cos(b3)-i*q3*sin(b3)*cos(b2);
        m22=-q2*sin(b2)*sin(b3)/q3+cos(b2)*cos(b3);
        r=((m11+m12*q4)*q1-(m21+m22*q4))/((m11+m12*q4)*q1+(m21+m22*q4));
        r2=abs(r)^2;
        SPR(j,1)=thetaangle;
        SPR(j,2)=r2;
end
min(SPR(:,2))
x=find(SPR==min(SPR(:,2)));
minang=SPR(x-range,1)
plot(SPR(:,1),SPR(:,2))
save('u:\SPR\20.txt','SPR','-ASCII')
```

Acknowledgements

First and foremost, I would like to thank professor Hillier for all his support and guidance throughout my graduate study. I thank my parents Gun-ee Choi and Jin-ja Chun and my older brother Chang-won Choi for providing me support and trust in my potential at all times.

I would also like to thank my teachers and professors who guided my way and inspired me to push myself to do justice to my potential. Especially, prof. Yongsug Tak was being my mentor since when I was sophomore and guided me to graduate school. Dr. Byoungwon Cho and Dr. Wonil Cho at KIST also supported me to continue study at graduate school. Prof. Hudson at University of Virginia was my mentor that I could always rely on.

My friends hold a special place in my heart. I have met my best friends in college. They were always on my side through difficult phases and shared happiness and pleasure on success. My special mention goes to Jae-hyuck Han, Jong-gyun Park, Hyun-su Huh, Sug-geun Park, Young-ho Lee, and Ki-yun Hong. I would also like to share the joy with friends I met at Iowa State University. Especially Choonho Jung and Jangwoon Lee shared one of the most difficult times with me.

I would also like to express my appreciation to Hillier-group members – Sudha, Kousik, Lu, Karine, Bipin, Erin, and Yi to make my research experience a pleasurable and fruitful one. I especially thank to Bipin and Erin for all the useful discussions. My fellow graduate students at CBE also made my school life fun. I thank professors, secretaries, and support staff both at University of Virginia and at Iowa State University.